Main Bearing Fatigue Analysis: Fixed vs. Floating Offshore Wind Turbines

MSc Program: Sustainable Energy Technology

Georgios Verykokkos

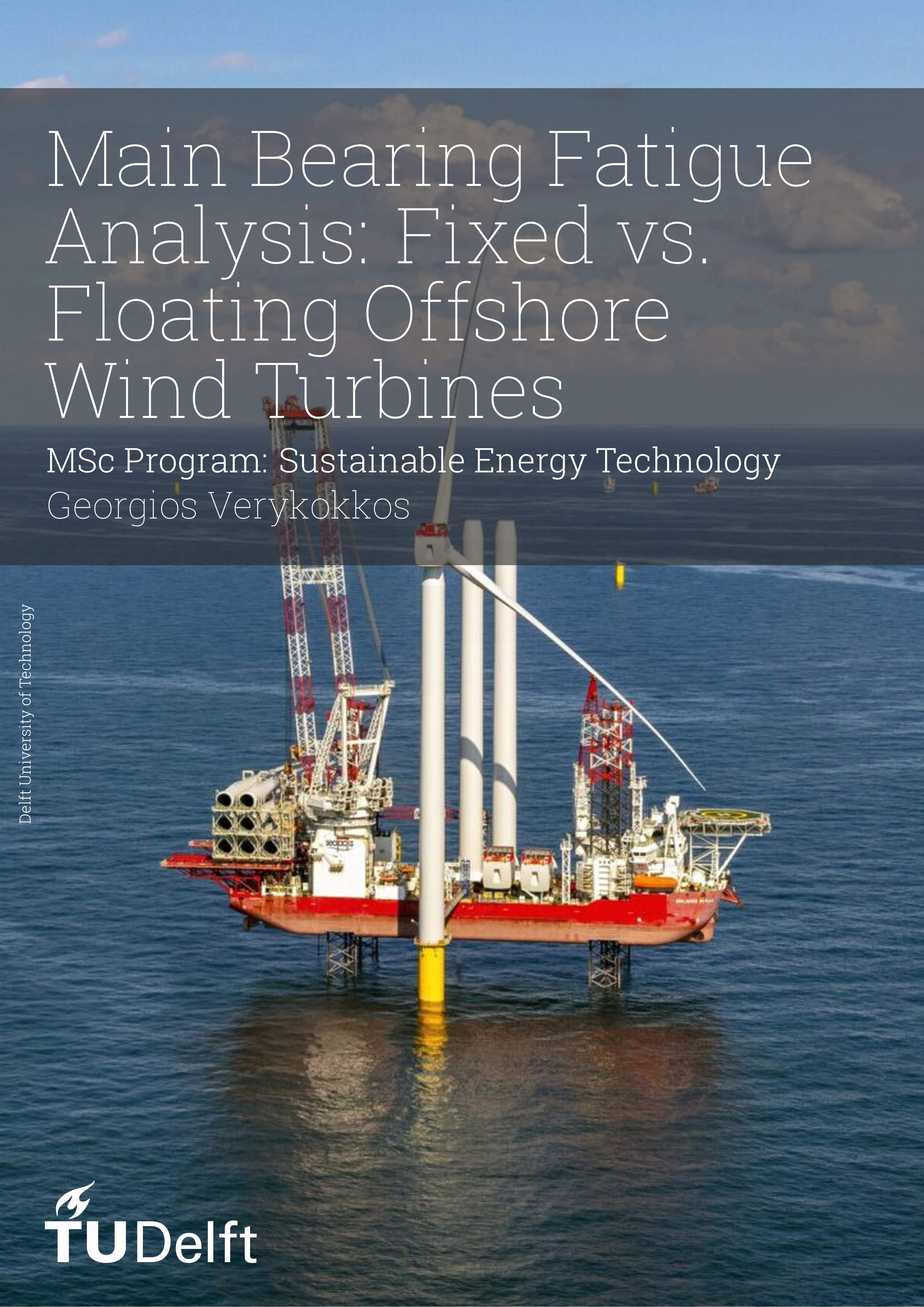

Delft University of Technology

TUDelft

Main Bearing Fatigue Analysis: Fixed vs. Floating Offshore Wind Turbines

by

Georgios Verykokkos

to obtain the degree of Master of Science in Sustainable Energy Technology
at Delft University of Technology.

Chair of Thesis Committee:	Dr.ir. M.B. (Michiel) Zaayer
Thesis Supervisor:	Dr. D. (Donatella) Zappalá
Thesis Committee Member:	Prof.dr.ir. R.C. (René) Alderliesten
Daily Supervisor:	Dr. S.K. (Sumit) Pal
Project Duration:	December, 2024 - August, 2025
Faculty:	Wind Energy Group, Faculty of Aerospace Engineering, Delft University of Technology, Faculty of Electrical Engineering, Mathematics and Computer Science, Delft University of Technology

Cover by: Ocean Energy Resources [1]

Acknowledgements

This thesis marks the end of my Master's studies at TU Delft. The past two years were filled with rewarding and challenging moments, which led to considerable personal and professional growth. In this section, I would like to thank a few people that made this journey special, through their contributions and support.

Firstly, I would like to express my sincere gratitude to my main and daily supervisors, Dr. Donatella Zappalá and Dr. Sumit Kumar Pal, for their valuable guidance and support, as well as their constructive feedback throughout this project. Their availability and encouragement helped me stay on track and motivated during the difficult and uncertain phases of this project. I am also grateful to Dr.ir Michiel Zaayer, the chair of my thesis committee, for the insightful comments and constructive feedback provided during the midterm review. Finally, I would like to thank Prof.dr.ir. René Alderliesten for being a member of my thesis committee.

Next, I would like to thank my close friends in the Netherlands and Greece for always being there to help me unwind and recharge during stressful and busy periods. This journey would not have been the same without the beautiful moments we shared.

In the end, my deepest thanks go to my parents and sisters for their unconditional support and for always believing in me through every phase of this journey and my life in general. Their encouragement was vital and helped me stay calm and focused throughout all the stages of this journey.

Georgios Verykokkos
Delft, August 2025

Abstract

Amid the global energy transition, offshore wind energy has been positioned as a pivotal technology, utilizing both bottom-fixed (BOWT) and floating offshore wind turbine (FOWT) configurations. Offshore wind turbines face high operation and maintenance (O&M) costs, representing up to 35% of the levelized cost of energy (LCOE), with the drivetrain and especially the main bearing (MB) being among the most failure-prone components, leading to long downtime and reduced energy production. In floating wind turbines, main bearings experience additional challenges due to combined wind and wave loads and the platform motions.

This research investigates the differences in loading and fatigue damage of the upwind main bearing (MB1) in a monopile BOWT and semi-submersible FOWT, both based on the DTU 10 MW reference wind turbine (RWT). Using OpenFAST simulations under Design Load Case (DLC) 1.2, according to Standard IEC 61400-1: 2019, this study calculates the MB1 loads for both wind turbine configurations, at a North Sea location east of Scotland, with a water depth of 60 m. Simulations are conducted across the full operating wind speed range (4.5 - 24.5 m/s), and loads are calculated through an analytical formulation. The axial and radial loads of MB1 are post-processed according to Standard ISO 281:2007, to compute the dynamic equivalent load, which is used to evaluate the fatigue damage of the main bearings. The Load Duration Distribution (LDD) method, which defines the load cycles, and the site-specific Weibull distribution are used to estimate the hourly fatigue damage of MB1, which is then extrapolated to a 20-year design lifetime, yielding the time-dependent Remaining Useful Life (RUL).

A comparative analysis of MB1 load means and standard deviations reveals that, for the examined drivetrain configuration, radial loads dominate the main bearing loading and fatigue contribution in both configurations. Specifically, for the FOWT, they represent 74 to 90% of the dynamic equivalent load and 39 to 72% of the fatigue damage across all operating wind speeds. For the BOWT configuration, the corresponding ranges are 75 to 90% and 42 to 72%, respectively. MB1 of the FOWT experiences higher axial and radial loads, mainly due to platform surge and pitch motions, which increase rotor thrust and amplify the axial loading, as well as platform sway, roll and yaw motions that mainly amplify the radial loads. The largest load differences between FOWT and BOWT are encountered at around the rated wind speed of 11.4 m/s, and they peak at 13.5 m/s, where the FOWT axial load is 13.17% higher than in the BOWT.

Over the 20-year lifetime, MB1 in the FOWT accumulates 5.03% more fatigue damage, failing at 11.98 years, compared to 12.58 years for the BOWT. BOWT MB1 exhibits higher fatigue damage in the below-rated wind speed region, especially for wind speeds below 8.5 m/s. For aligned wind-wave cases, the reduction in the MB1 damage for both FOWTs and BOWTs is only 0.6% compared to realistic (misaligned) cases, indicating that, the wind-wave misalignment for wind speeds in the above-rated region, has a slight influence on the cumulative damage. A parametric sensitivity analysis shows that turbulence intensity is the most influential environmental factor: a change from Class A to C results in up to 10% reduction in MB1 damage. Among system parameters, platform mass significantly affects MB1 fatigue in FOWTs, with a 20% increase in mass reducing damage by 5.6%, while a 20% decrease increases it by 4.4%.

Overall, the findings of this thesis prove that MB loads in floating wind turbines are subjected to greater complexity and amplification, due to platform motions and aerodynamic, hydrodynamic, structural and control coupling. This results in increased fatigue damage and indicates the importance of advanced fatigue-aware, system-integrated control strategies that consider the platform dynamics to ensure main bearing reliability in future floating wind developments. The study concludes with recommendations for future work, including the validation of the results with field data, the exploration of alternative drivetrain layouts and the implementation of advanced control schemes to mitigate the impact of the platform motion.

Contents

List of Figures

List of Tables

Nomenclature

Abbreviations

Abbreviation	Definition
BEM	Blade Element Momentum
BOWT	Bottom-Fixed Offshore Wind Turbine
CAGR	Compound Annual Growth Rate
CBM	Condition-Based Maintenance
CCW	Counter Clockwise
CMS	Condition Monitoring System
COP	Conference of Parties
CRB	Cylindrical roller bearing
CW	Clockwise
DHI	Dansk Hydraulisk Institut
DLC	Design Load Case
DLL	Dynamic link library
DOF	Degree of Freedom
DSRB	Double-row sherical bearing
DTRB	Double-row tapered roller bearing
DTU	Danmarks Tekniske Universitet
DLC	Design Load Case
DOF	Degree of Freedom
FA	Fore-Aft
FFT	Fast Fourier Transform
FOWT	Floating Offshore Wind Turbine
HSS	High Speed Shaft
IEC	International Electrotechnical Commission
IPCC	Intergovernmental Panel on Climate Change
IRENA	International Renewable Energy Agency
ISS	Intermediate Speed Shaft
JONSWAP	Joint North Sea Wave Project
LC	Load Case
LCOE	Levelised Cost Of Energy
LDD	Load Duration Distribution
LSS	Low Speed Shaft
LT	Long-term
MB	Main Bearing
MB1	Upwind main bearing
MB2	Downwind main bearing
MBS	Multibody Simulation
MIS	Misalignment
MSL	Mean Still Level
MUL	Multidirectional
NREL	National Renewable Energy Laboratory
NSS	Normal Sea State
NTM	Normal Turbulence Model
NWLR	Normal Water Level Range
O&M	Operation and Maintenance
PDF	Probability Density Function

Abbreviation	Definition
PV	Photovoltaic
RMS	Root Mean Square
RNA	Rotor Nacelle Assembly
ROSCO	Reference Open-Source Controller
RPM	Revolutions Per Minute
RUL	Remaining Useful Life
RWT	Reference Wind Turbine
SCADA	Supervisory Control and Data Acquisition
SKS	Station Keeping System
SS	Side-to-Side
SRB	Spherical roller bearing
ST	Short-term
Std	Standard Deviation
TLP	Tension Leg Platform
TorRB	Toroidal roller bearing
TRB	Tapered roller bearing
TSR	Tip Speed Ratio
UNFCCC	United Nations Framework Convention on Climate Change
WT	Wind Turbine

Symbols

Symbol	Definition	Unit
AM	Additional mass matrix	[kg]
b	Factor b of Normal Turbulence model	[m/s]
B	Number of rotor blades	[-]
c	Chord length	[m]
C	Hydrodynamic damping matrix	[-]
C_α	Added mass coefficient	[-]
C_d	Drag coefficient	[-]
C_D	Dynamic load rating	[N]
C_l	Lift coefficient	[-]
C_m	Inertia coefficient	[-]
$C_{p,max}$	Maximum power coefficient	[-]
d	Water depth	[m]
$D_{accumulated}$	Accumulated damage	[-]
D_{hourly}	Hourly damage	[-]
D^{LT}	Long-term damage	[-]
D^{ST}	Short-term damage	[-]
dD	Drag force	[N]
dL	Lift force	[N]
dr	Distance of the blade element from the blade root	[m]
dt	Timestep	[s]
F_1	Reaction force of the upwind main bearing	[N]
F_2	Reaction force of the downwind main bearing	[N]
f	Frequency	[Hz]
F_a	Axial load	[N]
F_r	Radial load	[N]
F_x	Force in x- direction	[N]
F_y	Force in y- direction	[N]
F_z	Force in z- direction	[N]
F_{ext}	External loads vector	[-]

Symbol	Definition	Unit
F_{HD}	Hydrodynamic loads	[N]
F_{HS}	Hydrostatic forces	[N]
F_{moor}	Restoring loads by mooring lines	[N]
F_{wind}	Wind loads	[N]
F_n	Normal force on the plane of rotation	[N]
F_t	Tangential force on the plane of rotation	[N]
h	Wave height	[m]
H_s	Significant wave height	[m]
I_t	Turbulence Intensity	[-]
I_{ref}	Reference turbulence intensity	[-]
k	Shape parameter in Weibull distribution	[-]
K	Stiffness matrix	[N/m]
K_{moor}	Restoring stiffness matrix of mooring lines	[N/m]
K_{opt}	Optimal Load gain	[Nm/(rad/s)^2]
L	Distance	[m]
$L_{10,i}$	Bearing life	[revolutions]
L_K	Kaimal integral scale parameter	[-]
M	Mass matrix	[kg]
M_x	Moment about x- axis	[N]
M_y	Moment about y- axis	[N]
M_z	Moment about z- axis	[N]
n_i	stress cycles for every interval	[-]
n_{rotor}	Rotor rotational speed	[rpm]
P_i	Dynamic equivalent load for bin i	[N]
R	Resultant force or radius depending on the context	[N or m]
r_{gearbox}	Gearbox ratio	[-]
S_J	JONSWAP spectrum	[m^2/Hz]
S_K	Kaimal spectrum	[m^2/Hz]
T	Rotor thrust force or period (depending on context)	[N or s]
T_{HSS}	HSS-Generator torque	[N · m]
t_{nom}	Nominal life	[yrs]
T_p	Peak spectral period of wave	[s]
u	Transverse constituent of velocity	[m/s]
U	Wind speed	[m/s]
U_{10}	Wind speed at 10 m	[m/s]
U_{ave}	Average wind speed	[m/s]
U_{hub}	Wind speed at the hub height	[m/s]
U_r	Wind speed at the rotor	[m/s]
V_{res}	Resultant wind speed	[m/s]
V_{sub}	Displaced volume	
X	Dynamic radial load factor	[-]
Y	Dynamic axial load factor	[-]
z	Altitude- height	[m]
z_0	Roughness length of the surface	[-]
ζ_α	Amplitude of wave elevation	[m]
z_{ref}	Reference height-altitude	[m]
α	Angle of attack	[°]
α_{ind}	Induction factor	[-]
α_p	Power law or wind shear exponent	[-]
α_{scale}	Scale parameter in Weibull distribution	[m/s]
Γ	Gamma function	[-]
$\eta_{gearbox}$	Gearbox efficiency	[-]
θ	Section pitch angle	[°]
λ	Wave wavelength	[m]

Symbol	Definition	Unit
λ_{design}	Design tip speed ratio	[-]
ρ_{air}	Air density	[kg/m^3]
ρ_w	Water density	[kg/m^3]
σ	Standard deviation	[-]
ϕ	Inflow angle	[°]
Ω	Rotational speed of the rotor	[rad/s]
Ω_{LSS}	LSS-rotor rotational speed	[rad/s]
ω_{HSS}	HSS-generator rotational speed	[rad/s]

1

Introduction

Climate change is no longer a distant threat, it is a major issue influencing the world. Rising global temperatures, extreme weather phenomena, melting glaciers, and elevated sea levels are just a few of the evident outcomes of the human-induced climate crisis, according to the Intergovernmental Panel on Climate Change (IPCC) [2]. In recent decades, there have already been concerns about climate change leading to Conference of Parties (COP) events [3], among which the events in Kyoto, 1997 and Paris, 2015 could be distinguished. In the latter assembly, the Paris Agreement was adopted, which set the target of limiting the global average temperature increase to well below 2 °C above pre-industrial levels and pursue efforts to restrict the temperature raise even further, to 1.5°C [4]. The achievement of this goal would avert the expansion of the detrimental impacts of the climate change and would ensure the viability of planet Earth. As a result, the global energy landscape demands a radical and immense transformation that involves the elimination of fossil fuels and the transition to renewable energy sources.

To that end, World Energy Transitions Outlook 2024 by the International Renewable Energy Agency (IRENA) [5] outlines a vision for reshaping the worldwide energy framework in accordance with the aforementioned targets. Specifically, it presents a strategy to limit the temperature increase to 1.5 °C and attain net-zero emissions by 2050. In 2023, renewable power capacity was increased by 473 GW, compared to the addition of 298 GW of renewable energy technologies in 2022. To comply with the Paris Agreement, the total renewable power capacity by 2030, should amount to 11.2 TW [5]. According to IRENA's 1.5 °C scenario, by mid-century, 91% of the global electricity must be generated by renewable energy sources, with PV systems and wind energy making up almost 70% [5]. As the Global Wind Energy Council (GWEC) shows in Global Wind Report 2024 [6], in 2023, 106 GW of onshore wind and 10.8 GW of offshore wind were installed globally. This number is estimated to reach 791 GW of total new wind capacity added until 2028, with Compound Annual Growth Rate (CAGR) of almost 10%. The projected annual new wind capacity is illustrated in Figure 1.1 [6].

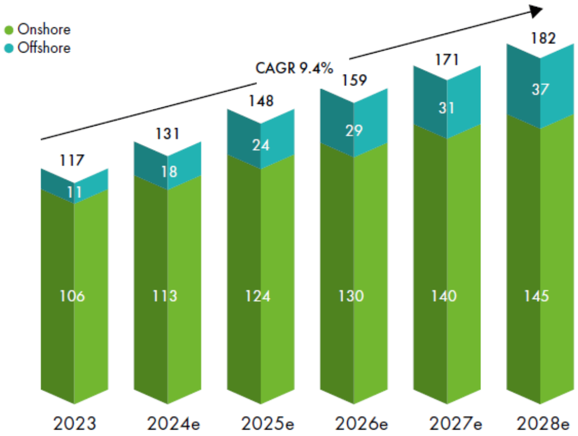

Figure 1.1: New wind energy installation outlook between 2023 - 2028 [6]

As can be observed in Figure 1.1, the future wind development strongly depends on offshore wind turbines (CAGR of 27.4% for the time period between 2023 and 2028), since onshore wind development has already been saturated in some countries, due to visual and noise constraints [7]. In contrast, these constraints are less limiting in offshore locations, allowing the utilization of numerous wind turbines (WTs) with larger rotor diameters. Subsequently, larger rotor diameters result in increased swept area of wind turbines and consequently higher aerodynamic torque, leading to higher wind power generation. There are two broad categories of offshore wind turbines, bottom-fixed offshore wind turbines (BOWTs) and floating offshore wind turbines (FOWTs), with considerable differences in their installation and loading. BOWTs constitute the majority of offshore wind farms and are installed in shallow waters, being economically viable and feasible at a water depth of up to almost 60 m. FOWTs are placed in deeper waters, where BOWTs become uneconomic [8, 9, 10]. Moreover, according to IRENA, the capacity factors of offshore wind farms are anticipated to increase between 43% and 60% globally [11]. This outlook is supported by projects such as HyWind Scotland, the first commercial floating wind farm, which achieved an average capacity factor of 54% during its first five years of operation [12] by accessing superior wind resources in deeper waters. However, along with the huge potential of offshore wind turbines, come the increased operation and maintenance (O&M) costs, which can amount up to 35% of the total cost of wind energy [13, 14]. Therefore, this is a key area of cost reduction for BOWTs and FOWTs, which would render them more economically attractive.

Wind turbine (WT) drivetrains and especially main bearings (MBs) are among the components of a wind turbine with the most frequent need for repair or maintenance. They suffer significant impact loads that severely affect the availability and power production of wind turbines [14]. FOWTs, unlike their bottom-fixed counterparts, must withstand a unique combination of loads due to platform motions. These platform motions, caused by both wind and wave conditions, pose several additional challenges to the fatigue of their main bearings [15]. In the literature, there is no existing comparison between BOWTs and FOWTs with respect to the fatigue analysis and loads of their main bearings. Consequently, it is crucial to assess their fatigue damage to identify the mechanisms and the differences of the two WT configurations.

1.1. Research objective and questions

The main objective of this thesis is to compare the fatigue damage experienced by the main bearings of bottom-fixed and floating offshore wind turbines and to identify the most prominent differences in their loading behavior. By comparing these two categories of wind turbines, this research aims to determine the influence of the platform motions on the main bearing loads and fatigue damage accumulation for the FOWTs, with the ultimate goal of identifying performance and fatigue mechanisms that could affect maintenance costs and energy yield.

This investigation directly addresses a pressing challenge in the field of sustainable energy technology: ensuring reliable and cost-effective offshore wind deployment in both shallow and deep water locations. Since MB failures are among the most critical drivers of unplanned and significant O&M costs, understanding their loading and fatigue damage behavior has strong implications for reducing the levelized cost of energy (LCOE) and improving the long-term economic viability of offshore wind energy.

This study provides practical insights that support system-level integration. The findings improve understanding of MB fatigue behavior, leading to better maintenance planning strategies such as optimized inspection intervals and predictive maintenance schedules. The research identifies platform-specific load patterns that provide essential data for component design optimization. These load patterns are specifically important for developing bearing specifications and control strategies tailored to different offshore wind configurations. These contributions strengthen the competitiveness of FOWTs in deep-water markets where BOWTs are not feasible, thus supporting large-scale expansion of offshore wind energy. Furthermore, the study highlights how improved MB reliability contributes not only to technical performance, but also to supporting sustainable energy transitions at system scale.

This thesis uses an established aero-hydro-servo-elastic coupling dynamic model of the DTU 10 MW Reference Wind Turbine (RWT) in two configurations: a bottom-fixed monopile and a semi-submersible floating substructure. The models consider the flexibility of the tower and blades and the stochastic loads of wind and waves. Various Design Load Case (DLC) 1.2 conditions are simulated in OpenFAST, for a specific North Sea location at 60 m water depth. MB loads are calculated through an analytical formulation using OpenFAST outputs, and MB fatigue damage is calculated using the Load Duration Distribution (LDD) methodology.

Given this context and methodology, this thesis addresses the following primary research question:

“How do the loading and fatigue damage of the main bearing differ between bottom-fixed and floating offshore wind turbines, and what is their sensitivity to environmental and system parameters?”

The main research question can be divided into the following sub-questions, that are investigated during the project:

1. How can the loads on the main bearings be estimated, and which loads have the greatest influence on the main bearings of floating and bottom-fixed offshore wind turbines?
2. What is the impact of the platform motion in floating wind turbines on main bearing loading compared to the bottom-fixed configurations?
3. How can fatigue damage of main bearings be calculated and what are the primary factors driving it in both wind turbine configurations?
4. Which environmental and system parameters have the greatest impact on the fatigue damage of the main bearings?

1.2. Report outline

The report begins with a literature review in Chapter 2, covering main offshore wind turbine categories, O&M strategies and established drivetrain and main bearing layouts. Chapter 2 also reviews main bearing load and fatigue assessment methodologies. Then, Chapter 3 provides a detailed overview of the methodology, an introduction to OpenFAST and the relevant fundamental theoretical background of wind and wave loading. Next, the case study investigated in this thesis is explained in detail in Chapter 4, while Chapter 5 presents the results of the methodology implemented in this thesis. Specifically, results related to the main bearing loads and their fatigue damage are presented. A parametric sensitivity analysis examines environmental and system parameters, and their impact on the main bearing fatigue damage. The report continues with Chapter 6, which further discusses the results and their implications. Finally, Chapter 7 concludes the thesis by summarizing the key findings and providing recommendations for future work.

2

Literature Review

This chapter provides an overview of the fundamental aspects of offshore wind turbines O&M, their main bearings and the methods to calculate their loads and fatigue damage. It starts in Section 2.1, with the classification of offshore wind turbines, differentiating between bottom-fixed and floating types. In Section 2.2, the foremost categories of O&M are briefly explained, followed by the presentation of the key WT subsystems and common failure areas in Section 2.3. Next, in Section 2.4 and Section 2.5, typical drivetrain and main bearing configurations are discussed, respectively. Then, Section 2.6 briefly presents methods for calculating main bearing loads and fatigue damage, as found in the literature. The chapter concludes, in Section 2.7, identifying the research gap and briefly explaining how this thesis addresses it.

2.1. Offshore wind turbines

In the introduction, it was already highlighted that offshore wind energy has taken considerable steps toward expanding as a major energy source in the future. With respect to offshore wind turbines, various categories can be distinguished and their foundation types differ depending on the water depths where they are installed. In Figure 2.1, different foundation types of offshore wind turbines are illustrated, accompanied by their theoretically applicable depths, according to DHI Group [16].

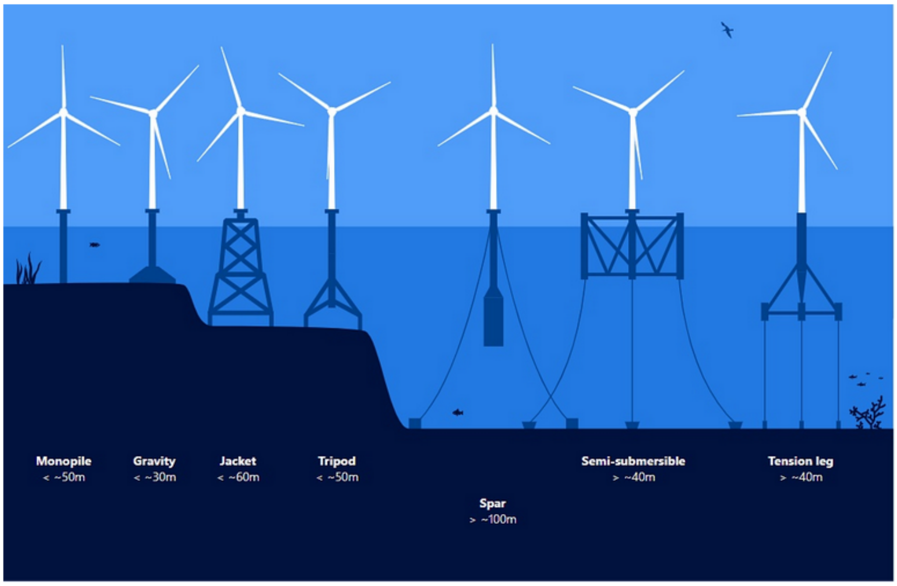

Figure 2.1: Typical offshore WT foundation types and applicable water depths [16]

As shown in Figure 2.1, BOWTs are split into gravity, monopile, jacket and tripod foundation type, that are elaborated further below [17]:

- **Gravity-based foundation:** Gravity-based foundations ensure their stability with their weight without the need for additional anchoring. Usually constructed from reinforced concrete or steel, they are suitable for shallow depths of up to 30 m. Although they are economical, their large weight limits their application in deeper waters.
- **Monopile:** Monopile foundations are the most frequently used support structures for offshore wind turbines, since they represent approximately 80% of global offshore wind farms [18], especially at water depths of up to 50 m. They consist of a wide-diameter steel pile inserted into the seabed, offering a straightforward and economical solution. Their simple installation and production processes make them very popular in offshore wind projects.
- **Jacket-based foundation:** Jacket foundations consist of a lattice structure with several supports, ensuring strong structural integrity, which makes them appropriate for water depths ranging from 30 to 80 m. Jacket foundations are favored in harsher seabed conditions and deeper waters, where monopiles are not feasible.
- **Tripod:** Tripod foundations are intended for offshore wind turbines installed in water depths ranging from 25 to 50 m. They comprise a central steel tube linked to three supporting legs, forming a triangular framework that enhances stability. Their high structural rigidity limits wave-induced motions, thereby improving their overall reliability.

On the other hand, FOWTs are divided into spar, semi-submersible and tension foundation types, as shown in Figure 2.1. These FOWTs are briefly explained below [19]:

- **Spar:** Spar platforms are ballast-stabilized floating foundations, typically used in deep waters higher than 100 m. By lowering the center of gravity using ballast water, which restricts pitch and roll motions, their stability is achieved. However, pitch motion remains a critical design challenge, as it can affect wind turbine operation.
- **Semi-submersible:** Semi-submersible offshore wind turbines maintain their stability by balancing between weight and buoyancy. The arrangement of buoyant pontoons and hydrostatic restoring forces achieves this stability by limiting movements such as heave, pitch, and roll. These platforms include large water-plane areas and small drafts, making them highly resistant to wave-induced motions. Their application fluctuates from 40 m, where they may not be cost-effective, to deeper waters. Semi-submersible platforms represent the most widespread type of FOWT, accounting for approximately 57% of the global floating offshore wind energy market in 2024, according to the most recent recorded data [20].
- **Tension leg :** Tension Leg Platforms (TLPs) are mooring-stabilized floating wind turbine foundations, designed for deep waters (40 m - 1000 m). They consist of a central buoyant platform anchored to the seabed with tensioned tendons, which confine motion in roll, pitch, and heave, while minimizing vertical motion. However, the demand of specialized vessels for the installation of TLPs and their dependence on vertical-load anchors amplify their costs.

Despite the theoretical range of water depth for the installation of the diverse offshore WT showcased in Figure 2.1, a water depth of approximately 60 m is generally considered the turning point beyond which FOWTs become more cost-effective than bottom-fixed solutions [21]. Therefore, this is the water depth considered in this thesis, to evaluate and compare the MB loads between a monopile BOWT and a semi-submersible FOWT, which are the prevalent offshore WT types, under similar environmental conditions.

Having presented the main offshore WT foundation types, the next section explores the O&M aspects that affect the performance, reliability and cost-effectiveness of offshore WTs.

2.2. Operation and Maintenance

Despite the promising further development of offshore wind energy, O&M of offshore WTs remains a significant technical and economic challenge. Harsh maritime conditions, weather-related access delays, and the requirement for specialized personnel and vessels contribute to high costs. Maintenance represents the highest proportion of O&M expenditure, including all activities necessary to keep a wind turbine operating within acceptable performance limits throughout its lifetime [22]. In offshore wind projects, O&M costs are estimated between 20 and 35% of the LCOE of wind, compared to 5 to 10% for the onshore wind farms [23, 24, 25].

Maintenance strategies are classified into two main types, corrective and preventive, depending on the time that maintenance takes place [14]. Corrective maintenance is performed after an issue in the system has occurred, while preventive actions aim to prevent the occurrence of a problem. Corrective maintenance is divided into immediate and deferred maintenance, according to the urgency of the problem that arises. Preventive approaches include time-based maintenance and condition-based maintenance (CBM). The former type follows predefined intervals independent of the operating condition of the wind turbine. Specifically, in offshore wind farms, WTs are serviced yearly during spring or summer [26]. CBM is based on real-time condition monitoring systems (CMS) and Supervisory Control and Data Acquisition (SCADA) data. [14]. In the context of drivetrain components, such as MBs, CBM facilitates early fault detection and helps mitigate the risk of severe failures, although major replacements remain challenging corrective tasks.

Particular attention should be given to the maintenance strategies of FOWTs, which are located in deep waters, far from shore. Their maintenance costs in 2023 were calculated to be 44,000 $/MW/year [27], while maintenance downtime can range from a few days for a routine maintenance to more than three months for more extensive maintenance [28]. According to McMorland et al. [29], there are two primary maintenance strategies in FOWTs to reduce downtime and costs while enhancing their reliability: tow-to-shallow waters and tow-to-shore. Katsouris and Marina [30] demonstrated the first approach. They showed that towing turbines to shallow areas for maintenance could reduce O&M costs by 35%. The second strategy, tow-to-shore, is meant for heavy component replacement. In this approach, the FOWT platform is disconnected from its mooring and electrical connections and towed to a near-shore port facility for maintenance or repair. Upon completion, the WT is towed back to its original offshore location [29, 31, 32]. This method was also implemented in the first major maintenance required for the Hywind Scotland wind farm, the first floating wind farm in the world, operating since 2017 in the North Sea, 24 km off Peterhead, Scotland [33]. Five wind turbines of 6 MW each, were towed back to Wergeland port on the west coast of Norway, where their main bearings were replaced, after seven years of operation, resulting in four months of downtime [34, 35].

2.3. Wind Turbine Failure Areas

Following the analysis of the most common maintenance strategies, this section examines the most critical failure areas of wind turbines. Particular attention is given to the drivetrain and main bearings, as their reliability strongly influences overall turbine performance and O&M costs.

2.3.1. Wind Turbine Subsystems

Wind turbines consist of multiple interrelated subsystems, each with specific functions. Li et al. [36], in their review of onshore wind turbines and FOWTs, present a detailed statistics on the foremost subsystems, their components, and their associated failure rates. The main subsystems include the rotor, electrical systems, pitch and yaw mechanisms, drivetrain, nacelle, and auxiliary equipment. Figure 2.2 illustrates the primary subsystems, as specified by Li et al. [36].

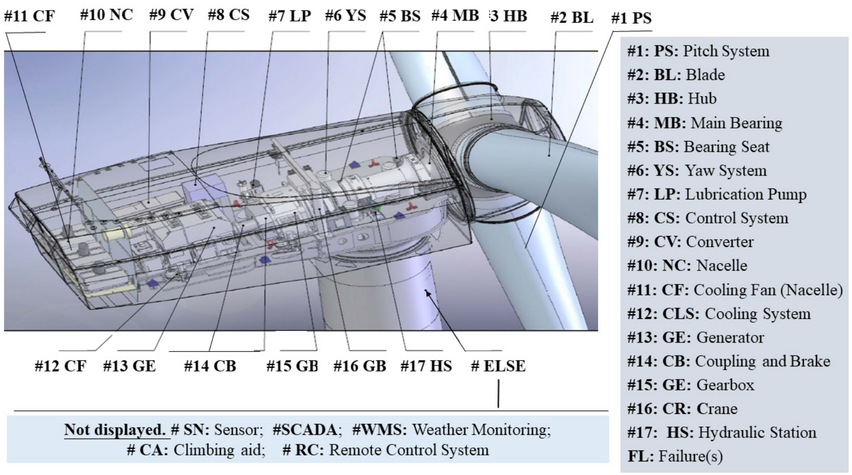

Figure 2.2: Main subsystems of a WT [36]

2.3.2. Failure definition and areas

In wind turbine research, failure is generally defined as an event that disrupts the normal operation of a WT. Wilkinson et al. [37] describe it as an event with downtime exceeding one hour that demands at least one manual restart of the WT, while Carroll et al. [38]define failure as an unplanned visit to a WT, to restore its functionality. Li et al. [36] further define failure as an event that stops the operation of WTs and triggers maintenance actions. Failures can be categorized as follows [36]:

- **Normal failures:** minor impact on WT productivity, easily repaired.
- **Critical failures:** reduced availability, necessitating prompt maintenance
- **Extremely critical failures:** complete turbine stoppage require extensive repair.

Reliability, closely related to failure, is defined as the probability that the system will perform a required function without failure under defined environmental and operating conditions for a predefined period of time [39].

WT operational and failure data are documented in multiple reliability databases, which often reveal inconsistencies in terms of data quality and availability, as there is no standardized procedure for WT reliability data collection [14]. Ribrant and Bertling [40] and Tavner et al. [41] focused on three of the most extensive and longest-standing European onshore WTs databases: the German WMEP (Wissenschaftliches Mess- und Evaluierungsprogramm), LWK (Landwirtschaftskammer) and the Swedish Elforsk/Vindstat. A comparison of these databases is illustrated in Figure 2.3, which shows the most frequent failure areas and those with the longest downtime. Failures related to the drivetrain and nacelle components, such as the gearbox and the yaw system, incur prolonged downtime in addition to their high repair costs [14, 41]. Reliability databases for offshore WTs, such as Offshore WMEP [42] and SPARTA (System Performance, Availability and Reliability Trend Analysis) [43], are also available. However, operational and failure data for FOWTs, which is the latest development in the offshore wind energy sector, are not yet sufficiently documented [36].

The gearbox is one of the most costly WT components with numerous failure incidents since the early stages of the wind energy industry [44]. According to Li and Soares [45], almost 70% of gearbox failures are caused by bearing failures. Following the gearbox, the main bearing is considered the second most significant reliability challenge, particularly regarding condition monitoring strategies and lubrication [46, 47]. Over a 20-year lifetime, main bearing failures have been reported to amount to 30% [48]. Moreover, main bearing failures appear to grow as a problem with the increasing size of wind turbines, as the main bearing interacts directly with the rotor and is subjected to dynamic loads from wind field variations and aerodynamic forces [46]. In the case of FOWTs, platform-induced motions intensify the fatigue and damage of the drivetrain components, particularly main bearings, due to combined wind and wave loading [49]. More specifically, the uneven load distribution on the drivetrain components leads to accelerated wear and increased maintenance requirements.

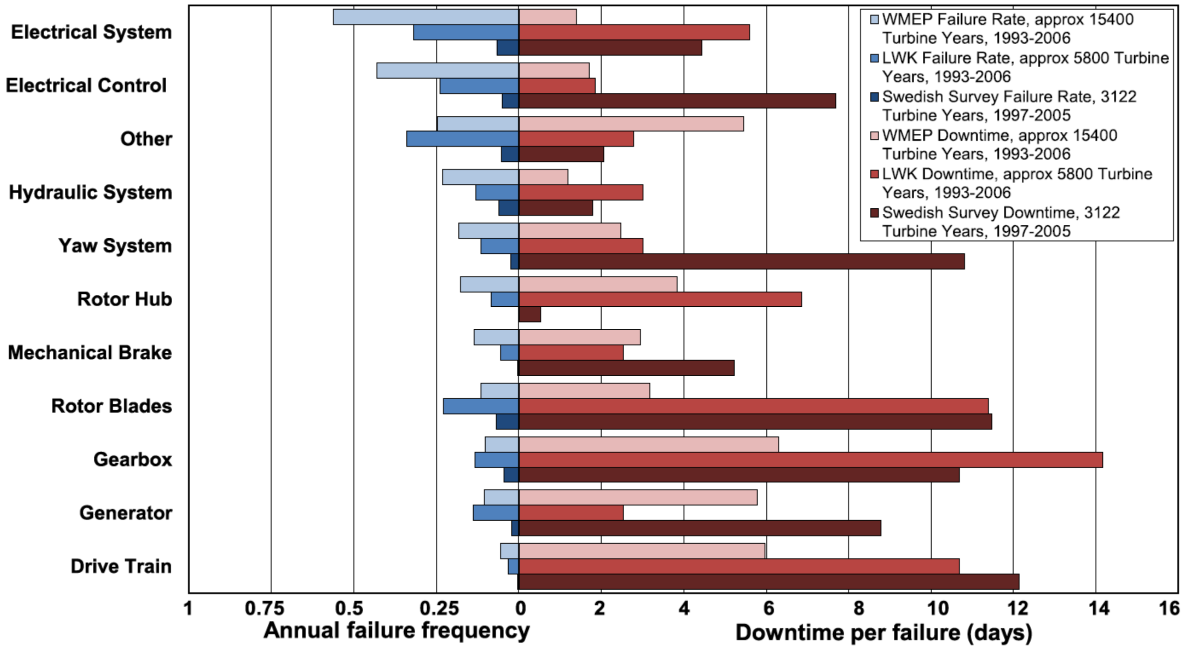

Figure 2.3: Failure rates and downtime for onshore WTs from various initiatives [14]

From a similar analysis, Li et al. [36] found that electrical subsystems, pitch and yaw system, cooling and hydraulics and the generator are involved in over 83% of the failures, with most occurring within the nacelle. These systems affect drivetrain performance through mechanical vibrations and variable loading conditions that accelerate component degradation. McMorland et al. [49] further noted that, in FOWTs, the main failure points include hydraulic systems, drivetrain units, and mooring lines, since the wave- and wind-induced fatigue aggravates these issues. Therefore, it is appropriate to examine the drivetrain in the following section.

2.4. Drivetrain systems: state of the art

This section provides an outline of drivetrains and their main features and. However, as this study does not focus on the specifics of drivetrain technology, further details can be found in the literature. Main bearing is part of the drivetrain, thus understanding drivetrain configurations is critical to evaluate MB fatigue behavior.

Drivetrain is the WT subsystem that converts the wind kinetic energy harnessed by the rotor into electrical energy produced by the generator. It transfers the loads from the rotor to the bedplate and the tower. To that end, it includes the whole power conversion system comprising the main bearing, the main shaft, the gearbox, the generator and the power converter, accompanied by the hub, bedplate and coupling for the connection and support of the sub-components. In the industry, there is a wide range of drivetrain technologies available with benefits and drawbacks varying in terms of aspects such as cost, weight, size, materials and manufacturing processes, efficiency, reliability and O&M needs [50]. Figure 2.4, by Nejad A. et al. [50], illustrates the schematic layouts of the two most commonly used WT drivetrains configurations: geared drive and direct drive (without gearbox) systems.

Geared drive systems incorporate a gearbox which increases the low rotational speed of the rotor and allows the reduction of the size and the inertia of the generator. Geared drivetrains can be divided into medium speed-hybrid and high speed systems [51, 52]. However, the presence of a gearbox can influence the WT reliability, increasing their non-operational period. Alternatively, in direct drive systems, the rotor is directly connected to the generator which rotates at the same speed as the rotor. In this case, the generator has significantly larger size to achieve a higher torque, but the system eliminates the high failure percentage due to the gearbox. This configuration comes with higher costs because of the larger size and subsequently mass of the generator. Both configurations can use different generator types, including permanent magnet synchronous and electrically excited machines [52].

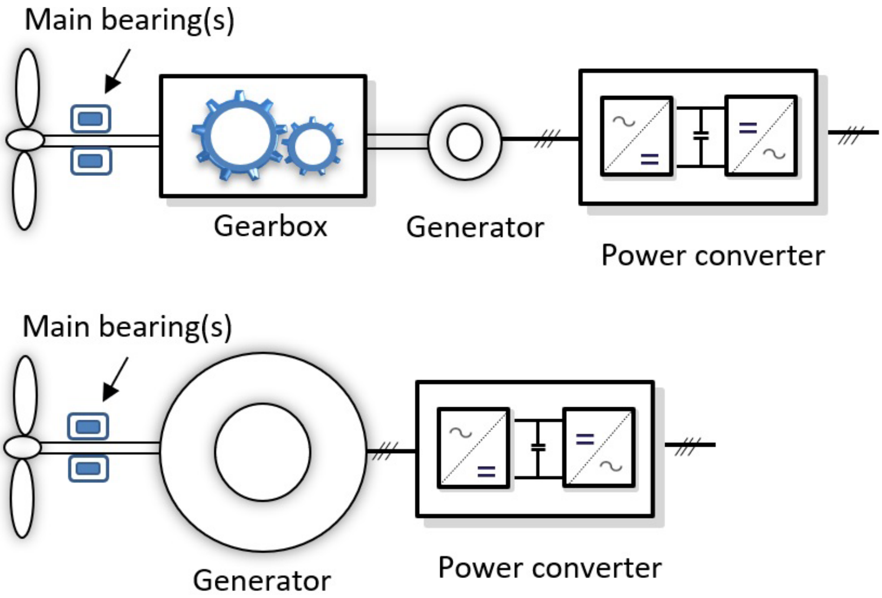

Figure 2.4: Layout of the two most common types of drivetrain configurations, with and without a gearbox (illustration by Nejad A. et al. [50])

For both drivetrain designs, drivetrain components are subject to mechanical vibrations and variable loads that affect their fatigue and reliability. These loads and operating conditions are presented in detail in the standards of the International Electrotechnical Commission (IEC), specifically IEC 61400-3-1 [53] and 61400-3-2 [54] for fixed and floating offshore wind turbines, respectively.

Regarding the main drivetrain components, gearboxes are designed at least for a 20-year life, as defined in the IEC 61400-4 design standards [55]. Yet, during actual operations, most of the WT gearboxes fail earlier than the nominal 20-year life. To accomplish the significant speed step-up necessary for the modern WT high-speed generators, typically three distinct stages in the gearbox are essential: a planetary stage connected to the Low Speed Shaft (LSS) for high torque transmission, followed by two parallel stages with helical gears on intermediate speed shaft (ISS) and the high speed shaft (HSS) [50, 24].

Generator systems transform kinetic energy from the wind into electrical energy via the drivetrain, with common types including permanent magnet, electrically excited magnet, induction, and doubly-fed induction generators [56]. Permanent magnet generators offer higher efficiency and reduced maintenance, while electrically excited and doubly-fed induction generators require more frequent maintenance due to components, such as slip rings and brushes [50, 24].

The power converter, located between the generator and the power grid, must satisfy the operational requirements of both. Common designs include two-level back-to-back converters, often combined in parallel for higher power ratings. Effective thermal management is critical, necessitating cooling systems [50].

After discussing the gearbox, generator, and power converter, the last key drivetrain component to address is the main bearing. Given its critical role in supporting the rotor, the following section examines the state of the art of main bearings.

2.5. Main bearings: state of the art

As discussed in Subsection 2.3.2, the main bearing is a critical drivetrain component, due to its high replacement cost, high failure frequency, and exposure to a complex combination of aerodynamic, gravitational, and inertial loads transmitted through the LSS. Consequently, this thesis focuses specifically on the MB. Moreover, MBs have been shown to be subjected to repetitive large-scale fluctuating loads, even during normal operation of the WT, which can be analyzed into axial and radial components [50]. In IEC Standard 63400-4: 2012 [55], the various types of bearings used in WTs are extensively described, according to the type of loads that they are able to withstand (axial, radial or combination), as well as their arrangements. Specifically for MBs, there are four widely used types of bearings, depending on their rolling elements, and three of them are shown in Figure 2.5 [46]:

- **Spherical roller bearings (SRBs):** In the SRBs, the outer raceway forms a section of a sphere. Subsequently, the rollers are designed so that they adhere tightly to both the inner and outer raceways. Consequently, SRBs are internally self-aligning and have a significant capacity to sustain radial loads. Additionally, a double-row SRB (DSRB) type, allows to carry combined axial and radial loading. However, SRBs are not suitable for the support of moment loads.
- **Tapered roller bearings (TRBs):** Single-row TRBs can carry combined axial and radial loads. They have truncated cones roller structures and different contact angles in the inner and outer raceways. The magnitude of the axial loading to be experienced determines the bearing contact angle. Akin to SRBs, TRBs are usually placed into double-row (DTRB) so that they boost their radial load carrying capacity.
- **Cylindrical roller bearings (CRBs):** CRBs have cylindrical rollers, usually curved at the ends to inhibit high edge stresses. They feature a high radial load capacity and they show low-friction compared to SRBs and TRBs, however, they cannot support axial loads. Similarly to the previous types, double-row types (DCRB) may be used to increase load carrying capacity.
- **Toroidal roller bearings (TorRBs):** TorRBs are similar to SRBs, but with a toroidal outer raceway and elongated rollers, being in this way capable to carry higher radial loads.

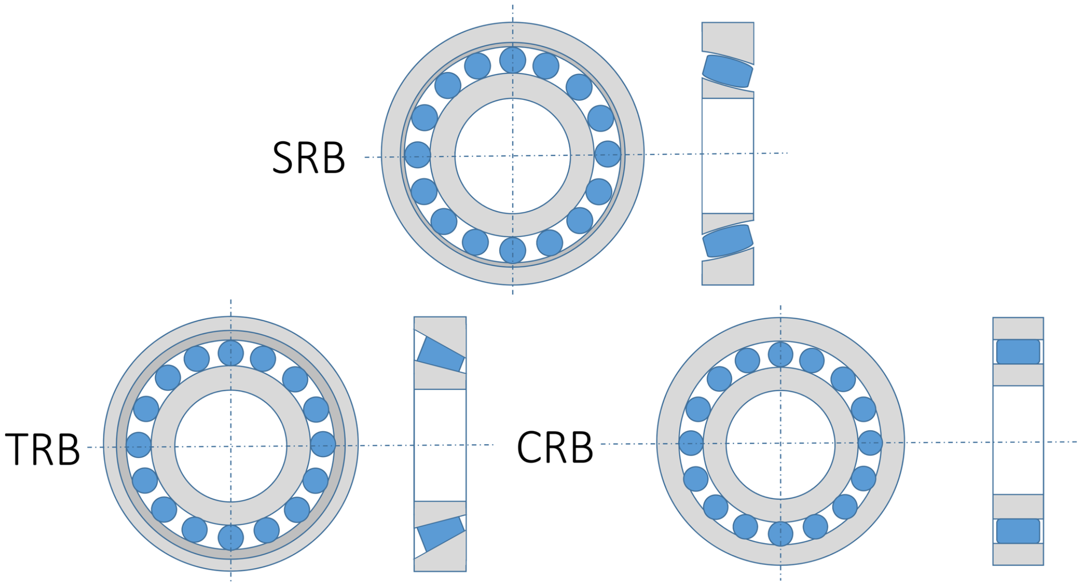

Figure 2.5: Single rows of bearing rolling element types [46].

Geared drivetrains differ in the use of one or two MBs, corresponding to three-point or four-point support, respectively. In a single MB arrangement, gearbox trunnions absorb loads on the gearbox side of the LSS, creating a three-point support. In a four-point support configuration (double main bearing), a second MB is placed close to the gearbox end of the LSS so that it counteracts the non-torque loads before they are transmitted to the gearbox. Further designs integrate the MB into the gearbox, eliminating the need for a main shaft, thus lowering tower-top weight and cost, however, causing potential early failures due to incompatibility between the gearbox (which functions as a main load path) and the remaining nacelle components. Finally, an emerging layout is the “floating drivetrain” design, in which two MBs mount the rotor on the bedplate, transmitting torque to the shaft via an elastic coupling and preventing the non-torque loads from reaching the gearbox. Although existing studies demonstrate lower gearbox failures for this design [57], there are not respective studies for MBs [46]. The aforementioned MB configurations of the geared drivetrain systems are depicted in Figure 2.6.

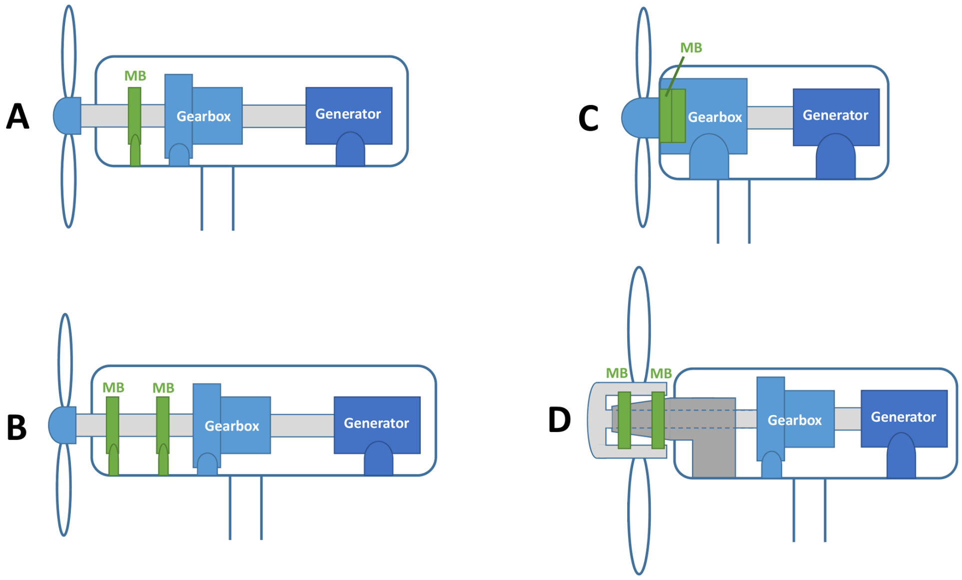

Figure 2.6: Existing drivetrain layouts for geared turbines, single main bearing (A), double main bearing (B), gearbox-integrated main bearing (C) and a “floating drivetrain” design (D) [46]

Direct drive systems include single, double or triple MB configurations with various arrangements, which are indicated in Figure 2.7. More details about these configurations can be found in the research of Stander et al. [58].

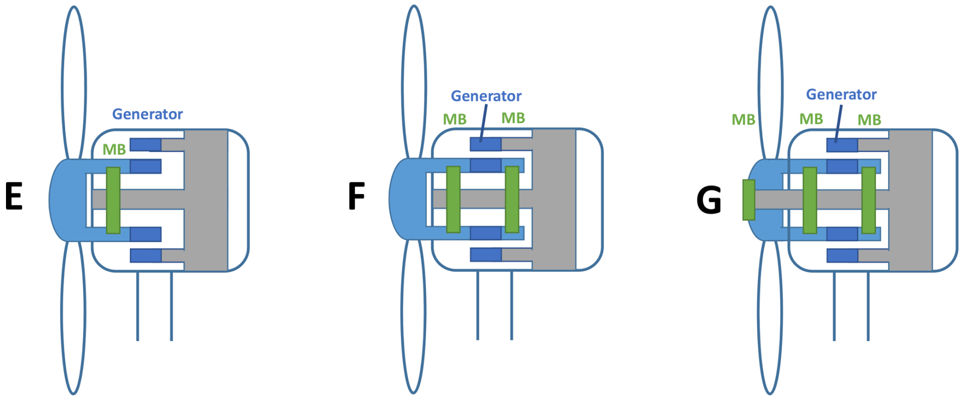

Figure 2.7: Existing drivetrain layouts for direct-drive turbines, including single-MB (E), double-MB (F) and triple-MB (G) design [46]

2.6. Main bearing loads and fatigue analysis in literature

The main bearing of offshore WTs, is subjected to combined and variable loading conditions, leading to frequent failures as described in the previous sections. The assessment of MB loads and fatigue damage is therefore critical. In the scientific literature, various methodologies have been explored to calculate the MB loads and evaluate its fatigue damage ranging from simplified analytical models to physics-based fatigue analyses and advanced coupled aero-hydro-servo-elastic simulations with detailed load post-processing. This section provides a concise overview of various MB load calculation and fatigue assessment methods, found in the literature.

2.6.1. Main bearing load calculations approaches

Main bearing load estimation in offshore wind turbines is typically performed using either high-fidelity time-domain simulations or analytical formulations. These approaches differ in their complexity, computational requirements, and precision.

High-fidelity simulation tools can capture the coupled dynamic behavior of the WT under a wind range of realistic operating and environmental conditions. Representative software platforms include:

- **OpenFAST** [59]: open-source aero-hydro-servo-elastic simulation tool widely used in academia and industry.
- **SIMPACK** [60]: multibody simulation (MBS) tool that enables high-fidelity drivetrain and bearing modeling.
- **Romax** [61]: commercial software for analysis and modeling of drivetrain and bearings.

In contrast, analytical approaches estimate MB loads from rotor or hub data and loads without requiring full drivetrain-model dynamic simulations. They typically include:

- **Geometric relationships**: including bearing position, shaft geometry, and contact angles.
- **Force-moment balances**: static or quasi-static equilibrium calculations.

Several studies have used these approaches, either individually or combined, to estimate the loads acting on the MB. Representative examples are briefly mentioned here, with further details available in the cited sources. Mehlan and Nejad [62] used OpenFAST to develop a global WT model and SIMPACK for drivetrain modeling, to calculate the main shaft and MB loads. Krathe et al. [63] modeled a WT drivetrain in OpenFAST, representing the MBs with springs, and subsequently calculating their loads and fatigue. Wang et al. [64] applied SIMPACK for drivetrain modeling and Romax to model the MBs and calculate their loads. Furthermore, Hart et al. [48] used Romax to model their WT drivetrain and its components (main bearing, main shaft, gearbox), and geometrical relationships and force-moment balances to estimate the MB forces. Finally, Hart et al. [65], Guo et al. [66] and Jiang et al. [67], using geometric relationships and force-moment balances, calculated the MB loads and, subsequently, their fatigue.

2.6.2. Main bearing fatigue damage and Remaining Useful Life estimation

Once the MB loads have been defined using either simulation-based or analytical approaches, the next step is to assess their impact on MB life. This is typically achieved through fatigue damage analysis methods, which quantify the accumulation of damage over time and create the basis for estimating the Remaining Useful Life (RUL) of the MB.

In the literature, there are typical models for the estimation of the MB fatigue damage, which are briefly described below.

- **ISO 281: 2007 bearing life equations** [68]: used to determine the basic rating life of the bearing, based on its dynamic load ratings and dynamic equivalent loads.
- **Load Duration Distribution (LDD)** [55]: used to categorize the loads by magnitude and duration to account for the load variability during operation.
- **Palmgren–Miner linear damage accumulation rule**: summation of individual damage from individual load cycles to calculate the total accumulated damage.

RUL estimation complements the damage calculation and predicts the time that corresponds to the end of life of the MB, under specific loading conditions. The importance of RUL approaches lies in their ability to estimate fatigue life based on load histories, without the need for field failure data. In the literature, RUL approaches can be classified as follows.

- **Physics-based**: combining MB load histories with bearing life models to project the MB remaining life until failure.
- **Data-driven** [69]: applying statistical models or machine learning methods to CMS data, to estimate the MB remaining life.

- **Hubrid** [70]: integrating physics-based models with data-driven techniques for improved accuracy.

Having outlined the most common approaches for estimating MB loads and, subsequently, their fatigue damage and RUL, the next section presents an example that integrates several of these methods. Specifically, it describes a Digital Twin model that provides real-time monitoring data. These data are post-processed, using data-driven techniques and a physics-based model, to estimate MB loads and calculate the real-time accumulated damage and RUL of the MB.

2.6.3. Digital Twin and Remaining Useful Life

Mehlan et al. [70], in their research, focused on virtual sensing of bearing loads in offshore WTs and the subsequent evaluation of the RUL utilizing physics-based techniques and Digital Twin technology, which offers the possibility of real-time monitoring and fatigue evaluation of the drivetrain components. Their methodology is described in short in Figure 2.8.

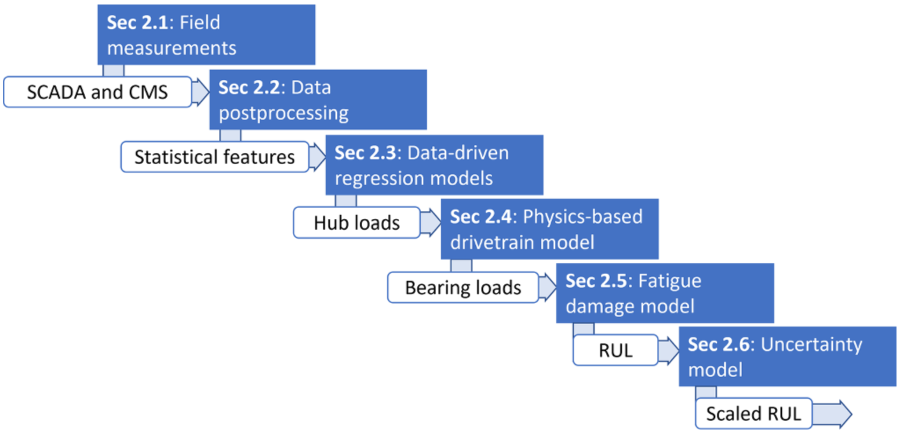

Figure 2.8: Complete methodology for virtual sensing of drivetrain loads and remaining useful life estimation [70]

Essentially, the developed framework consists of three fundamental layers, the data acquisition, a virtual model and the decision support. Firstly, real sensor measurements are derived from SCADA systems, (e.g. wind speed, rotor speed and power output) together with signals and vibration data from CMS, which are divided into 10-min intervals and post-processed to calculate statistical features such as mean values, standard deviation and root mean square (RMS). Specifically, field measurements from the U.S Department of Energy 1.5 MW research WT are used.

The virtual model layer integrates data-driven algorithms and physics-based models, which are explained in detail in their work [70]. Moreover, regression models, both linear (e.g., Linear Regression) and nonlinear (e.g., Support Vector Machines, Tree Ensembles) are implemented to calculate the loads at the rotor hub (torque, thrust, yaw and pitch moments), which are difficult to be directly measured. When these global loads are known, local bearing loads are estimated using analytical drivetrain models, specifically via moment balances and geometric parameters.

Fatigue analysis is then performed according to standardized methodologies. According to ISO 281: 2007 [68], the bearing lifetime $L_{10,i}$ is calculated as:

$$L_{10,i} = 10^6 \cdot \left(\frac{C_D}{P_i}\right)^m \tag{2.1}$$

where C_D is the basic dynamic load rating, given by the bearing manufacturer, (P_i) is the equivalent dynamic load, which is computed for 10-minutes average intervals, considering the axial and radial load of the main bearing and m is equal to 10/3 for roller bearings according to ISO 281: 2007 [68]. Next, the Palmgren–Miner linear damage accumulation rule is used to estimate the fatigue damage (D_i^{ST}) for every 10-min interval.

$$D_i^{ST} = \frac{n_i}{N_i} \tag{2.2}$$

N_i represents the permissible stress cycles, while n_i denotes the experienced stress cycles which are determined using the LDD method. The LDD method is prescribed by IEC 61400-4 [55] and is suitable for rotating elements, such as bearings and gears in contrast to structural elements, where the Rainflow Counting method is commonly used. At the rotating elements, apart from the loads to which they are subjected, their rotational speed influences the stress cycles, thus, LDD is applied to capture the magnitude and the duration of the loads.

The cumulative long-term fatigue damage (D^{LT}), which is tracked over time, arises from summation of the 10-min intervals damage as:

$$D^{LT}(t) = \sum_{i=0}^{t/\Delta t} D_i^{ST} \tag{2.3}$$

where t is the total time and Δt is the 10-min timestep. The RUL is, then estimated by comparing the accumulated damage with the nominal life (t_{nom}) of 20 years as follows.

$$\text{RUL}(t) = t_{\text{nom}} \cdot (1 - D^{LT}(t)) \tag{2.4}$$

Finally, despite the fact that 10-minute averaged data reduce computational costs and allow real-time monitoring, they can conceal high-frequency load fluctuations, which are more damaging due to the non-linear nature of fatigue. Consequently, the authors define an uncertainty factor as the ratio between the true short-term damage measured at 50 Hz and the short-term damage of the 10-min intervals. More information about their models is available in their paper [70].

2.7. Research Gap

This chapter has reviewed the main BOWT and FOWT types, followed by a short overview of their O&M activities and the most frequent WT failure areas. Furthermore, it has outlined the state-of-the-art in drivetrain systems and main bearing designs, while the challenges of the FOWTs in the MB loading and fatigue damage have been explained. Finally, several approaches for calculating the MB loads and their fatigue damage have been briefly explained.

Main bearing analysis for BOWTs has been widely investigated, with numerous studies establishing methodologies for MB load calculation and fatigue damage assessment, using both analytical and high-fidelity simulations. In contrast, MB analysis for FOWTs remains limited, largely due to the additional complexity added by platform motion. Although studies have explored general FOWT challenges, specific investigation of MB loads and fatigue damage is scarce. Particularly, there are no studies directly comparing MB loading patterns and fatigue damage accumulation between BOWTs and FOWTs.

This thesis addresses the literature gap by directly comparing MB loads and fatigue damage between BOWT and FOWT configurations using OpenFAST simulations under identical environmental conditions. It quantifies MB loading differences, analyzes MB fatigue damage for both WT configurations and evaluates its sensitivity to environmental and system parameters. Addressing this research gap has significant industry implications, since current main bearing designs for FOWTs rely mainly on BOWT experience, potentially leading to suboptimal designs. The findings provide essential insights for improved design and maintenance strategies adapted for the floating offshore wind sector. The following chapter outlines the methodology developed to address this literature gap.

3

Methodology and Theoretical Background

This chapter describes the comprehensive methodology developed in this study for evaluating MB loads and fatigue damage in offshore WTs, as well as the essential theoretical background. The methodology combines OpenFAST-based load analysis with physics-based damage estimation to investigate the differences in MB loading behavior and fatigue damage between BOWTs and FOWTs.

Section 3.1 outlines an overview of the methodology, presenting a workflow from inputs definition to OpenFAST simulations, MB load calculations and fatigue assessment. Section 3.2 introduces OpenFAST and its primary operations. Section 3.3 and Section 3.4 explain the essential physics governing wind and wave interactions, respectively, with offshore WTs. Next, Section 3.5 explains the principles of controller operation. The chapter ends with Section 3.6, which elaborates the post-processing methodology for converting simulation outputs into MB loads, fatigue damage and RUL estimates.

3.1. Methodology Overview

Figure 3.1 illustrates the overall methodology implemented in this thesis, including the input conditions, the simulation tool used, and the post-processing of the outputs to estimate the loads and the fatigue damage of the main bearings of the WTs.

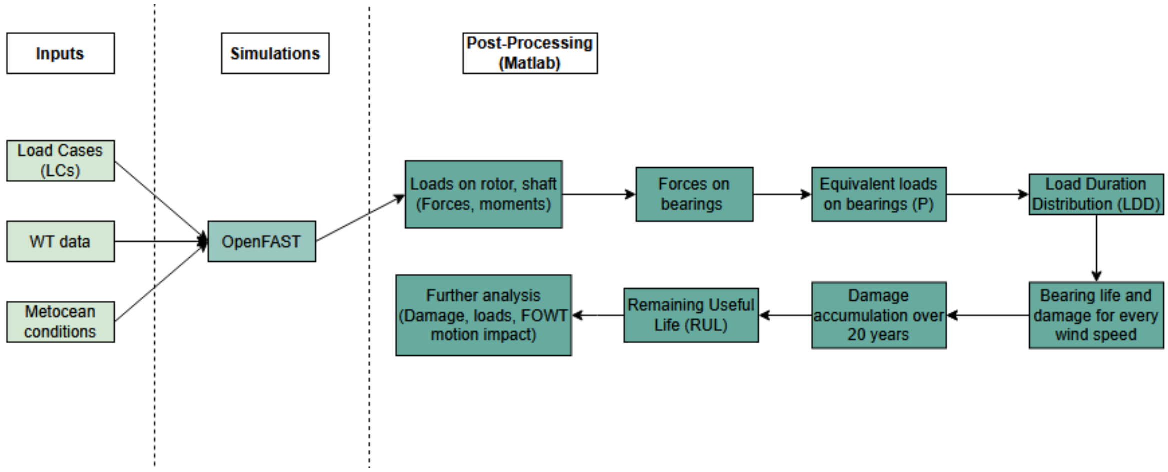

Figure 3.1: Overview of methodology

First, the input conditions must be defined before the simulations are performed. In particular, the data and specifications of the simulated WT models, the selected load cases, as well as the environmental metocean (wind and wave) conditions should be described. This chapter includes only some basic information on the simulated WT, which is necessary for the methodology, while more details on the simulation inputs are elaborated in Chapter 4, which presents the case study of this thesis. The simulations are then conducted in OpenFAST, which produces the loads acting on the hub and the main shaft of the WT. These loads are, in turn, used in the post-processing stage to calculate the forces and the equivalent loads on the main bearings. Subsequently, once the LDD method is implemented, the damage of the main bearings is calculated for every hourly simulation and wind speed and their RUL is calculated over a time horizon of 20 years.

Finally, a more in-depth load and damage analysis is carried out to achieve the thesis objective of identifying the main differences between BOWT and FOWT and the impact of the platform motions. First, a statistical evaluation of the MB loads and FOWT platform motion time series is conducted, based on their means and standard deviations. Secondly, the relationship between rotor aerodynamic performance and fatigue damage is analyzed, since the former affects rotor speed, which, in turn, influences load cycles and MB fatigue damage. In the end, a parametric sensitivity analysis is performed to identify the most influential factors affecting the MB fatigue damage. In this analysis, environmental and system parameters are varied, and their impact on MB fatigue damage is investigated.

In this thesis, the RUL methodology is used, since it offers a direct physics-based estimation of the remaining time until failure at component-level, such as the main bearings, based on load histories without the need for real failure databases or large-scale field failure data. Additionally, it allows the explicit comparison of MB loads and fatigue damage between BOWTs and FOWTs under the same environmental and operating conditions. The RUL methodology complies with the standard ISO 281: 2007 [68], applying established equations for the estimation of MB fatigue life, boosting its credibility and reproducibility.

The implementation of this comprehensive methodology requires a simulation platform capable of modeling the complex and coupled dynamics of wind turbines under realistic environmental conditions. OpenFAST serves as this simulation tool, since it is suitable for the aero-hydro-servo-elastic modeling of WTs and is widely used in academia and industry to simulate both BOWT and FOWT configurations. The following section introduces OpenFAST modules and their operations.

3.2. Introduction to OpenFAST

OpenFAST combines multiple modules connected and driven by a central “glue” code, that are suitable for the modeling of aerodynamics, servo-dynamics, hydrodynamics and other relevant aspects of a wind turbine [59]. For this study, OpenFAST was adopted to compute the dynamic loading of the drivetrain under different wind and wave conditions, by solving the fully coupled behavior of the rotor, tower, controller, and in the case of the FOWT, the floating platform at every simulation timestep.

Specifically, the seven modules used for the WT configurations of this thesis are briefly mentioned below:

AeroDyn

AeroDyn is used to calculate aerodynamic loads acting on the blades and tower utilizing the Blade Element Momentum (BEM) theory and actuator line theory. Detailed analysis of these theories can also be found in the book by Zaaijer and Viré [71]. AeroDyn inputs include environmental conditions, blade and airfoil data and control inputs. It also entails submodules that handle induction factors and wake effects [72].

HydroDyn

HydroDyn enables the calculation of hydrodynamic loads based on potential flow theory, strip theory, or a hybrid approach. Both linear wave theory and regular or irregular wave spectra can be used. In this thesis, irregular waves modeled via the Pierson-Moskowitz spectrum are used. Moreover, potential flow theory is used for the semi-submersible platform of the FOWT, while for the monopile BOWT the hydrodynamic loads are determined using the Morison equation for the fluid inertia, added mass and viscous-drag components [73].

ElastoDyn

ElastoDyn governs the structural dynamics of the rotor, tower, drivetrain and generator by applying Newton's laws across seventeen Degrees of Freedom (DOFs). Among its input data, the initial conditions, the wind turbine configuration, mass distribution and stiffness for tower and blades are included [74].

Inflow Wind

Inflow Wind is a module for processing wind inflow data and providing wind speed data at every blade node to AeroDyn. This module encompasses various wind file formats, such as steady wind, uniform wind and binary TurbSim full-field wind files [75]. For this project, turbulent wind fields are externally generated by TurbSim and introduced to InflowWind [76].

ServoDyn

ServoDyn models the turbine control strategy. It entails dynamic link libraries (DLLs) for various control strategies, including pitch control, torque control, nacelle yaw control, and HSS braking [77]. In this thesis, a torque and pitch control strategy is implemented.

MoorDyn

MoorDyn predicts the dynamic behavior of mooring lines in floating configurations. It employs a lumped-mass method to discretize the cable dynamics along the length of the mooring line and provides restoring forces and coupling with the platform [78].

SubDyn

SubDyn models the structural flexibility of the fixed substructure using finite-element analysis and a Craig-Bampton reduction method [79].

The interrelation of these modules allows OpenFAST to simulate the full WT system behavior, reflecting the interaction between between aerodynamics, hydrodynamics, structure, and control. The interconnection of the modules for the FOWT configuration is shown in Figure 3.2, where the MoorDyn is active, while the BOWT configuration, which uses the SubDyn, is depicted in Figure 3.3 [80].

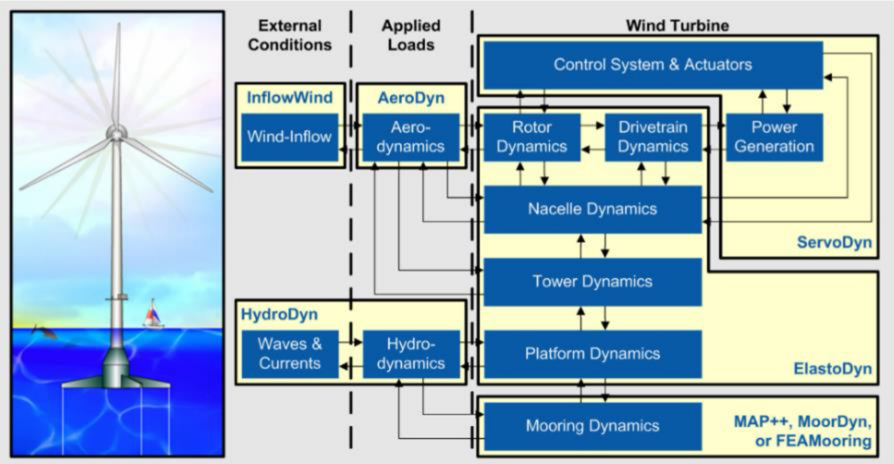

Figure 3.2: Full System FOWT OpenFAST module interconnections [80]

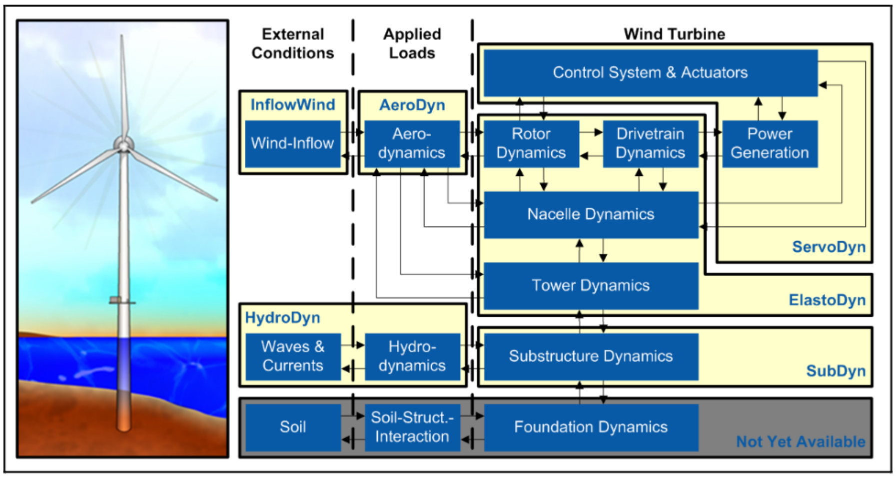

Figure 3.3: Full System BOWT OpenFAST module interconnections [80]

3.3. Wind Theory

3.3.1. Wind Physics

This section analyzes wind, a highly dynamic phenomenon, addressing various aspects of wind field modeling, as they are used in OpenFAST. Apart from wind speed and direction, often the most obvious characteristics of wind, there are other factors and parameters that define the wind state, such as wind shear and atmospheric turbulence. Current WTs, including the DTU 10 MW RWT, typically start operating at 3-4 m/s, while their generation stops at around 25 m/s, which is the cut-out wind speed [81]. These wind speeds refer to wind conditions at hub height, which differ from wind speeds at lower heights, such as 10 m, where standard meteorological measurements are often taken.

This difference is attributed to the wind shear, which describes a wind profile indicating the wind speed growth with respect to height from the surface. At low elevations, wind speed is affected by the surface roughness, which can reduce the wind speed in the case of high roughness values (e.g. buildings, trees in onshore applications). However, in offshore applications, the surface is relatively smooth, lowering the impact on the wind speed.

According to Standard International Electrotechnical Commission (IEC): 61400-3:2009 [82], the most commonly used wind profiles are the logarithmic profile and the power law profile, represented by Equation 3.1a and Equation 3.1b, respectively:

$$U(z) = U(z_{\text{ref}}) \cdot \frac{\ln(z/z_0)}{\ln(z_{\text{ref}}/z_0)} \qquad \text{(3.1a)} \qquad\qquad U(z) = U(z_{\text{ref}}) \cdot \left(\frac{z}{z_{\text{ref}}}\right)^{\alpha_p} \qquad \text{(3.1b)}$$

where U is the wind speed, z is the height above still water level, at which the wind speed value is desired, z_{ref} is the reference height above the still water level, at which the wind speed is usually known, z_0 is the roughness length of the surface, and α_p is an empirical power law or wind shear exponent, which depends on the atmosphere stability. For offshore locations, according to IEC:61400-3:2009, α_p = 0.14 [82]. These wind profiles can also be selected in the Inflow Wind input file.

Furthermore, wind can be either steady, meaning that it maintains a constant speed and direction over a specific time period, or turbulent which entails irregular fluctuations in wind speed and direction over short time intervals. Turbulence is critical for dynamic WT loading and is expressed by the turbulence intensity (I_t), which is defined as the ratio between the standard deviation (σ) of the time-varying wind speed and the mean wind speed (U) over the short-term time interval examined, as [71]:

$$I_t = \frac{\sigma}{U} \qquad \text{(3.2)}$$

Based on Standard IEC: 61400-1:2019 [83], wind turbines are classified into three classes, shown in Table 3.1, according to their average wind speed at hub height (U_{ave}) and their turbulence intensity

(I_{ref}), where class A is high turbulence, class B is medium turbulence and class C is low turbulence.

Table 3.1: Basic Parameters for Wind Turbine Classes [83]

Wind turbine class	**I**	**II**	**III**
U_{ave} (m/s)	10	8.5	7.5
A I_{ref} (-)	0.16		
B I_{ref} (-)	0.14		
C I_{ref} (-)	0.12		

In this thesis, turbulent wind conditions are externally modeled by TurbSim, a stochastic, full-field turbulent wind simulator which is utilized to generate randomized coherent turbulent structures around a specific mean wind speed [76], using Kaimal spectrum. Kaimal spectrum is widely used due to its effectiveness in characterizing atmospheric turbulence, is defined in standard IEC 61400-1:2019 [84] and is given in Equation 3.3, where σ is the standard deviation of the velocity, L_K is an integral scale parameter, f is the cyclic frequency and U is the mean wind speed at the hub height [76, 84]:

$$S_K(f) = \frac{4\sigma_K^2 \frac{L_K}{U}}{\left(1 + 6f\frac{L_K}{U}\right)^{\frac{5}{3}}} \tag{3.3}$$

3.3.2. Aerodynamic loads

Wind creates aerodynamic loads on wind turbines and these wind-induced forces affect the turbine's behavior. Thus, the mechanical loadings on the rotor-nacelle assembly (RNA) and subsequently on the main bearings are governed by the lift and drag forces acting on the blades.

AeroDyn uses Blade Element Theory (BEM) to calculate aerodynamic forces along each blade. BEM constitutes one of the most widely utilized aerodynamic solvers and is a combination of blade element and momentum theory. The former theory computes the lift and drag forces locally on the blades, while the latter one describes the momentum loss of the airflow through the rotor plane and the calculation of the induction factor. As the wind interacts with the blades of a turbine, it gives energy to the system, resulting in a decrease in its velocity. The induction factor (α_{ind}) (Equation 3.4), expresses the relationship between the wind velocity far from the rotor (U) and on the rotor (U_r) [71].

$$a_{\text{ind}} = \frac{U - U_r}{U} \tag{3.4}$$

As described in the blade element theory, the lift and drag forces are calculated from Equation 3.5a and Equation 3.5b, respectively, where C_l is the lift coefficient, C_d is the drag coefficient. ρ_{air} is the air density, c is the chord length and dr is the distance of the blade element from the blade root. These magnitudes are also illustrated in Figure 3.4, where R is the resultant force, ϕ is the inflow angle, θ is the section pitch angle, α the angle of attack, Ω the rotational speed of the rotor and V_{res} is the sum of the wind velocity and the one coming from the rotation of the blade. More information about the derivation of these equations or the definition of the rest of the magnitudes can be found in the book of Zaiijer and Viré [71].

$$dL = \frac{1}{2} \cdot C_l \cdot \rho_{\text{air}} \cdot V_{\text{res}}^2 \cdot c \cdot dr \tag{3.5a}$$

$$dD = \frac{1}{2} \cdot C_d \cdot \rho_{\text{air}} \cdot V_{\text{res}}^2 \cdot c \cdot dr \tag{3.5b}$$

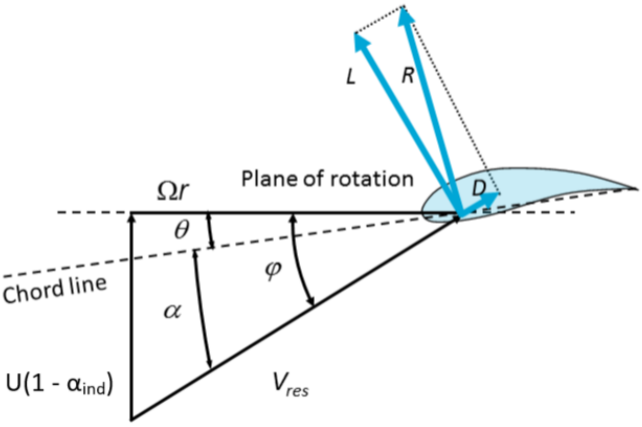

Figure 3.4: Lift and Drag on a blade element [71]

The latter component of BEM, momentum theory, explains how the interaction of airflow with the rotor disk leads to pressure and momentum losses across the rotor plane. The thrust force extracted from each rotor annulus dr is given by Equation 3.6.

$$dT = 4 \cdot \pi \cdot r \cdot \rho_{\text{air}} \cdot V^2 \cdot (1 - \alpha_{\text{ind}}) \cdot \alpha_{\text{ind}} \cdot dr \tag{3.6}$$

Figure 3.5 illustrates the main aerodynamic parameters within BEM theory, where F_t and F_n are the tangential and normal component of the force on the plane of rotation, respectively.

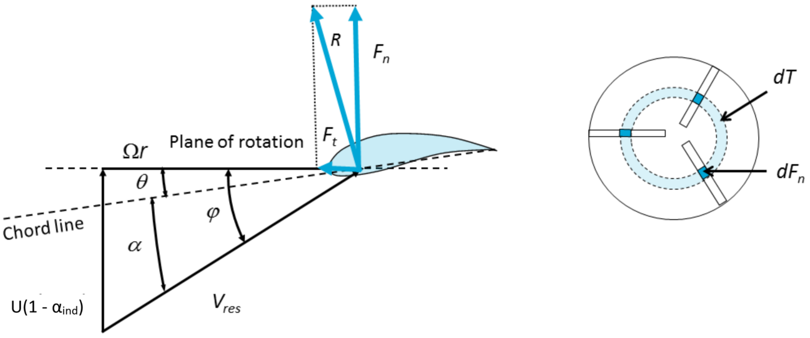

Figure 3.5: Main aerodynamic parameters on an airfoil (left) and BEM principle configuration (right) [71]

F_n for each rotor annulus is calculated from Equation 3.7, while it can also give the rotor thrust from Equation 3.8, where B is the number of the rotor blades.

$$dF_n = dL \cdot \cos\varphi + dD \cdot \sin\varphi = \frac{1}{2} \cdot \rho_{\text{air}} \cdot V_{\text{res}}^2 \cdot (C_l \cdot \cos\varphi + C_d \cdot \sin\varphi) \cdot c \cdot dr \tag{3.7}$$

$$dT = B \cdot dF_n \tag{3.8}$$

3.4. Wave Theory

3.4.1. Wave Physics

Beyond aerodynamic loads, offshore wind turbines and especially semi-submersible FOWTs, are subjected to wave loads that induce platform motions. Therefore, it is significant to discuss the wave and hydrodynamic behavior.

Ocean waves are created from the interaction between the wind and the sea and they can be characterized by physical properties, such as the water depth d, the wavelength λ and the wave height h. Another important property is the wave steepness defined as h/λ, which divides the waves into deep water waves (when the wave steepness is higher than 1/2), shallow water waves (when the ratio is lower than 1/20) and intermediate waves (when the ratio is between 1/20 and 1/2) [85].

Another substantial separation between the waves is the division into regular and irregular waves. Regular (deterministic) or harmonic waves are represented by simple sinusoidal functions with a constant wave direction, height, and period. This shape is characterized by a crest, the highest point of the wave, and a trough, the lowest point. The distance between two consecutive crests is the wavelength λ, the wave height h is the vertical distance between a crest and a trough and the period of the wave T is the time period between two successive upward zero-crossings. The features of a regular wave are depicted in Figure 3.6, where ζ_α is the amplitude of wave elevation, which is defined as the distance of the crest from the still water level [86].

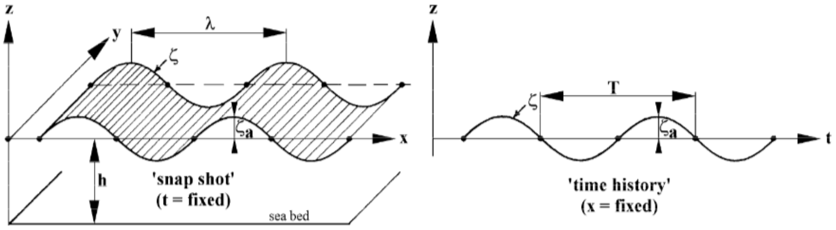

Figure 3.6: Regular wave definition [86]

In reality, wave patterns are not repetitive and constant, but stochastic and irregular, with the elevation of the water surface resembling the one depicted in Figure 3.7, rather than following an ideal sinusoidal form. The sea evolves perpetually over time and the wavelength between two subsequent crests constantly changes. This irregularity renders irregular waves quite valuable for simulation of realistic conditions. Figure 3.7 portrays the irregularity of a irregular wave amplitude on the left and the superposition of many regular waves to form an irregular one on the right. The basic parameters describing irregular waves are the significant wave height H_s and the peak period T_p, which are defined as inputs in the HydroDyn module. H_s is defined as the average height of the highest 1/3 of the waves in the examined period and peak period is defined as the period during which the most energetic waves of the total wave spectrum occur. More information on the wave modeling and definition can be found in the work of Journée and Massie [86], but are out of the scope of this thesis.

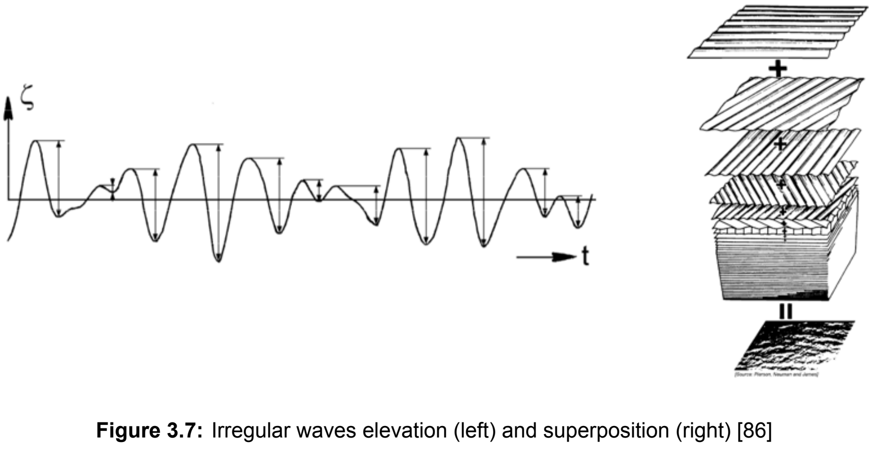

Figure 3.7: Irregular waves elevation (left) and superposition (right) [86]

In HydroDyn module, both regular and irregular waves can be modeled, long-crested (unidirectional) or short-crested (with wave energy across a range of directions). As it was already mentioned, irregular waves are preferred to simulate realistic wave conditions, thus, irregular waves are considered in this project, where multimple regular waves are superpositioned. Their wave energy can be described by appropriate wave spectra such as the JONSWAP and Pierson-Moskowitz spectrum, which both can be modeled in HydroDyn. For the scope of this project, the Pierson-Moskowitz spectrum has been selected (or JONSWAP with peak shape parameter equal to one) as an approximation for a common offshore location between the BOWT and FOWT, where fully developed sea-state is assumed. Furthermore, for this project, no second-order wave kinematic phenomena are considered [73], since their simulation requires significantly more computational time, while it produces almost the same results. Also, for this thesis, current loads are not considered as it will be elaborated in the load cases selection included in Section 4.3. The selected wave spectrum S_J is represented by Equation 3.9, where H_s is the significant wave height and T_p is the wave peak spectral period. The values of the simulated pairs H_s and T_p are explained in detail in Chapter 4.

$$S_J(\omega) = \frac{5}{32\pi} \cdot H_s^2 \cdot T_p \left(\frac{\omega T_p}{2\pi}\right)^{-5} \cdot \exp\left[-\frac{5}{4}\left(\frac{\omega T_p}{2\pi}\right)^{-4}\right] \tag{3.9}$$

3.4.2. Hydrodynamic Loading and Motion Response

The various types of waves and the motion of the water generate several forces on a floating structure. Regarding BOWTs, they are subjected to hydrodynamic forces, such as buoyancy, but since they are constrained at the seabed, their DOFs are limited compared to FOWTs. In the case of FOWTs, wave-induced loads move the platform, which floats freely having six motion DOFs in total, three translational and three rotational split into pairs per axis, as illustrated in Figure 3.8 provided by Tran and Kim [87]. These DOFs are as follows:

- Surge and Roll for the x axis
- Sway and Pitch for the y axis
- Heave and Yaw for the z axis

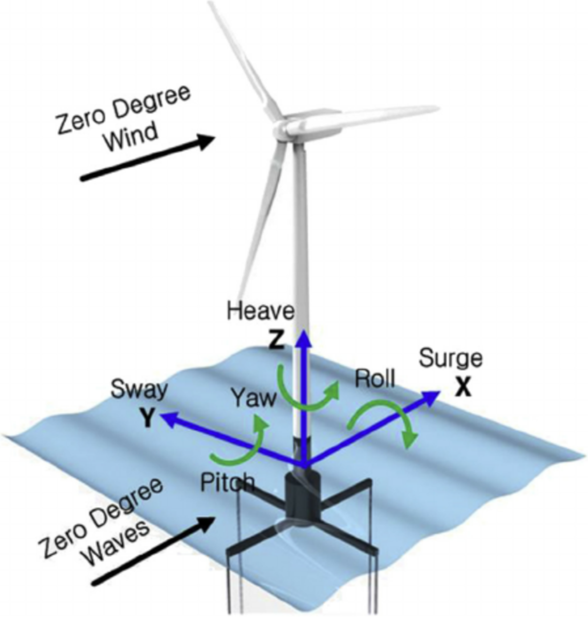

Figure 3.8: Platform motion DOFs of a FOWT [87]

The system motion response of the FOWT in OpenFAST is analyzed by rigid body dynamics, where the movement of the joint bodies is investigated under an external force action [88]. Therefore, to calculate the motion response of the platform, Equation 3.10 can be used based on Newton's second law of motion, resembling the platform-mooring lines-wind turbine system as a spring-mass-damper system [89, 90]. $\vec{x}(t)$ is the platform motion vector containing the six aforementioned DOFs, which is time-dependent (t). Furthermore, K is the stiffness matrix, C is the hydrodynamic damping matrix, M is the mass matrix of the platform and AM is the added mass matrix. Regarding the last parameter, in semi-submersible FOWTs, to ensure the stabilization of the system and mitigation of the load impacts, except for the active pitch control system, which is also used for the BOWTs and the onshore WTs, the ballast water distribution control strategy is implemented. In this control technique, ballast tanks are placed within the floating platform and by adjusting the distribution and volume of the water of the tanks, the center of gravity is shifted and the buoyancy is adjusted [91]. However, in OpenFAST, the dynamic ballast water distribution and shift of the platform center of gravity are not actively simulated, but the platform mass and added mass are modeled as static parameters.

$$(M + AM) \cdot \ddot{\vec{x}}(t) + C \cdot \dot{\vec{x}}(t) + K \cdot \vec{x}(t) = \vec{F}_{\text{ext}}(t) \tag{3.10}$$

F_{ext} vector denotes the external loads acting on the FOWT and can be divided into wind loads F_{wind}, mooring line restoration loads F_{moor}, hydrostatic forces F_{HS} and hydrodynamic loads F_{HD}, as showcased in Equation 3.11.

$$F_{\text{ext}} = F_{\text{wind}} + F_{\text{moor}} + F_{\text{HS}} + F_{\text{HD}} \tag{3.11}$$

The first term represents the wind loads, which can be distinguished between the thrust force T applied on the rotor and the drag force of the tower F_{tower} (applicable in both BOWTs and FOWTs). Since the scope of this section is to give a brief overview of the theory used in the OpenFAST, additional information on the definition of these loads is provided in the thesis of Filippidis [88] and the work of Lerch et al. [90].

The motion of the platform is limited by the mooring lines. The mooring forces counteract the incoming wind and wave loads, to stabilize the platform. Their modeling in MoorDyn module serves this rationale. Considering that K_{moor} is the restoring stiffness matrix of all mooring lines, the mooring forces are calculated from Equation 3.12.

$$F_{\text{moor}} = -K_{\text{moor}} \cdot x \tag{3.12}$$

The hydrostatic forces arise from submerging a structure into the water and consist of buoyancy and gravitational force that oppose each other, as shown in Equation 3.13, where ρ_w denotes the density of the water, V_{sub} the displaced water volume and K_{HS} the linear hydrostatic-restoring matrix from the water-plane area and the center of buoyancy [73].

$$F_{\text{HS}} = \rho_w \cdot g \cdot V_{\text{sub}} - K_{\text{HS}} \cdot x \tag{3.13}$$

The last term of Equation 3.11 stands for the hydrodynamic loads which are calculated from Morison equation (Equation 3.14) for both BOWTs and FOWTs, where d is the water depth and u is the transverse component of the velocity. The first term expresses the inertia term, so C_m is the inertia coefficient, while the second term is the drag term, thus, C_D is the drag coefficient. The inertia term includes the Froude-Krylov force, which is caused by the pressure field around the body, and the added mass force. Consequently, considering a coefficient C_α for the added mass and 1 for the Froude-Krylov force, the inertia coefficient is equal to their sum, C_m = 1 + C_a.

$$F_{\text{HD}} = \rho_w \cdot C_m \cdot \frac{\pi \cdot d^2}{4} \cdot \dot{u}(t) + \frac{1}{2} \cdot \rho_w \cdot C_D \cdot d \cdot u(t) \cdot |u(t)| \tag{3.14}$$

For the BOWT, the Morison equation is used to calculate the hydrodynamic loads of the monopile substructure. On the contrary, for the FOWT, the potential flow theory is used [73], including however only the first order terms, specifically hydrostatic restoring forces, added mass, radiation damping and wave excitation forces. The second-order terms are omitted due to time constraints and the inability to access the license-locked commercial software WAMIT [92], which is used to compute that wave-structure interaction [73, 88].

3.5. Controller Operation

Wind turbines have four regimes, but they operate and generate power in two of them, in the below-rated operating region (or between the cut-in wind speed and the rated wind speed) and the above-rated operating region (or between the rated wind speed and the cut-out wind speed). In the below-rated region the blade pitch is constant, and the power is maximized by adjusting the generator torque. In the above-rated region, the blade is progressively pitched towards feather to reduce the aerodynamic power so that the rotor speed and generator power remain constant. Figure 3.9 depicts the operating regions for pitch-regulated (variable pitch) and stall-regulated (fixed pitch) WTs.

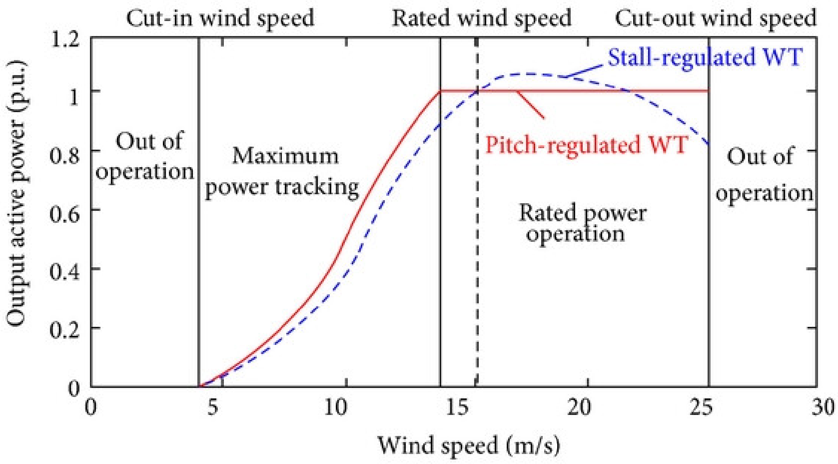

Figure 3.9: Example of power curves for pitch-regulated and stall-regulated wind turbines [93]

In the below-rated region, the generator torque control is implemented, which is cited in Equation 3.15. T_{HSS} is the torque of the HSS (or generator torque), ω_{HSS} is the HSS speed or generator speed which is linked to the rotor or LSS speed, Ω_{LSS} through Equation 3.16, where r_{gearbox} is the gearbox ratio. Finally, K_{opt} is the optimal load gain, given by Equation 3.17, where ρ_{air} is the air density and $C_{p,\text{max}}$ is the maximum power coefficient which is obtained for the optimal or design Tip Speed Ratio (TSR) (λ_{design}).

$$T_{\text{HSS}} = K_{opt} \cdot \omega_{HSS}^2 \tag{3.15}$$

$$\omega_{HSS} = r_{\text{gearbox}} \cdot \Omega_{LSS} \tag{3.16}$$

$$K_{\text{opt}} = \frac{\frac{1}{2}\rho_{\text{air}} C_{p,\text{max}} \eta_{\text{gearbox}} \pi R^5}{r_{\text{gearbox}}^3 \lambda_{\text{design}}^3} \tag{3.17}$$

In the case of FOWTs, the nacelle and the rotor also move due to the platform motions. This additional motion adds extra velocity to the rotor blades, making control more challenging. Traditional pitch controllers, commonly used in BOWTs, are slower and may not always be able to compensate for this additional effect.

In the context of OpenFAST, the Reference Open-Source Controller (ROSCO) is used, which is a WT controller designed for offshore wind turbines and developed by NREL [94]. ROSCO is an open-source controller available for FOWTs and it can be implemented in OpenFAST through an input file for ServoDyn module, to control key operations such as power optimization and rotor speed regulation. In this thesis, specifically, in the below-rated region, the control aims to optimize the rotor efficiency and subsequently power. In the above-rated region, the generator torque controller works in conjunction with the pitch controller, so that the produced power remains stable.

Following the description of OpenFAST operations and the main underlying wind, wave and controller theory, the next section focuses on the post-processing analysis of the OpenFAST outputs.

3.6. Post-Processing

This section explains in detail the post-processing of the OpenFAST outputs, to estimate the fatigue damage and the RUL of the main bearings by the procedure shown in Figure 3.1. This thesis uses the DTU 10 MW RWT, which is described in detail in Section 4.1. DTU 10 MW RWT has a four-point support drivetrain, which includes two MBs on the main shaft, specifically, two tapered roller bearings (TRBs). Wang et al. [64] modeled the DTU 10 MW RWT drivetrain in SIMPACK [60], considering both MBs locating, which means that they support both axial and radial loads, and their movement is constrained in the axial direction. The DTU 10 MW RWT drivetrain is also presented in detail in Section 4.1.

3.6.1. Calculation of equivalent dynamic load P

The equivalent dynamic load on the main bearings, mentioned in Subsection 2.6.3, is given by ISO 281: 2007 [68]:

$$P = XF_r + YF_\alpha \tag{3.18}$$

where F_r and F_α are the radial and axial loads on the bearing respectively, X is the dynamic radial load factor and Y the dynamic axial load factor of the bearings. X and Y are provided by the bearing manufacturer or estimated by ISO 281: 2007 [68], based on the bearing nominal contact angle. Krathe et al. [63] developed a medium-fidelity DTU 10 MW RWT drivetrain model in OpenFAST, in which they modeled the two MBs using constant stiffness springs between joints. They also studied the fatigue of the main bearings and according to them, the factors X and Y, are given in Table 3.2. C_D is the basic dynamic load rating and e is a threshold value to compare the axial to radial load ratio. Both of these quantities are given by the bearing manufacturer. According to Wang et al. (2019) [64], the upwind main bearing (MB1) is a TRB Koyo 2TR1450, while the downwind main bearing (MB2) is a TRB Koyo 2TR950B. Hence, from the manufacturer data [95], for the former, C_D is 9,690 kN and e is 0.61, while for the latter, C_D is 7,860 kN and e is 0.73, as shown in the table. Then, to define X and Y, the ratio of F_α and F_r should be compared with e for every simulated case. Depending on whether the axial to radial load ratio is higher or lower than e, the corresponding set of X and Y values is used.

Bearing location	C_D (kN)	e (-)	X (-)	Y (-)	**Load ratio**
Upwind	9690	0.61	1	1.11	$\frac{F_a}{F_r} \leq e$
Main bearing			0.67	1.66	$\frac{F_a}{F_r} > e$
Downwind	7860	0.73	1	0.92	$\frac{F_a}{F_r} \leq e$
Main bearing			0.67	1.37	$\frac{F_a}{F_r} > e$

Table 3.2: Main bearing load parameters

It is important to define the axial and radial forces acting on the main bearings. According to [63], the radial load on the main bearings is composed of the transverse (F_y) and vertical (F_z) loads on the main bearings.

$$F_r = \sqrt{F_y^2 + F_z^2} \tag{3.19}$$

To define the reaction forces of the main bearings in the y- and z-direction, the analytical formulation presented by Hart et al. [65] is used. A verification of this analytical formulation is presented here performing moment and force balances in a four-point suspension drivetrain in static equilibrium, assuming that the drivetrain is rigid and the hub forces and moments are known. A general representation of the main bearings modeled is shown in Figure 3.10. F_h and M_h refer to the forces and moments applied on the hub of the wind turbine, while F_1 and F_2 pertain to the reaction forces of the upwind and downwind main bearings, respectively. All of the aforementioned forces and moments can be analyzed in their components in the x, y and z axis. The two main bearings have a spacing of $2L_b$, and L_h is the distance of the hub from the midpoint of the spacing of the two main bearings. According to Wang et al. [64], for the DTU 10 MW RWT drivetrain, L_b is equal to 0.764 m, while L_h is equal to 3.734 m.

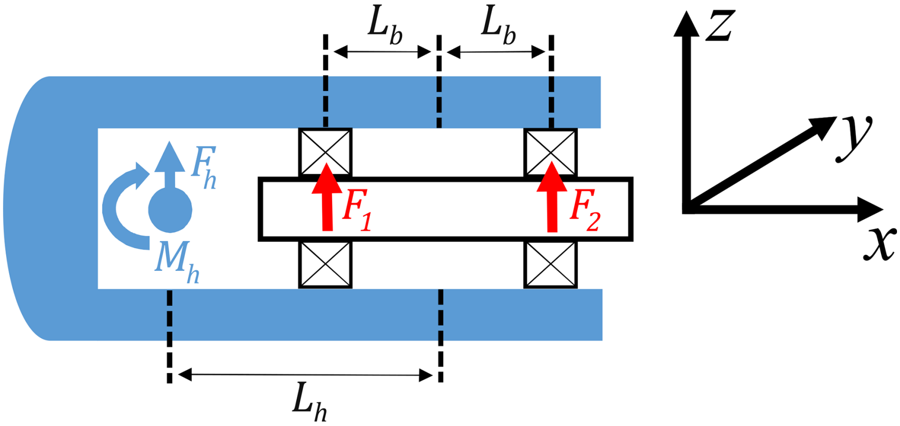

Figure 3.10: A general representation of the main bearings modeled by [65]

The force equilibrium on the y-axis and z-axis are given by:

$$F_1^y + F_2^y + F_h^y = 0 \Rightarrow F_2^y = -F_1^y - F_h^y \tag{3.20}$$

$$F_1^z + F_2^z + F_h^z = 0 \Rightarrow F_2^z = -F_1^z - F_h^z \tag{3.21}$$

Next, the equilibrium of moments about the y-axis at the midpoint of the spacing between the two main bearings is considered (corresponding to the initial moment equilibrium expression in Equation 3.22). According to the right hand-thumb rule and the standard sign convention, F_1^z and F_h^z create a positive moment (counter clockwise - CCW), while F_2^z creates a negative moment (clockwise - CW). Moreover, as it has also been mentioned in other studies, such as [65, 96, 97], it is assumed that the moments acting on the main bearings have a small contribution compared to the forces, thus they are neglected. Therefore, after substituting Equation 3.21, the moment equilibrium around y-axis, given in Equation 3.22, yields F_1^z.

$$M_h^y + F_1^z \cdot L_b + F_h^z \cdot L_h - F_2^z \cdot L_b = 0 \Rightarrow M_h^y + 2F_1^z \cdot L_b + F_h^z \cdot (L_b + L_h) = 0$$
$$\Rightarrow \quad F_1^z = -\frac{1}{2}\left(F_h^z \cdot \left(1 + \frac{L_h}{L_b}\right) + \frac{M_h^y}{L_b}\right) \tag{3.22}$$

Then, after substituting F_1^z into Equation 3.21, the vertical reaction force at the downwind main bearing F_2^z is given by:

$$F_2^z = -\frac{1}{2}(F_h^z \cdot (1 - \frac{L_h}{L_b}) - \frac{M_h^y}{L_b}) \tag{3.23}$$

Finally, akin to the aforementioned derivation, regarding the equilibrium of moments about z-axis at the midpoint, F_1^y and F_h^y create a negative (CW) moment, while F_2^y gives a positive (CCW) moment. Considering, also Equation 3.20, F_1^y and F_2^y are calculated as follows:

$$\begin{aligned} M_h^z - F_1^y \cdot L_b - F_h^y \cdot L_h + F_2^y \cdot L_b = 0 \Rightarrow M_h^z - 2F_1^y \cdot L_b - F_h^y \cdot (L_b + L_h) = 0 \\ \Rightarrow \quad F_1^y = -\frac{1}{2}(F_y^h \cdot (1 + \frac{L_h}{L_b}) - \frac{M_h^z}{L_b}) \end{aligned} \tag{3.24}$$

$$F_2^y = -\frac{1}{2}(F_y^h \cdot (1 - \frac{L_h}{L_b}) + \frac{M_h^z}{L_b}) \tag{3.25}$$

The reaction forces for each main bearing are calculated with respect to the local coordinate system of the main bearings or shaft, which is identical to the non-rotating shaft coordinate system that is used in OpenFAST and illustrated in Figure 3.11 (for a downwind wind turbine). Therefore, although the shaft is tilted with respect to the y-axis of the global coordinate system, the tilt angle is not mentioned in any of the equations.

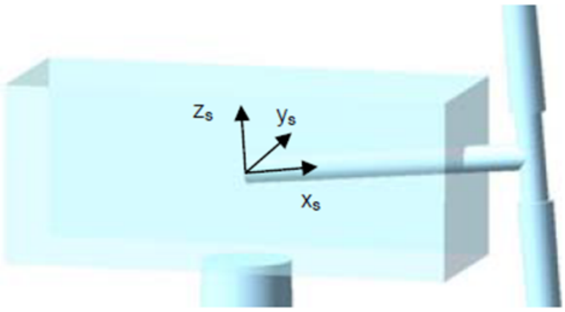

Figure 3.11: Shaft coordinate system in OpenFAST [74]

The moments and forces at the hub, denoted by subscript h in the study of Hart et al. [65], can be derived from the OpenFAST simulations as outputs of the ElastoDyn module. Specifically, the specific used outputs are listed below, considering that the OpenFAST outputs are the forces and moments at the interface between the hub and the main shaft, already including the aerodynamic and gravitational loads and their effects [74]:

- F_h^y : LSShftFys, Non-rotating LSS shear force along y_s-axis and constant along the shaft
- F_h^z : LSShftFzs, Non-rotating LSS shear force along z_s-axis and constant along the shaft
- M_h^y : LSSTipMys, Non-rotating LSS bending moment at the shaft tip about the y_s-axis
- M_h^z : LSSTipMzs, Non-rotating LSS bending moment at the shaft tip about the z_s-axis
- F_h^x : LSShftFxa, LSS thrust force (constant along the shaft and equivalent to the rotor thrust force)
- M_h^x : LSShfttq, LSS torque, (constant along the shaft and equivalent to the rotor torque)

Regarding the reaction forces of the main bearings in the x-direction, Hart et al (2022) [65] considered that only one of the two main bearings supports axial loads, the locating bearing, while the non-locating bearing does not handle any axial loads. However, for the DTU 10 MW RWT drivetrain studied in this thesis project, both main bearings are considered locating, so the axial hub load (or the thrust force of the rotor) should be distributed along the two main bearings.

To achieve this, it is assumed that the hub load in the axial direction is shared between the two main bearings, proportionally to their stiffness, emulating the linear behavior of spring elements, as has been mentioned in relevant references [98, 99]. More precisely, Harris and Kozalas [98] mentioned that if two bearings have axial constraints and support a common axial force, the force is distributed in proportion to their axial stiffnesses, thus the stiffer main bearing will handle a higher share of the axial load. This approach comes with some limitations and approximations that can be summarized below:

- There are not any considerable moments about the x-axis and the rotor thrust is the dominant force in the x-direction
- There is not any axial displacement (thanks to locating bearings), minimal shaft deformation, while the rotor and the hub are considered as rigid bodies.
- Despite the fact that platform motions are present in the FOWT, considering the sufficiently small timestep of 0.025 s of the simulations (as presented in Section 4.3) and the aerodynamic and hydrodynamic coupling through OpenFAST, it can be assumed that the rotor thrust already includes the effects of turbulent conditions and platform motions.

Consequently, this method offers a reasonable alternative for the comparative evaluation of the fatigue and loads of BOWTs and FOWTs in this thesis. Then, from the force equilibrium in the x-direction which is shown in Equation 3.26 and the axial stiffnesses of the two main bearings, the axial reaction forces of the two main bearings can be defined. In Equation 3.27, F_{total}^{x} is the total axial force that needs to be handled by the two main bearings. According to Krathe et al. (2025) [63], who simulated and modeled the DTU 10 MW RWT drivetrain, the axial stiffness of the upwind main bearing K_{x1} is equal to $3.53 \cdot 10^9$ N/m, while the counterpart K_{x2} for the downwind main bearing is equal to $3.39 \cdot 10^9$ N/m.

$$F_1^x + F_2^x + F_h^x = 0 \tag{3.26}$$

$$F_1^x + F_2^x = -F_h^x = F_{total}^x \tag{3.27}$$

$$F_1^x = \frac{K_{x1}}{K_{x1} + K_{x2}} \cdot F_{total}^x \tag{3.28}$$

$$F_2^x = F_{total}^x - F_1^x \tag{3.29}$$

Therefore, according to the aforementioned equations, the axial F_α and radial load F_r of the two main bearings are given from the following equations, where the subscript “1” refers to the upwind main bearing and “2” to the downwind main bearing:

$$F_{\alpha,1} = F_1^x \tag{3.30}$$

$$F_{r,1} = \sqrt{(F_1^y)^2 + (F_1^z)^2} \tag{3.31}$$

$$F_{\alpha,2} = F_2^x \tag{3.32}$$

$$F_{r,2} = \sqrt{(F_2^y)^2 + (F_2^z)^2} \tag{3.33}$$

3.6.2. Load Duration Distribution (LDD) method

Following the calculation of axial and radial loads of the main bearings and subsequently, of the equivalent dynamic load for each timestep from Equation 3.18, the next step is to implement the LDD method.

In the LDD method, the rotational speed of the rotor (n_{rotor}) in rpm, and subsequently that of the main shaft which is an output of OpenFAST, is used. In this thesis, simulations of 4000 s are performed with an analysis timestep of 0.025. The selection of these numbers is clearly explained in Section 4.3. After discarding the initial 400 s of the OpenFAST simulation, to remove transient effects, the remaining simulation time amounts to 3600 s with output data exported at a timestep of 0.025 s. This results in a total of 144,000 data points for every quantity.

Next, the revolutions or cycles per timestep, $\text{cycles}_{\text{timestep}}$, and hour, $\text{cycles}_{\text{hourly}}$, are calculated by:

$$\text{cycles}_{\text{timestep}} = \frac{n_{\text{rotor}}}{60} \, dt \tag{3.34}$$

$$\text{cycles}_{\text{hourly}} = \sum_{t=0}^{3600\text{s}} \text{cycles}_{\text{timestep}} \tag{3.35}$$

where dt = 0.025 s, n_{rotor} is the rotor rotational speed in rpm and $\text{cycles}_{\text{hourly}}$ is the summation of the $\text{cycles}_{\text{timestep}}$ in the hourly simulation. Subsequently, a histogram is constructed to determine the duration for which specific load magnitudes occur at each wind speed interval. To decide on the number of bins to be used for the histogram, a short sensitivity analysis is performed. Specifically, the LDD script has been run multiple times for the FOWT for a specific operating condition at 11.5 m/s, using various numbers of bins, and the arising damage of MB1 over 20 years only from the contribution of this wind speed has been compared. In Figure 3.12, the LDD histogram is shown for four numbers of bins in total. On the x-axis, the P load values of the different bins are written, while on the y-axis, the cycles per hour for every bin are mentioned.

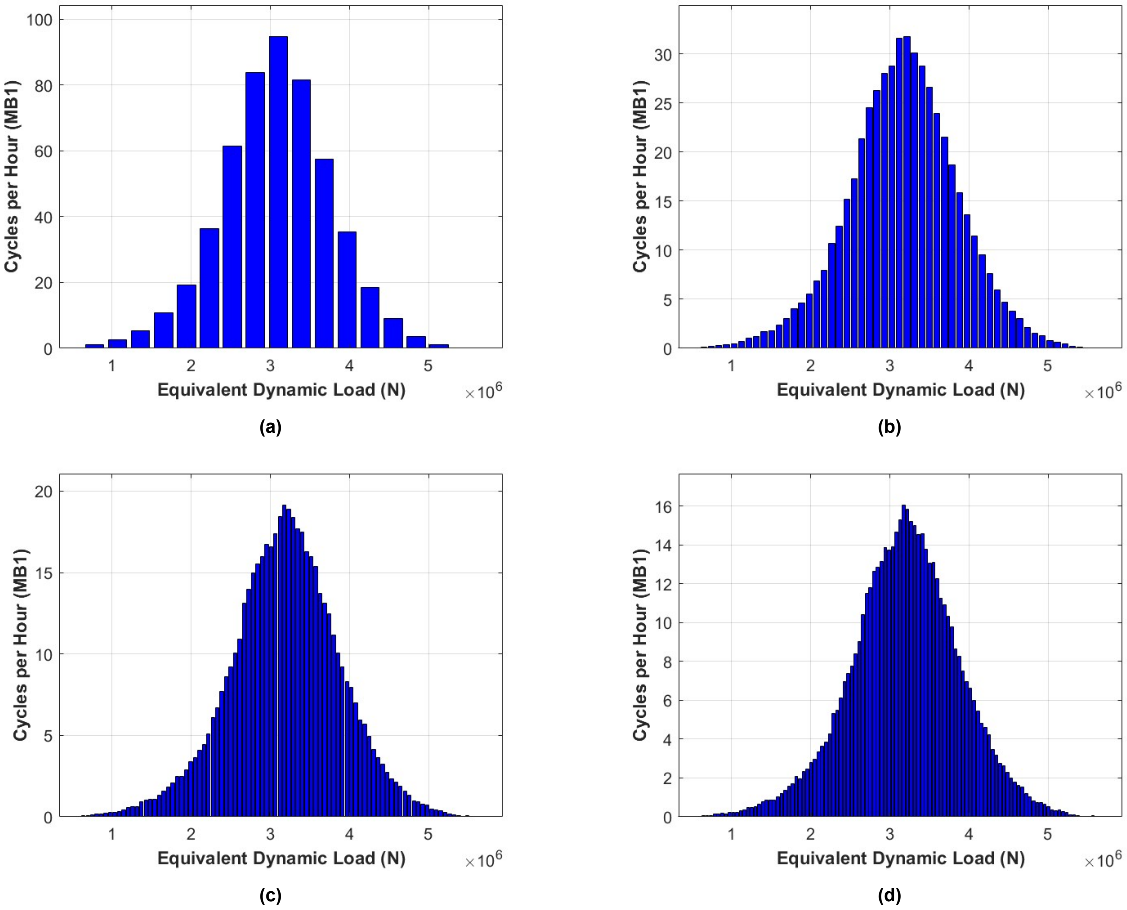

Figure 3.12: LDD histograms for four bins number: (a) 20, (b) 60 (c) 100 and (d) 120

In Figure 3.13, the 20-year damage of MB1 for the FOWT and 11.5 m/s is depicted as a function of the used number of bins.

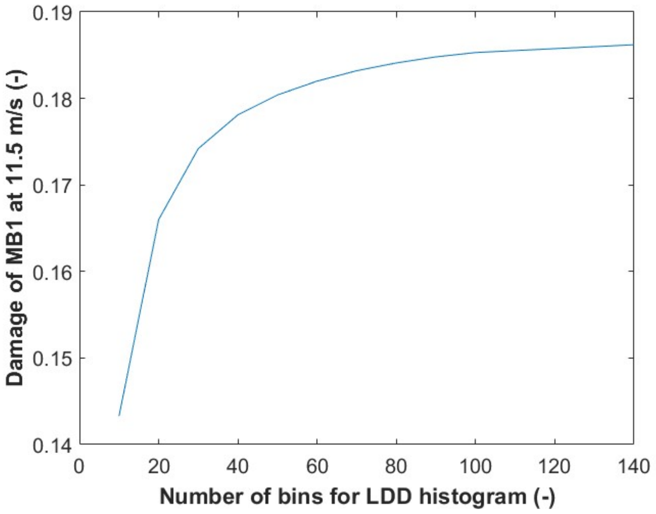

Figure 3.13: Number of bins plotted against the 20-year damage of MB1 for FOWT at 11.5 m/s

According to Figure 3.13, for more than 60 bins, the damage value changes less than 1%, thus, this number of bins is considered for the calculations. The LDD process is iterated for each load case separately. The various load cases are cited in Section 4.3.

Therefore, the values of equivalent dynamic loads P are divided into 60 bins and the number of incidences falling into each bin are defined as $counts_i$. Then, to find the number of cycles per bin and per hour, the P load duration of every bin is divided by the total number of seconds in one hour, T_{total} = 3600 s, and multiplied by the hourly cycles.

$$\text{cycles}_{\text{bin}} = \frac{counts_i \cdot dt}{T_{\text{total}}} \cdot \text{cycles}_{\text{hourly}} \tag{3.36}$$

3.6.3. Damage and RUL calculation

Following the LDD implementation, the division of P loads in bins and the calculation of cycles per bin, the bearing basic rating life in cycles for every bin is calculated as:

$$L_{10,i} = 10^6 \cdot \left(\frac{C_D}{P_i}\right)^m \tag{3.37}$$

where, according to ISO 281:2007 [68], m = 10/3 for roller bearings. To assess the fatigue damage of the main bearings, the Palmgren-Miner linear damage accumulation rule is applied, including the Weibull probability for every wind speed. First, the Weibull probability for every wind speed U is given by

$$\text{prob}_{\text{Weibull}}(U) = \frac{k}{\alpha_{scale}} \cdot (\frac{U}{\alpha_{scale}})^{k-1} e^{-(\frac{U}{\alpha_{scale}})^k} \tag{3.38}$$

where α_{scale} is the scale parameter and k is the shape parameter of the Weibull distribution for a specific site. With the wind speed distribution defined, the hourly damage for every wind speed can be calculated by summing the damage contributions of each bin of the LDD histogram [64]. The contribution of each bin is weighted by the Weibull probability for the relevant wind speed, as shown in:

$$D_{\text{hourly}} = \sum_{i=1}^{60} \left(\frac{\text{cycles}_{\text{bin},i}}{L_{10,i}}\right) \cdot \text{prob}_{\text{Weibull}}(U) \tag{3.39}$$

where $cycles_{bin,i}$ is the hourly number of cycles per bin. To calculate the accumulated damage over the 20-year design lifetime of the WTs (assuming a 95% availability of the WT power production [64]), the hourly damage is calculated for every hour over the 20 years using the same Weibull probability distribution, and then linearly extrapolated to 20 years, following the approach adopted in previous studies [100, 101]. The aggregation is found as follows:

$$D_{\text{accumulated}} = D_{\text{accumulated},i} + D_{\text{hourly}} \tag{3.40}$$

where $D_{\text{accumulated},i}$ denotes the accumulated damage at every hour over the 20 years. Finally, the RUL of the main bearing over the 20-year period is found by

$$RUL(t) = (1 - D_{\text{accumulated}}(t)) \cdot t_{\text{life}} \tag{3.41}$$

where t is a specific moment in time and t_{life} = 20 years is the lifetime. When $D_{\text{accumulated}} = 1$, $RUL = 0$ and this means that the main bearing fails. The cumulative damage of all wind speeds yields the total RUL.

4

Case Study

This chapter presents a case study for the methodology described in Chapter 3, using the DTU 10 MW RWT in both bottom-fixed monopile and floating semi-submersible configurations. First, Section 4.1 presents the basic specifications of the DTU 10 MW RWT and its drivetrain, along with a brief description of the monopile BOWT and semi-submersible FOWT models. Second, Section 4.2 describes the site selection process and the necessary model adjustments to ensure a valid comparison of the two WT models under identical environmental conditions. Then, Section 4.3 analyzes the load case selection and the simulation setup, implementing the Design Load Case (DLC) 1.2 of IEC Standard 61400-1:2019 [84] with specific wind speeds and turbulence characteristics. Finally, Section 4.4 presents the metocean conditions, including significant wave height, peak spectral period, wind and wave directions, and wind speed probability for the selected North Sea location. Two wind-wave alignment scenarios are defined: realistic conditions with misaligned wind and wave directions, and idealized conditions with aligned wind-wave directions.

4.1. DTU 10 MW Reference Wind Turbine

As mentioned in Section 3.6, the DTU 10 MW RWT is used with its main characteristics shown in Table 4.1. The wind turbine has been designed for offshore sites with an IE) class 1A wind climate and is a conventional three-bladed, upwind wind turbine with a variable-speed collective pitch power control system [64].

Table 4.1: Main characteristics of the DTU 10 MW reference wind turbine [64]

Parameter	Value
Rated power (MW)	10
Cut in wind speed (m/s)	4
Rated wind speed (m/s)	11.4
Cut out wind speed (m/s)	25
Rotor diameter (m)	178.3
Hub height (m)	119.0
Hub diameter (m)	5.6
Drivetrain	medium-speed, multiple stage gearbox
Hub overhang (m)	7.1
Shaft tilt angle (deg)	5.0
Rotor mass (kg)	227,962
Nacelle mass (kg)	446,036
Tower mass (kg)	628,442

The main features of the drivetrain of the DTU 10 MW RWT are shown in Table 4.2 [64]. The DTU 10 MW RWT drivetrain is a four-point support system, including two TRBs, whose key features were described in Section 2.5. These two main bearings support the drivetrain to hinder vast non-torque loads from entering the gearbox. Wang et al. [64], in their study, modeled the DTU 10 MW wind turbine drivetrain in detail using the high-fidelity multibody simulation software SIMPACK [60], considering both main bearings as locating bearings. Also, the short distance between the two main bearings results in a shorter main shaft, thereby making the drivetrain more compact. This drivetrain model includes two planetary gear stages and one parallel gear stage, achieving an overall 1:50 gear ratio. The detailed schematic layout of the drivetrain designed for the DTU 10 MW RWT is shown in Figure 4.1.

Table 4.2: Drivetrain and torsional properties of the wind turbine [64]

Parameter	**Value**
Gearbox ratio	1:50
Minimum rotor speed (rpm)	6.0
Rated rotor speed (rpm)	9.6
Rated generator speed (rpm)	480.0
Electrical generator efficiency	94
Generator inertia about high-speed shaft (kgm^2)	1,500.5
Equivalent drive-shaft torsional-spring constant (Nm/rad)	2,317,025,352
Equivalent drive-shaft torsional-damping constant (Nm/(rad/s))	9,240,560

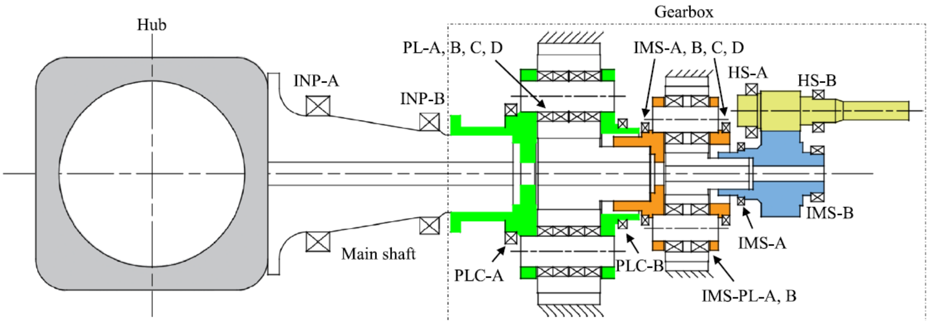

INP-A, B: Main shaft bearings.
PLC-A, B: Planet carrier bearing in the first stage; PL-A, B, C, D: Planet bearings in the first stage.
IMS-PLC-A, B: Planet carrier bearing in the second stage; IMS-PL-A, B: Planet bearings in the second stage.
IMS-A, B: Intermediate shaft bearings in the third stage; HS-A, B: High speed shaft bearings in the third stage.

Figure 4.1: 10 MW wind turbine drivetrain schematic layout [64]

For the purpose of this project, which is to study and compare the fatigue damage of the main bearings between a BOWT and a FOWT, two available models of a different substructure for DTU 10 MW RWT are used. More specifically, the monopile DTU 10 MW RWT, initially placed at 30 m water depth is used as a BOWT. As a FOWT, this thesis uses the Nautilus DTU 10 MW RWT, composed of the classic DTU 10 MW wind turbine placed on a semi-submersible floating platform, designed by Nautilus floating solutions, S.L, for the Gulf of Maine at 130 m water depth [102]. The designed semi-submersible platform consists of four columns, a rigid ring pontoon linking the columns to flat lower surfaces, while the main deck (10.5 m x 3 m) is composed of four rectangular shaped connections between the upper end of the columns (diameter = 10.5) and the transition piece. Regarding ballasting mechanisms, it includes a concrete and a seawater ballast system and the whole platform is connected to the seabed via four mooring lines alongside their anchors and fairleads. The components of the platform are shown in Figure 4.2 and the detailed design parameters can be found in the relevant work [102, 103].

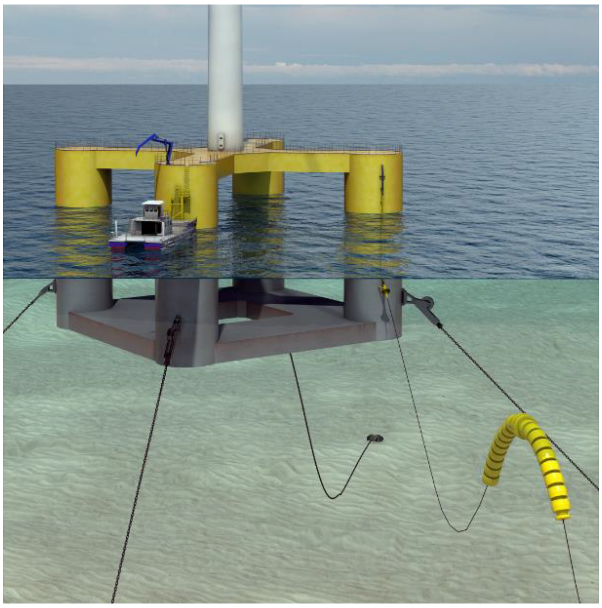

Figure 4.2: Nautilus DTU 10 MW WT semi-submersible platform [102]

Although the two WT configurations share the same main characteristics and the DTU 10 MW drivetrain properties (shown in Table 4.1 and Table 4.2 respectively), they slightly differ with respect to their tower characteristics. Specifically, both towers are 115.63 in height, but their stiffness and total mass are different. The FOWT tower is slightly heavier and stiffer than the BOWT tower, having a total mass of 879,381 kg compared to 640,940 kg of the BOWT tower, while the FOWT tower starts with a diameter of 10.5 m at the lowest part compared to the 9 m diameter of the monopile BOWT tower at the same point. Moreover, the tower of the FOWT is stiffer than that of the BOWT, as can be seen in Appendix Section A.1. In this way, the platform motions can be compensated and excessive tower-top displacements and resonance with the platform can be avoided, since the platform motion frequencies are generally lower.

4.2. Selected Location and models adjustment

Although FOWTs are typically installed in deeper waters than BOWTs, a common location was selected in this project to ensure a valid comparative analysis under identical metocean conditions for the main bearings of the two offshore WT configurations. Based on the applicable water depths of the two configurations and to be as close as possible to the realistic installation approaches, elaborated in Section 2.1, a 60 m water location was chosen in the North Sea, since that water depth can be considered as the point to shift from BOWTs to FOWTs considering their cost effectiveness [21]. Specifically, it is an offshore location off the coast of Peterhead, Scotland, with coordinates, $57.45°$N, $1.606°$W [104] (Figure 4.3). This location is close to the Buchan Deep Meteorological station used for the analysis of the metocean conditions in Hywind Scotland Floating Wind farm ($57.45°$N, $1.31°$W) [105] and other locations found in the literature that facilitate the specification of metocean conditions for the specific project.

Figure 4.3: Selected location for the study of the WTs ($57.45°$N, $1.31°$W, 60 m depth)

Subsequently, the BOWT and the FOWT should be set at the same 60 m water depth and the models in OpenFAST should be adjusted. This is done with estimations based on the relevant literature, which are briefly explained below. A detailed redesign and setting-up of the new models would require significant time, while it constitutes the explicit topic of other theses devoted to that.

Regarding the BOWT model, which involves a monopile substructure, the discretized members and member joints of the substructure are specified in the SubDyn to define the geometry, connection properties and finite-element model of the monopile, while the mass distribution is automatically calculated from the material properties and geometry. To move the model to 60 m water depth, the number of discretized members was kept the same, but the vertical coordinates of the joints were modified to account for the increased depth. These assumptions are supported by Velarde [106], who proves that at higher water depth and almost the same geometry, the dynamic behavior and natural frequencies and periods of the monopile substructure remain constant.

For the FOWT model, developed by Nautilus with a semi-submersible four-columns platform designed for 130 m water depth, the main adjustment (apart from shifting the z-coordinate in the MoorDyn) is to adapt the mooring system, so that the mooring lines are not overly slack, since the platform structure remains identical and only the water depth changes. Detailed parameters of the mooring system are provided in the work of Arias and Galvan [102] and Galvan et al. [103], and summarized in Appendix Section A.2. The final mooring system characteristics are selected to maintain similar fairlead tensions on the four mooring lines of the semi-submersible platform, while keeping the system stable. In this way, the dynamic behavior of the original 130 m design and the adjusted 60 m water depth model remain similar, as also indicated by Shi et al. [107], who show that the restoring forces and mooring line tensions remain similar with water depth. To achieve this purpose, the unstretched length of the mooring lines was reduced by approximately 5%.

To verify that the dynamic behavior of the adjusted and original BOWT and FOWT models remains consistent, free-decay tests were performed. The methodology and results of these tests are presented in Appendix Section A.3.

4.3. Load cases and Simulations setup

In wind turbine simulations, depending on the goal or the specific topic, various load cases (LCs) are simulated to represent realistic environmental conditions. Specifically, for fatigue analyses, operating conditions are the most important, as parked conditions of wind turbines have a negligible contribution to the fatigue life of bearings and drivetrain components in general [108, 109]. Moreover, the environmental conditions often used in the WTs, are gathered in the Design Load Cases (DLCs) defined in standard IEC 61400-1:2019 [84] and divided into the following eight categories:

1. Power production

2. Power production plus occurrence of fault
3. Start-up
4. Normal shutdown
5. Emergency stop
6. Parked
7. Parked and fault conditions
8. Transport, assembly, maintenance and repair

Among the scientific literature, related to the fatigue analysis and assessment DLC 1.2 is usually used [64, 110, 111], corresponding to fatigue analysis. Moreover, ultimate load analysis cases such as DLC 1.1 has been simulated in some studies [111, 112], while other researchers have considered discrete wind speeds below-rated region around rated and over-rated region [113, 108, 15].

For this thesis, to ensure the contribution of all operating conditions to the damage of the main bearings and the estimation of their RUL, DLC 1.2 is selected, according to standard IEC-61400-3-1:2019 [53]. DLC 1.2 is summarized in Table 4.3, where NTM is the Normal Turbulence Model, NSS is the Normal Sea State, MIS and MUL denote misalignment and multidirectional respectively, NWLR is the Normal Water Level Range, MSL is the Mean Still Level and F is fatigue.

DLC	Wind condition	Waves	Wind and wave directionality	Sea currents	Water level	Type of analysis
1.2	NTM $V_{\text{in}} < V_{\text{hub}} < V_{\text{out}}$	NSS Joint Prob. Distribution of H_s, T_p, U_{hub}	MIS, MUL	No currents	NWLR or $\geq$ MSL	F

Table 4.3: Offshore DLC 1.2 overview (IEC 61400-3-1, 2019) [53]

According to IEC 61400-3-1, 2019 [53], for DLC 1.2, six 10-min stochastic simulations or a continuous 1-hour simulation can be performed. In this thesis, continuous 1-hour period is considered for the simulations. To determine the simulation timestep, which defines how often the various simulation parameters are computed, NREL recommends that it is around or at maximum the one-tenth of the highest frequency simulated [59]. For this thesis, the highest frequency that could be of interest is the 3P which describes the phenomena that occur 3 times per revolution. For the DTU 10 MW RWT, whose maximum rotor speed is the rated one at 9.6 rpm, which corresponds to 0.16 Hz, the 3P frequency is 0.48 Hz. Therefore, the maximum recommended timestep is 0.208 s given by:

$$dt = \frac{1}{10 f_{\text{max}}} \tag{4.1}$$

where dt is the simulation timestep and f_{max} is the highest frequency of interest (0.48 Hz). A lower timestep was used, to ensure a more accurate simulation that captures even more frequent phenomena. In particular, for the FOWT model simulations, a timestep of 0.025 s was considered. For the BOWT, a finer timestep of 0.005 s was used due to convergence issues with SubDyn which typically requires smaller timesteps for numerical stability [59]. The timestep of the FOWT model remained at 0.025 s for computational efficiency, after verifying that there is no significant difference between the results (in terms of load statistics and fatigue) with a simulation timestep of 0.025 and of 0.005 s.

Furthermore, for the BOWT model, for a few exemplary cases, the results were exported in both 0.005 and 0.025 to evaluate any potential difference in the loads or the induced damage. The difference was negligible (less than 1%). Consequently, in both WT configurations, the results were exported in a timestep of 0.025 s and this is also the timestep of the analysis.

After defining the simulation timestep, simulations of 4000 s were performed and the first 400 s were discarded to remove any possible transient conditions, for the wind speeds within the operating range (4 - 25 m/s), split into 1 m/s clusters, thus the wind speeds considered in the simulations were 4.5 m/s, 5.5 m/s, 6.5 m/s and so on. In these LCs, NTM was considered in compliance with IEC 61400-1,2019 [84] for a Turbulence Class A, as defined by the DTU 10 MW RWT. In the NTM, the representative value for turbulence standard deviation, σ_1, is given by:

$$\sigma_1 = I_{\text{ref}}(0.75U_{\text{hub}} + b) \quad \text{with} \quad I_{\text{ref}} = 0.16 \quad b = 5.6\,\text{m/s} \tag{4.2}$$

where U_{hub} is the wind speed at hub height and I_{ref} is the reference turbulence intensity. In this project, turbulent inflow conditions are modeled using TurbSim, which was introduced in Subsection 3.3.1. To generate turbulent conditions in TurbSim, NTM is used with Kaimal Spectrum, analyzed in Equation 3.3 and turbulence class A. In Figure 4.4, an example of turbulent inflow conditions is shown with the wind speed variations around a mean wind speed of 12.5 m/s in a time period of 1000 s, while in Table 4.4, the characteristics of the TurbSim simulation are mentioned in brief. Figure 4.4 shows a signal without smoothing. This representation captures the stochastic nature and intensity of turbulence that affect drivetrain loads.

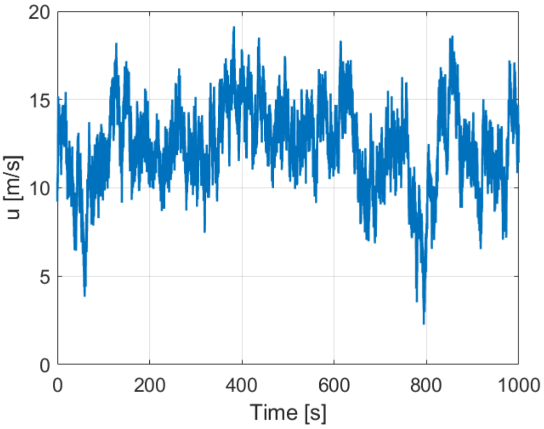

Figure 4.4: Example of turbulent inflow wind conditions of longitudinal direction component "u", generated through TurbSim, for mean wind speed 12.5 m/s

Table 4.4: TurbSim parameters for wind field generation

TurbSim Parameter	Value
Analysis Time [s]	4000
Time Step [s]	0.05
Grid Height [m]	230
Grid Width [m]	230
Grid points dimension [-]	20 × 20
Turbulence Model	Kaimal Wind Spectrum
IEC Turbulence Characteristic	A
IEC Turbulence Type	NTM
Wind Profile	Power Law
Power Law exponent	0.14
Surface Roughness Length [m]	0.003

4.4. Input metocean conditions

4.4.1. Significant Wave Height and Peak Spectral Period

Following the selection of wind speeds to be simulated for the various LCs, it is essential to define the significant wave height H_s and peak spectral period T_p, which are required inputs for each LC. Obtaining the metocean data for the selected location of 60 m water depth in the North Sea was not feasible through the literature or metocean databases. Therefore, data retrieved from literature studies in adjacent locations were adopted. Particularly, Li L. et al. [114] extracted joint probability distributions of wind and wave for five European Offshore sites, which have been circled in Figure 4.5.

Figure 4.5: Location of potential and examined European offshore sites [114]

Site 15., North Sea Center, whose coordinates are not precisely defined, refers to a location at 40 m water depth, 300 km from shore. According to the authors, in the North Sea, where site 15 and also the selected location (Section 4.2) are located, wind resources vary little from area to area and the waves are mainly wind-generated. Also, according to DNV standard DNV-RP-C205 [115], for water depths above 30 m and away from the coast, wave transformation effects are negligible, and wave parameters can be considered spatially homogeneous over short distances. Similarly, Holthuijsen [116] mentioned that in deep water or moderately deep water conditions, the wave field is mainly governed by wind field characteristics rather than local bathymetry. The values of H_s and T_p that were extracted from the joint probability distribution at site 15 for the desired wind speeds, almost correspond to deep waters (are in the verge between intermediate and deep waters) at 40 m water depths, so it is assumed that they can be adopted for the selected location at 60 m water depth, where the values correspond to clearly deep water conditions as defined in Subsection 3.4.1.

Regarding the methodology to define the H_s and T_p values, firstly, a conditional probability density function (PDF) of H_s as a function of wind speed U_{10} at 10 m height above the sea level, is given as a two-parameter Weibull distribution,

$$f_{H_s|U_w}(h \mid U_{10}) = \frac{\alpha_{HC}}{\beta_{HC}} \left(\frac{h}{\beta_{HC}}\right)^{\alpha_{HC}-1} \exp\left[-\left(\frac{h}{\beta_{HC}}\right)^{\alpha_{HC}}\right] \tag{4.3}$$

with the coefficients α_{HC} and β_{HC} defined as:

$$\alpha_{HC} = a_1 + a_2 U_{10}^{a_3} \tag{4.4}$$

$$\beta_{HC} = b_1 + b_2 U_{10}^{b_3} \tag{4.5}$$

The coefficients a_1, a_2 a_3, b_1, b_2 and b_3 are defined in [114], specifically for the location of Site 15. Moreover, to calculate the wind speed U_{10} at 10 m height, the inverse power law (presented in Subsection 3.3.1) was used, considering that the operating wind speeds included in DLC 1.2 are measured at hub height and the power law exponent is $\alpha_p = 0.14$.

$$U_{10} = \frac{U_{\text{hub}}}{\left(\frac{z_{\text{hub}}}{10}\right)^{\alpha_p}} \tag{4.6}$$

The expected value of H_s is found as the (expected) mean Weibull value calculated as:

$$E(H_s) = \beta_{HC}\,\Gamma\left(\frac{1}{\alpha_{HC}} + 1\right) \tag{4.7}$$

where Γ is the Gamma function [117]. Then, the mean peak spectral period T_p, is given as a joint function of wave height (h) and U_{10}, shown in Equation 4.8, including the two separate functions in Equation 4.9 and Equation 4.10.

$$\overline{T}_p(U_{10}, h) = \overline{T}_p(h) \cdot \left[1 + \theta\left(\frac{U_{10} - \overline{U_{10}}(h)}{\overline{U_{10}}(h)}\right)^{\gamma}\right] \tag{4.8}$$

$$\overline{T_p}(h) = e_1 + e_2 \cdot h^{e_3} \tag{4.9}$$

$$\overline{U_{10}}(h) = f_1 + f_2 \cdot h^{f_3} \tag{4.10}$$

The coefficients θ, γ, e_1, e_2, e_3, f_1, f_2 and f_3 are defined for the specific location in [114].

The H_s and T_p as a function of U_{10} are depicted in Figure 4.6 and Figure 4.7 respectively, while the overall wind speed, significant wave height and peak spectral period, considered for the different load cases are shown in the comprehensive Table 4.5, along with the wind and wave directions that are explained in Subsection 4.4.2. These conditions were introduced in the HydroDyn module.

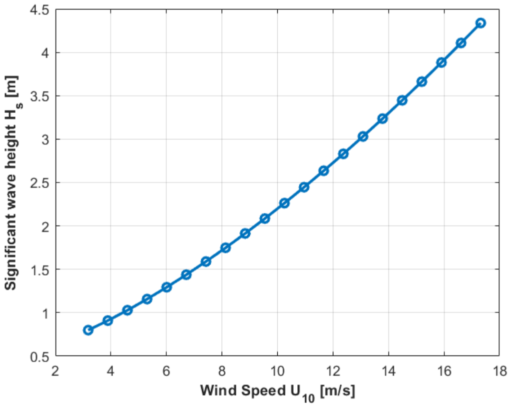

Figure 4.6: Expected significant wave height H_s as a function of wind speed U_{10}

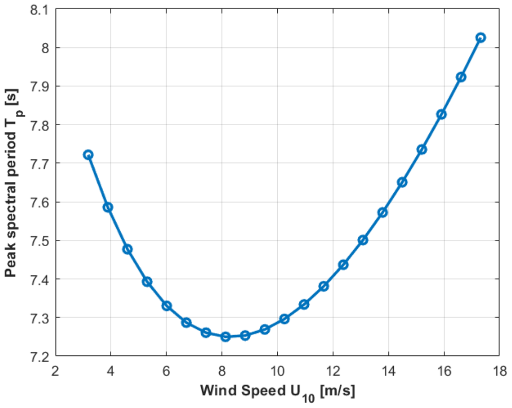

Figure 4.7: Expected peak spectral period T_p as a function of wind speed U_{10}

4.4.2. Wind and Wave directions

According to Standard IEC 61400-4: 2012 [53], the DLC 1.2 case contains misalignment and multidirectional wind and wave in their examined wind speeds. Therefore, regarding the desired load cases, to define the wind and wave direction of the simulations, the dominant wind and wave directions at the Buchan Deep ($57.45°$N, $1.31°$W) [118] have been adopted. This location, at 100 - 140 m water depth, was used for the metocean data site analysis of the Hywind Floating wind farm [105], which is located close to the location selected for the simulations of this thesis project $57.45°$N, $1.606°$W. The two locations, which are located at the same latitude, are shown in Figure 4.8, where the blue point corresponds to the selected location and the red point to the Buchan Deep.

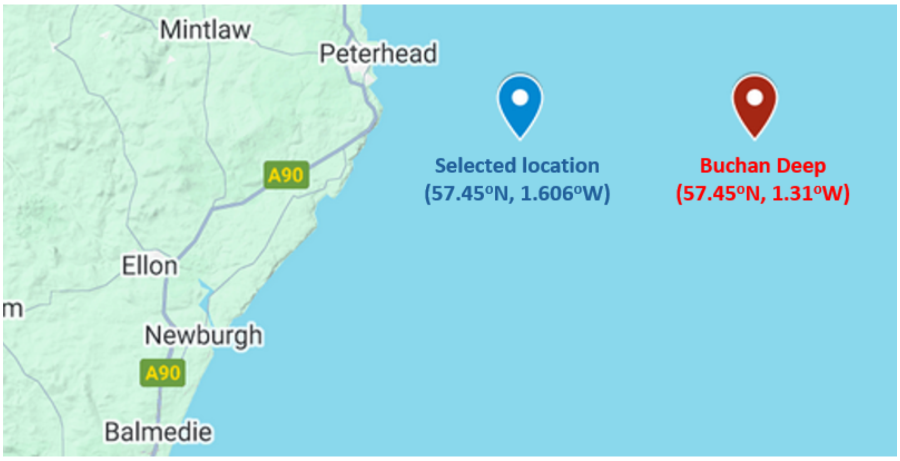

Figure 4.8: Selected 60 m water depth location and Buchan Deep

The distance between the two locations is approximately 18 km. According to standard DNV-RP-C205 [115], wave and wind climates are affected by large-scale weather patterns and can be assumed to be homogeneous over small regional distances. Furthermore, Holthuijsen [116] stated that wave direction is not significantly altered in deep or moderately deep waters. Therefore, it is a valid approach to adopt the most frequent wind and wave directions at Buchan Deep also for the selected location. To obtain the most probable wind and wave directions at Buchan Deep, the wind and wave rose were used, for the wind speed at 10 m and the significant wave height respectively [105]. This approach was also followed by Aguirre et al. [110], where they used real metocean data, including wind and wave directions, from Hywind Scotland wind farm, which they clustered via the Ward's minimum variance clustering method. In Figure 4.9, the aforementioned wind and wave roses in wind speed clusters of 5 m/s and significant wave height clusters of 2 m are shown. In addition, the detailed probabilities for the different wind speed and wave height clusters (of 2 m/s and 1 m respectively) can be seen in the work of Mathiesen et al. [105] and in Appendix Section A.4. From those tables, the most probable direction for every wind speed and wave height was defined and used as an input in the Inflow Wind and HydroDyn module, respectively. Overall, U_{hub}, H_s, T_p, wind and wave directions that were used in the simulations are shown in Table 4.5. These misalignments were considered to make the simulations more realistic. Furthermore, the load cases with the described wind and wave orientations of this table, will be called as realistic cases for the rest of this work.

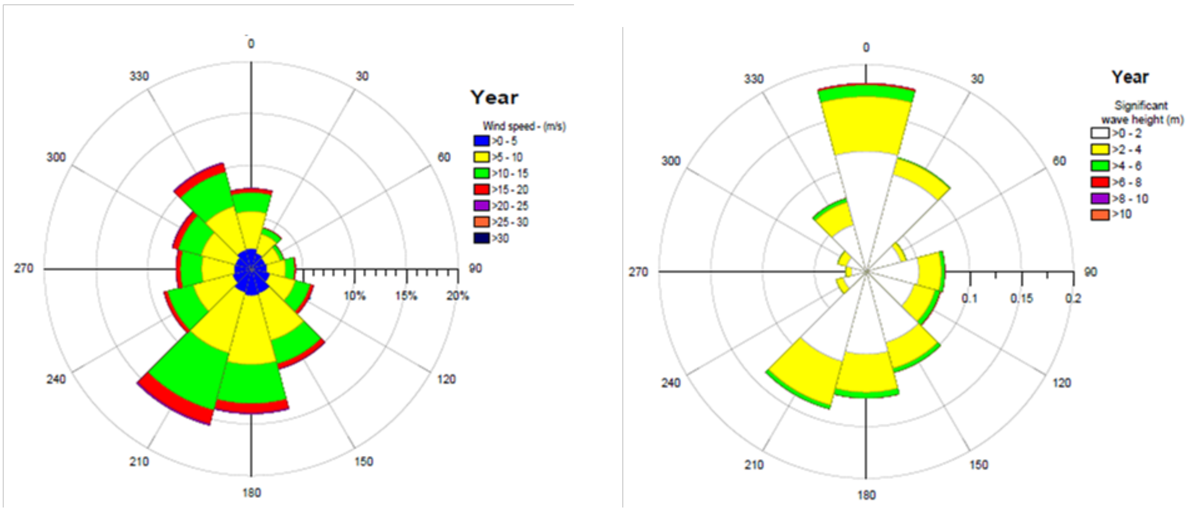

(a) Wind speed rose at 10 m above sea level at Buchan Deep

(b) Wave height rose at Buchan Deep

Figure 4.9: Distribution of wind speeds and significant wave heights at Buchan Deep for the period 1958-2010 [105]

LC	U_{hub}(m/s)	U_{10} (m/s)	H_s (m)	T_p (s)	Wind Origin | Heading (°)	Wave Origin | Heading (°)
1	4.5	3.18	0.80	7.72	180 | 0	30 | 210
2	5.5	3.89	0.91	7.59	180 | 0	30 | 210
3	6.5	4.59	1.03	7.48	180 | 0	0 | 180
4	7.5	5.30	1.16	7.39	180 | 0	0 | 180
5	8.5	6.01	1.29	7.33	180 | 0	0 | 180
6	9.5	6.72	1.44	7.29	180 | 0	0 | 180
7	10.5	7.42	1.59	7.26	180 | 0	0 | 180
8	11.5	8.13	1.75	7.25	210 | 30	0 | 180
9	12.5	8.84	1.91	7.25	210 | 30	0 | 180
10	13.5	9.54	2.08	7.26	210 | 30	0 | 180
11	14.5	10.25	2.26	7.30	210 | 30	0 | 180
12	15.5	10.96	2.45	7.34	210 | 30	0 | 180
13	16.5	11.67	2.63	7.38	210 | 30	0 | 180
14	17.5	12.37	2.83	7.44	210 | 30	210 | 30
15	18.5	13.08	3.03	7.50	210 | 30	210 | 30
16	19.5	13.79	3.23	7.57	210 | 30	210 | 30
17	20.5	14.49	3.43	7.65	210 | 30	210 | 30
18	21.5	15.20	3.66	7.74	210 | 30	210 | 30
19	22.5	15.91	3.89	7.83	210 | 30	210 | 30
20	23.5	16.61	4.11	7.92	210 | 30	210 | 30
21	24.5	17.32	4.34	8.02	210 | 30	210 | 30

Table 4.5: Wind and wave input conditions for simulated load cases

It is worth noting the directional orientation used in OpenFAST. In both Inflow Wind and HydroDyn, the wind and wave propagation can be defined, which corresponds to the direction to which the wind and wave are heading, respectively. A heading direction of $0°$ corresponds to wave or wind propagation in the positive x-axis direction, while a heading direction of $90°$ represents wave or wind propagation in the positive Y-axis direction, as shown in Figure 4.10. That means that considering an upwind WT that faces the South, a wind origin of $180°$ in Table 4.5 corresponds to $0°$ wind propagation (heading) direction in Inflow Wind and likewise, a wave origin of $30°$, corresponds to $210°$ wave heading direction in HyrdroDyn. The heading direction of the wind and wave are included next to the wind and wave origin correspondingly, in Table 4.5. Nevertheless, although wave propagation direction is defined counter-clockwise when looking from above, the positive wind propagation direction is defined as a clockwise rotation when looking from above toward the surface of the ocean [73, 75].

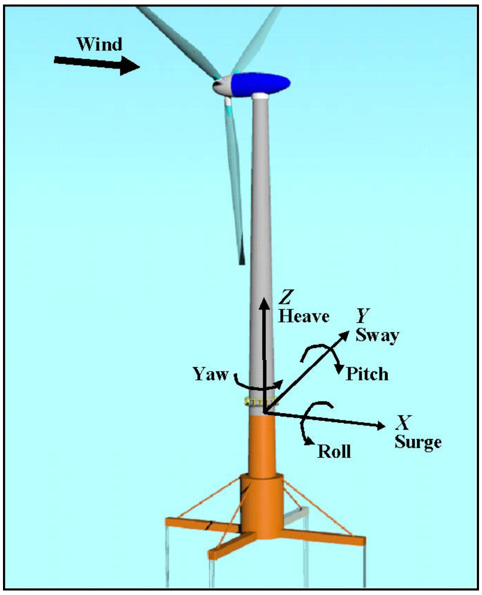

Figure 4.10: Wind Turbine coordinate system in OpenFAST [73]

Taking into account that simulations are performed separately for each wind speed and one dominant direction of wind and wave is considered for every wind speed, for every simulation a fixed nacelle yaw angle was set, equal to the wind heading direction. Finally, a second set of simulations was performed, in which the wind and wave are aligned with each other and with the rotor at every wind speed (wind and wave heading direction of $0°$). In doing so, the impact of wind and wave misalignment can also be analyzed. The load cases with this wind and wave orientation will be mentioned as aligned cases or aligned wind-wave cases for the next part of this thesis.

4.4.3. Wind Speed Probability

In Subsection 3.6.3, it was explained that the site-specific Weibull distribution must be defined, to account for the contribution of each operating wind speed to the MB fatigue damage. Since the wind speeds for the simulations are taken at the hub height, the Weibull distribution should also be calculated at the hub height. At the selected site of this thesis, in the paper of Li et al. [114], the Weibull coefficients required for Equation 3.38 are given at the reference height of 10 m. Consequently, the Weibull scale parameter at the hub height of 119 m is calculated by scaling the reference value provided at 10 m height using the power law, as:

$$\alpha_{\text{scale}}(z) = \alpha_{\text{scale}}(z_{\text{ref}}) \cdot \left(\frac{z}{z_{\text{ref}}}\right)^{\alpha_P} \tag{4.11}$$

where z_{ref} is equal to 10 m and, according to Li et al. [114], $\alpha_{scale}(z_{ref})$ is equal to 8.92 m/s. Thus, for the hub height, α_{scale} is equal to 11.4 m/s. Considering also that for the specific site [114], the shape parameter k is equal to 2.299, the Weibull probability distribution is shown in Figure 4.11.

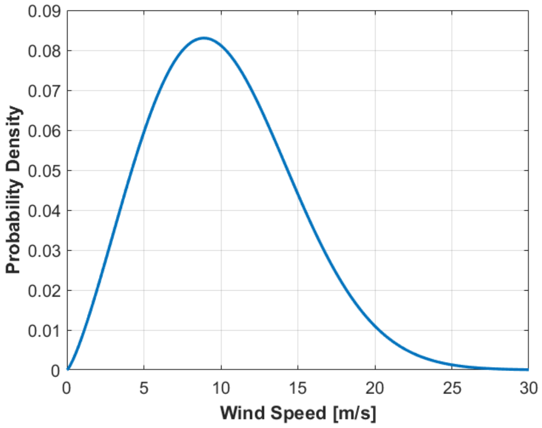

Figure 4.11: Weibull distribution for the selected location ($\alpha_{scale} = 11.4$ and $k_{shape} = 2.3$)

5

Results and Interpretation

In this chapter, the results of the implemented methodology are presented, along with an in-depth analysis and interpretation of them. Using the equations presented in Section 3.6, the loads acting on both the upwind main bearing (MB1) and the downwind main bearing (MB2) have been calculated. However, the analysis focuses on MB1, since it is the only one that fails to meet the 20-year design life, as shown in Section 5.2. MB1 is positioned first on the main shaft, therefore, it experiences the highest loads. The realistic wind and wave cases, introduced in Table 4.5, are the main object of the analysis. Aligned wind and wave cases are also added to show their similarity or considerable difference, which emphasizes the impact of wind and wave misalignment.

In Section 5.1 a comparison and interpretation of the main bearing loads of the BOWT and FOWT is presented, based on the LDD histograms, the load means and standard deviations, and the differences in aerodynamic and rotor performance. Furthermore, in the FOWT, the coupling of the loads with the platform motions is explained through their means and a physical interpretation. Then, in Section 5.2, the MB1 RUL and damage results are analyzed, followed by a parametric sensitivity analysis shown in Section 5.3, to identify the environmental and system parameters with the greatest impact on the MB1 fatigue damage. Specifically, turbulence intensity and H_s - T_p are examined as environmental parameters, while nacelle mass is considered as a system parameter for both WT configurations. In the case of the FOWT, platform mass and mooring line stiffness are included as additional system parameters.

5.1. Upwind Main Bearing Loads

5.1.1. LDD results

This section begins with the presentation of results from the LDD method. Figure 5.1 presents the LDD histograms for the realistic wind and wave orientations defined in Table 4.5, at wind speeds of 7.5 m/s, 11.5 m/s, 16.5 m/s, and 23.5 m/s. Similarly, Figure 5.2 (a,b) and Figure 5.2 (c,d) show the LDD histograms for the aligned wind and wave cases at wind speeds of 7.5 m/s, 11.5 m/s, and 16.5 m/s, 23.5 m/s, respectively.

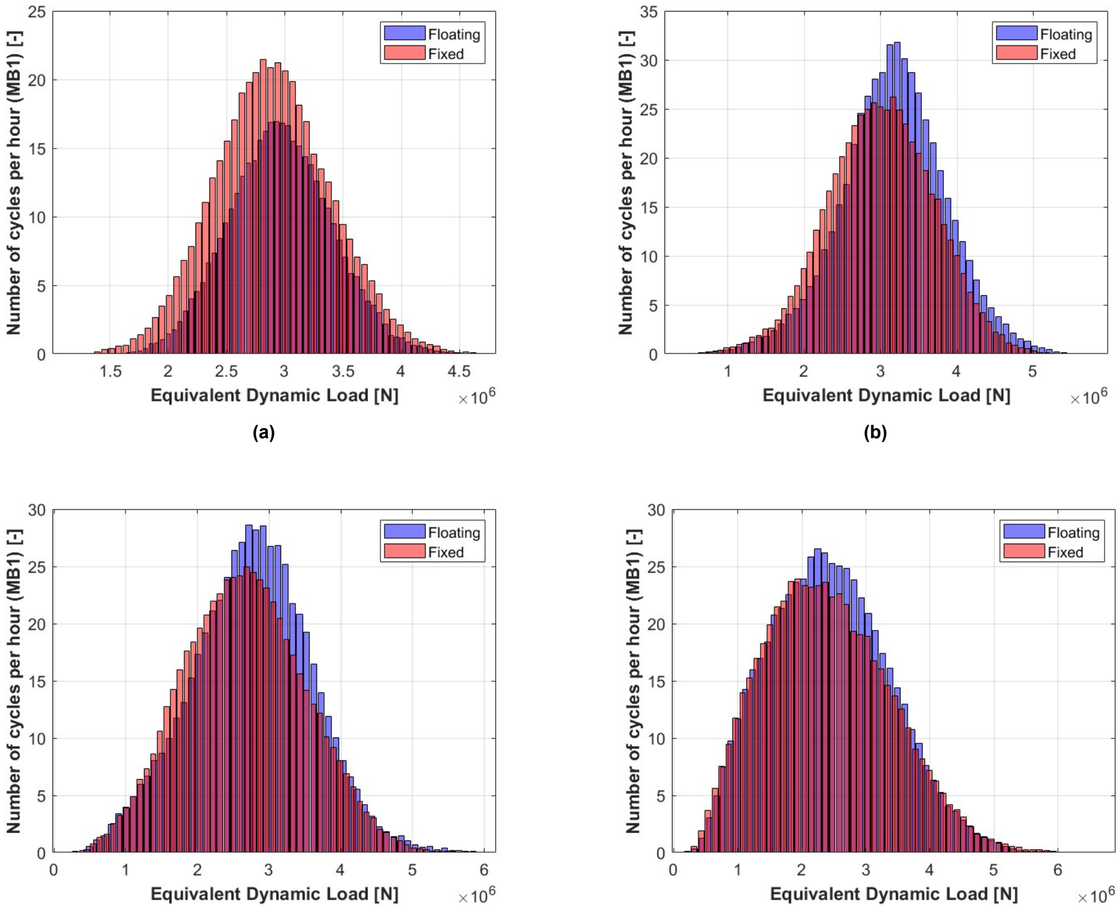

(a) (b)

(c) (d)

Figure 5.1: Realistic case: LDD histograms for FOWT and BOWT for four different wind speeds: (a) 7.5 m/s, (b) 11.5 m/s, (c) 16.5 m/s and (d) 23.5 m/s.

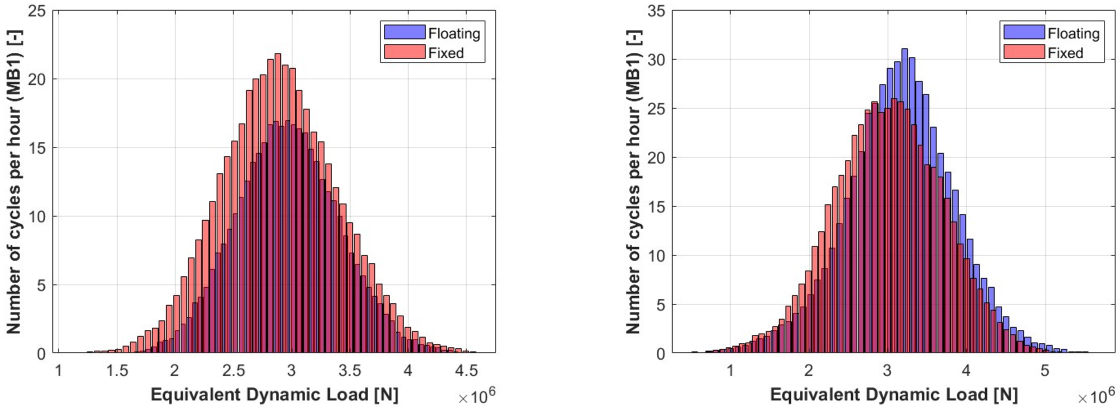

(a) (b)

Figure 5.2: Aligned wind-wave case: LDD histograms for FOWT and BOWT: (a) 7.5 m/s and (b) 11.5 m/s.

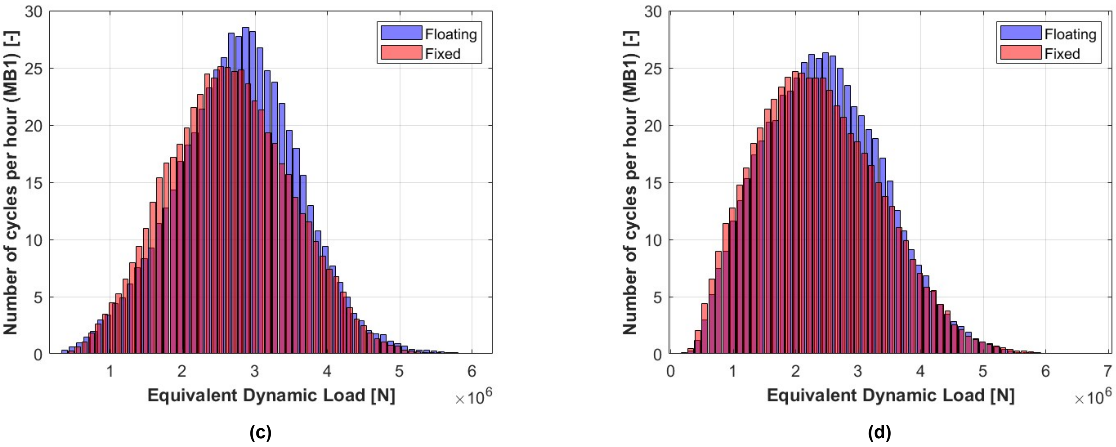

Figure 5.2: Aligned wind-wave case: LDD histograms for FOWT and BOWT: (c) 16.5 m/s and (d) 23.5 m/s.

One first observation is that in the below-rated region, the MB1 of the BOWT experiences more hourly load counts for both realistic and aligned cases. However, above the rated wind speed of 11.4 m/s, it is shown that the MB1 of FOWT is subjected to more cycles at higher values of the dynamic equivalent load for both realistic and aligned wind-wave conditions.

This behavior could be attributed to the platform motion that leads to higher and more varying loads on the MB1, especially at higher wind speeds. The values of the x-axis of the LDD histogram depend on the mere values of the dynamic equivalent load P, defined in Equation 3.18. The number of hourly cycles (y-axis of the LDD histogram) is influenced by the rotational speed of the main shaft, as explained in Equation 3.34 to Equation 3.36. The relationship between platform motions, MB1 loading, and rotational speed will be explained in more detail in Subsection 5.1.2 to Subsection 5.1.4.

More LDD histogram plots are included in Appendix B for further verification of the aforementioned behavior and the similarities between realistic and aligned wind-wave cases.

5.1.2. Loads comparison and interpretation

The upwind main bearing connects the hub to the nacelle through the main shaft and supports the mass of the rotor in combination with the downwind main bearing, compensating for the loads and moments acting on the hub and the main shaft. In this section, the loads acting on MB1 are analyzed as a function of wind speed for the simulated load cases, based on their means and standard deviations. Load and motion time series were also considered but are not included in detail in the present analysis, except for a few indicative examples. It should also be highlighted that the shaft coordinate system, described in Figure 3.11 refers to a downwind wind turbine according to the OpenFAST documentation [74]. For this project, models of an upwind wind turbine are considered (the wind meets the rotor first and then flows past the nacelle). Therefore, the local coordinate system of the shaft, which is used as the reference for the calculated loads, follows the orientation shown in Figure 5.3.

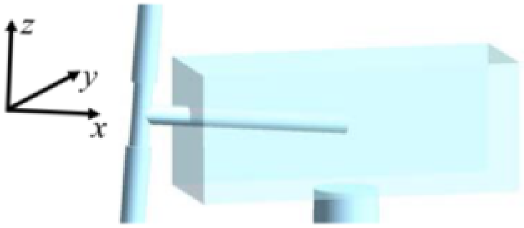

Figure 5.3: Coordinate System of Upwind Wind Turbine in OpenFAST [80]

Dynamic Equivalent Loads

In Figure 5.4, the means and standard deviation of the dynamic equivalent load P are shown, for the realistic and aligned wind-wave orientations, respectively.

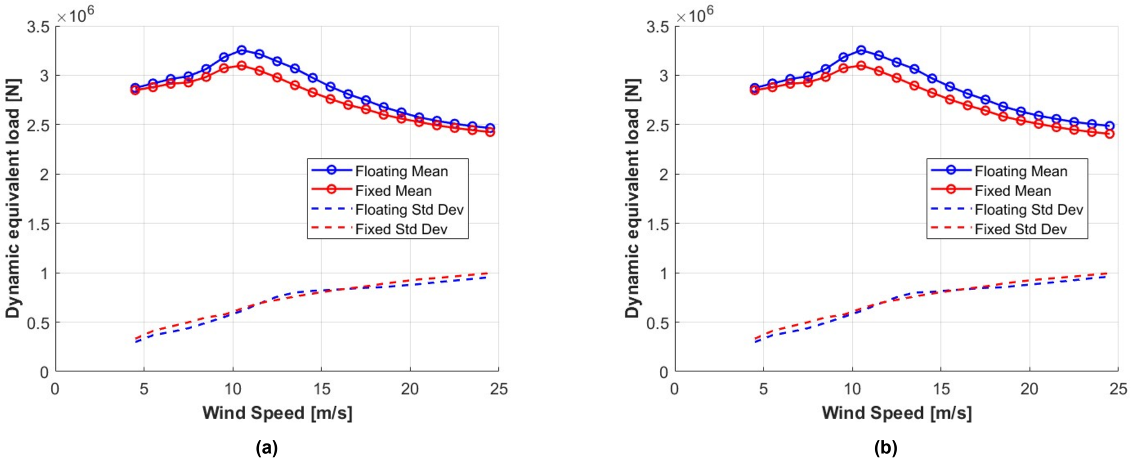

Figure 5.4: Dynamic equivalent load, P, mean and standard deviation as a function of wind speed for: (a) realistic case and (b) aligned case

It can be seen that the P loads, in both sets of simulations,increase in the below-rated region due to the increasing wind speeds and aerodynamic loads but they start decreasing after 10.5 m/s. This indicates the impact of the blade pitch control which is activated just before the rated wind speed for a smooth transition and is implemented in the above-rated region to keep the WT at the rated generated power and rotor speed. The controller effect will be explained in more detail later in this chapter. In contrast, the standard deviation of the P loads keeps increasing slightly and steadily with increasing wind speeds. Furthermore, similar pattern to the realistic cases can be noticed in the aligned wind and wave cases, indicating that wind-wave misalignment in realistic cases above 11.5 m/s, as shown in Table 4.5, has a negligible effect on the dynamic equivalent load.

Finally, the dynamic equivalent load appears to be generally higher in the FOWT than in the BOWT in most of the operating wind speeds, except for the low wind speeds and, in the realistic cases, for the higher wind speeds close to the cut-out. The maximum mean load P for the MB1 of both FOWT and BOWT appears at 10.5 m/s, with values of 3.25 MN for the FOWT and 3.10 MN for the BOWT, respectively. The maximum relative difference between the two WT configurations is 5.83%, at 13.5 m/s.

According to Equation 3.18, the equivalent dynamic load P of the main bearing consists of the axial and radial load, thus, these loads are analyzed separately. In Figure 5.5, a simplified sketch of the two main bearings is given, showing the nacelle, the hub and the blades, the shaft tilt angle and how axial and radial loads act on the main bearings.

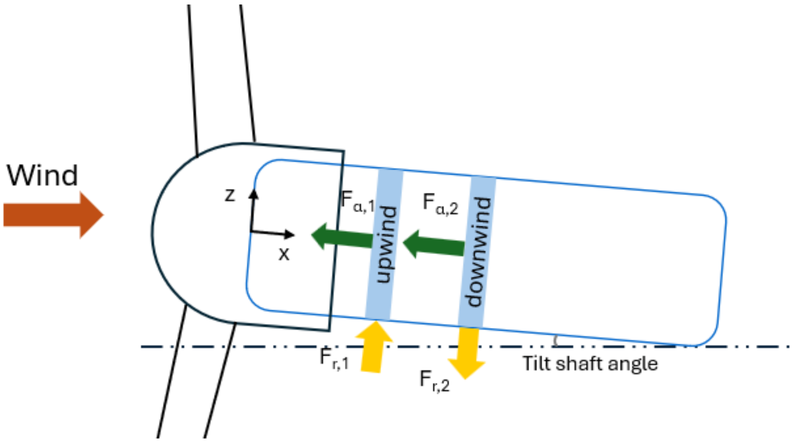

Figure 5.5: Simplified sketch of the main bearings and their reaction forces

Axial Loads

The axial loads (F_α) are strongly related to the aerodynamic loads and in particular, the thrust force of the rotor, but they can also be affected by gravitational loads, especially when the shaft is tilted. In the case of FOWTs, additional contributions arise from platform motions, which further amplify these effects.

Figure 5.6 presents the time series of axial load on MB1 for both WT configurations, at 8.5 and 13.5 m/s, under realistic wind and wave conditions. At 8.5 m/s, both BOWT and FOWT exhibit similar patterns. In contrast, at 13.5 m/s, FOWT shows a much wider range of magnitudes of axial load, due to the semi-submersible platform motion that differentiates the wind inflow conditions. This results in a higher standard deviation of the axial load at this wind speed. Moreover, the recorded variability of the loads is due to the applied turbulent conditions in both WT configurations and is amplified by the semi-submersible platform motion for the FOWT.

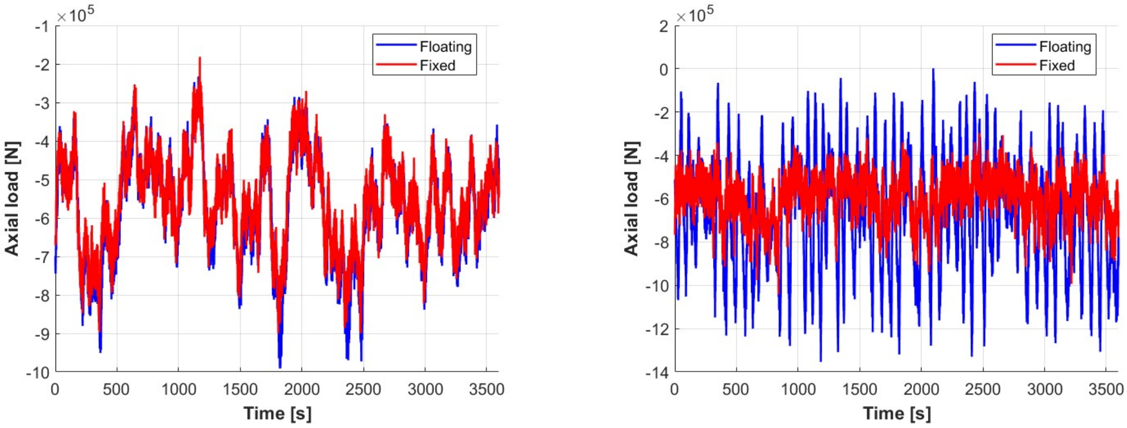

(a) (b)

Figure 5.6: Realistic case: Time series of MB1 axial load $F_{\alpha,1}$ at (a) 8.5 and (b) 13.5 m/s

The time series of individual wind speeds provides limited insight into the overall loading characteristics across the full wind speed range. Therefore, the mean and standard deviations of the MB1 axial load $F_{\alpha,1}$ are used over the full wind speed range, which are shown in Figure 5.7, along with the rotor thrust force T, in realistic cases. The results for the aligned wind-wave cases are similar, thus, they are not shown here, but are included in Appendix C for completeness.

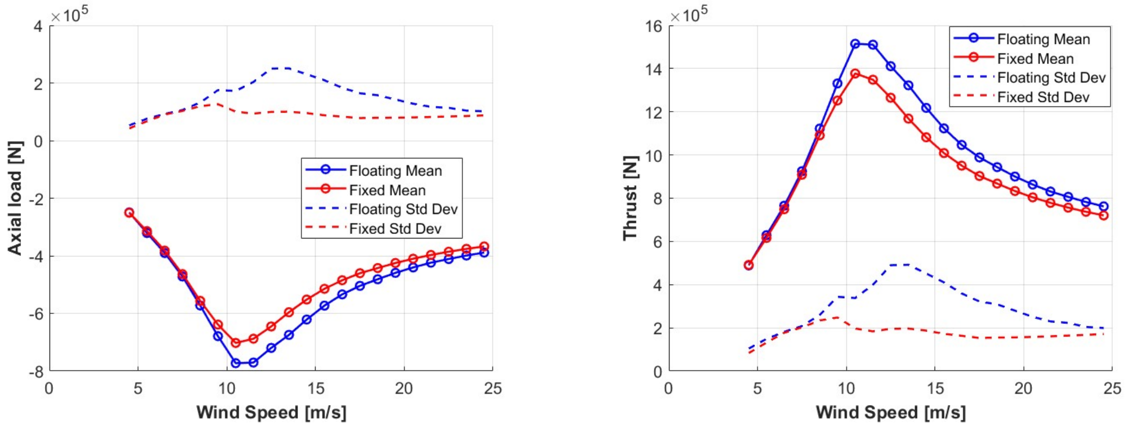

(a) MB1 axial load, $F_{\alpha,1}$, mean and standard deviation **(b)** Thrust force, T, mean and standard deviation

Figure 5.7: Realistic case: (a) MB1 Axial load, $F_{\alpha,1}$, and (b) thrust force, T, mean and standard deviation as a function of wind speed

The axial load follows the same pattern as the thrust force but with opposite sign, acting toward the negative x-axis (shown in Figure 5.3). Both loads decline in the above-rated region, similarly to the dynamic equivalent load shown in Figure 5.4. This behavior is due to the blade pitching which reduces thrust force to maintain rated power. This is also confirmed by Figure 5.8 which shows that the blade pitch angle is increased in the above-rated region, reaching up to a value of almost 23°. However, it is notable that the axial and thrust load is higher for the FOWT than for the BOWT, both in terms of mean and standard deviation. The maximum mean MB1 axial load for the FOWT is 773 kN and occurs at 10.5 m/s, while for the BOWT the corresponding value is 703 kN. The maximum difference in mean axial load between FOWT and BOWT is equal to 13.17% for 13.5 m/s.

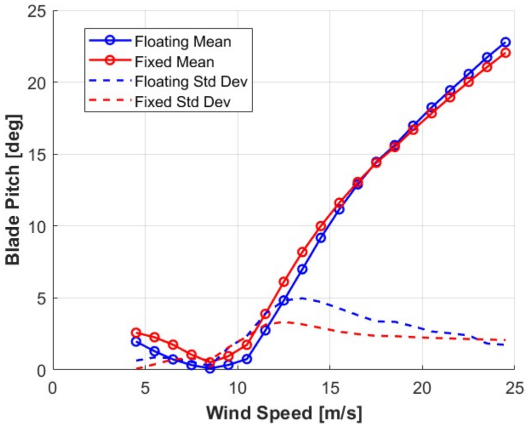

Figure 5.8: Realistic case: Blade pitch angle, mean and standard deviation as a function of wind speed

Platform Pitch and Surge motion

To explain the difference in thrust loads between FOWT and BOWT, it is significant to look into the surge and pitch motions of the platform, as they are the most relevant to the axial direction. These two platform motions are shown in Figure 5.9 and it is obvious that there is a correlation between them and the thrust load pattern shown in Figure 5.7b. This is due to the fact that, apart from the waves that influence the platform motion, which is compensated by the mooring system, also the thrust force affects the surge and pitch motion, by “pushing” the WT in the x-direction. More statistics of the platform motions over the operating wind speeds are provided in Appendix D.

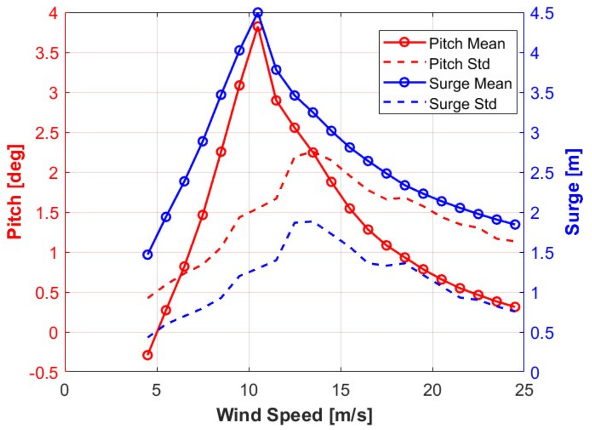

Figure 5.9: Realistic case: Platform pitch and surge motion, mean and standard deviation as a function of wind speed

Both pitch and surge motion have positive means, with a maximum mean of 3.8° and 4.5 m, respectively, at 10.5 m/s. This is the cause of the increase in thrust observed in FOWT compared to BOWT. Physically, a positive pitch angle turns the rotor and the blade airfoils upwards (clockwise) and increases the angle of attack α on the rotor and the blades. In this way, as can be seen in Figure 3.4 and Figure 3.5 and from Equation 3.5a to Equation 3.8, the lift force and in turn F_n and thrust are increased. Additionally, positive surge motion moves the FOWT towards the heading direction of the wind, thus, the rotor experiences a higher effective wind speed (sum of the real wind speed and the surge speed), which increases the thrust, according to Equation 3.6. An illustration of the positive pitch and surge motions is given in Figure 5.10.

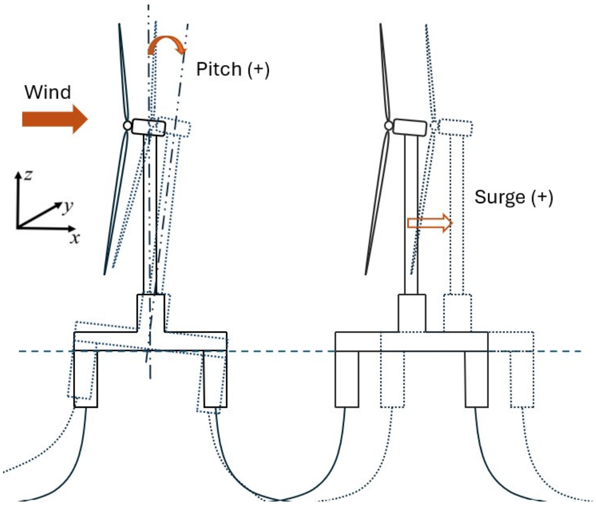

Figure 5.10: Representation of positive pitch and surge motion for FOWT

Radial loads and platfom Heave, Sway, Roll and Yaw motion

Radial loads (F_r), which are divided into forces acting on the y- and z- direction, as shown in Equation 3.31, are mostly dependent on the gravitational loads of the rotor, and the rest of the drivetrain components. The lateral wind loads also have an influence, especially when the main shaft is tilted or misaligned with the horizontal plane. The mean and standard deviations of the radial loads and the mean of its components for the MB1 and the realistic cases are depicted in Figure 5.11a and Figure 5.11b, respectively. Similar patterns are observed for these loads in the aligned wind-wave cases.

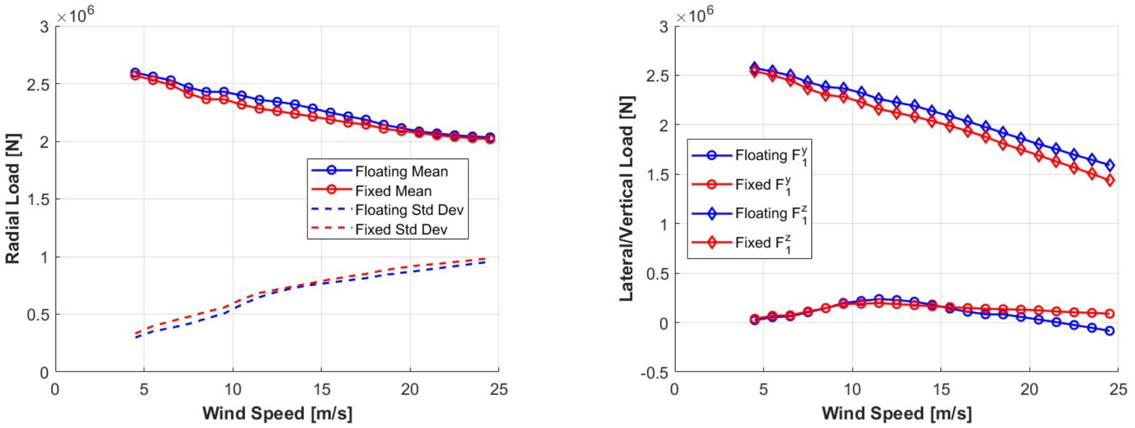

(a) Radial load, $F_{r,1}$, mean and standard deviation

(b) Lateral, F_1^y, and vertical load, F_1^z, means

Figure 5.11: Realistic case: MB1 Radial load, $F_{r,1}$, and its components, F_1^y and F_1^z, as a function of wind speed

The figures indicate that the mean radial load is generally slightly higher in the FOWT than the BOWT, apart from low wind speeds close to the cut-in and high wind speeds close to cut-out wind speeds. In the former region, it is clear that F_1^y and F_1^z are very close for FOWT and BOWT, while in the latter region, F_1^z is higher and F_1^y lower for the FOWT. Thus, from Equation 3.31, they yield an approximately similar mean radial load. With respect to radial load standard deviations, they increase with increasing wind speeds, showing that higher wind speeds and harsher conditions amplify the variability and turbulence of the loads.

Finally, the declining trend of the radial load in both WT configurations, can be attributed to the activation of pitch control and reduction of aerodynamic loads, in the above-rated region. Specifically, the effect of the blade pitching is clear on the variation of F_1^y, shown in Figure 5.11b, since F_1^y decreases in the above-rated region for both WT configurations. In the below-rated region, the $F_{r,1}$ reduction can be justified by the fact that the WT operates further from optimal aerodynamic performance in the lowest operating wind speeds, as will be explained in detail in Subsection 5.1.4.

The mean value of the radial load of the upwind main bearing is maximized at 4.5 m/s for both the FOWT and BOWT with 2.59 MN and 2.57 MN, respectively, while the maximum difference of the quantities for the two WT configurations is found at 13.5 m/s as 3.66%. Furthermore, as shown in Figure 5.11b, F_1^z constitutes the dominant component of radial loading (71-99% across wind speeds for both WT configurations), while F_1^y contributes significantly less (1-4%).

To explain the behavior of F_1^z and F_1^y, it is appropriate to recall their definitions, provided in Equation 3.22 and Equation 3.24 accordingly. According to them, F_1^z depends on the vertical load acting on the hub, F_h^z, and the hub moment M_h^y, which are shown in Figure 5.12. F_1^y is influenced by the lateral hub load, F_h^y, and the hub moment M_h^z.

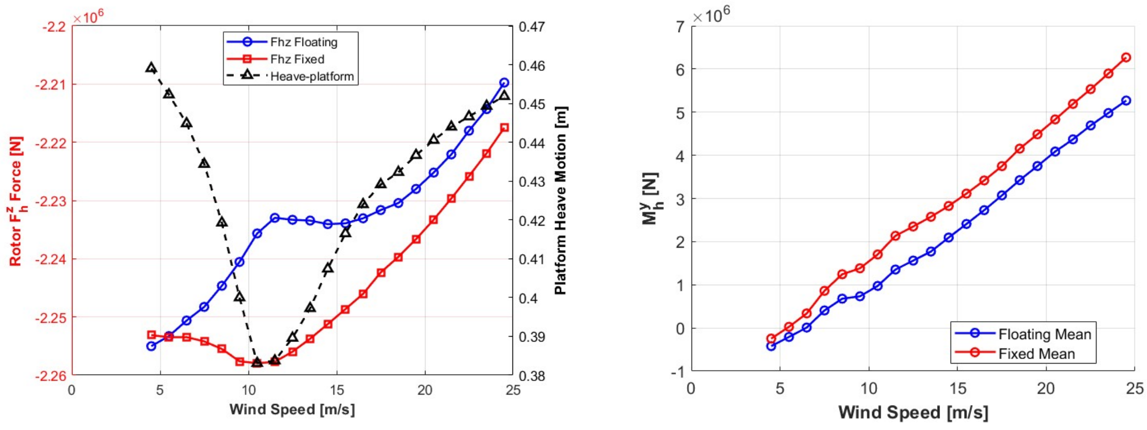

(a) Hub force F_h^z and platform heave motion means

(b) Hub moment M_h^y means

Figure 5.12: Realistic case: Hub force, F_h^z, and moment, M_h^y, related to MB1 vertical load, F_1^z as a function of wind speed

The mean vertical force F_h^z, shown in Figure 5.12a, is negative along all wind speeds, indicating that its direction is vertical downward. It depends both on the wind loads and the weights of the components. For the BOWT, it follows the trend of the thrust, so it starts reducing in the above-rated region. However, for the FOWT, mean F_h^z is lower in magnitude, at all wind speeds. This is partially due to the heave motion, which is the vertical motion of the platform and depends both on the waves and the wind loads.

In the below-rated region, the heave motion mean declines, which means that the platform mostly moves vertically downwards. Thus, heave absorbs some of the vertical load, by exerting an upward reaction force, which leads to a lower F_h^z for the FOWT. At around-rated region, the heave mean displacement is minimized, while the blade pitch starts increasing, resulting in a short flattening of the FOWT F_h^z curve. Then, in the above-rated region, thrust force begins to decrease, as shown in Figure 5.7b. This contributes to a further reduction of the FOWT F_h^z, causing the FOWT platform to start moving upwards again. Notably, the limited variation of the mean heave motion across the wind speeds range (around 8 cm) shows an effective vertical stability of the semi-submersible platform.

The mean pitching moment M_h^y (Figure 5.12b) is continuously increasing with higher wind speeds, due to higher turbulent conditions and more uneven thrust distribution in the rotor disk, that amplifies this moment. This is due to the wind shear, which induces higher wind speed on the top of the rotor disk than its bottom, as also mentioned in Subsection 3.3.1. Moreover, M_h^y is lower in the FOWT than in the BOWT, because as shown in Figure 5.9 and Figure 5.10, positive pitch motion of the platform turns the rotor upwards. This decreases the wind shear imbalance and also the gravitation effect on the moment. The latter result means that, at a higher upward tilt of the rotor and the shaft, the components' weights form a larger angle ϕ with the z-axis of the shaft, leading to smaller moment contribution from the gravitational loads.

This is depicted in Figure 5.13, assuming that W denotes the combined weight of the rotor and the hub. For a larger angle of the nacelle with the horizontal direction, which is portrayed in the right sketch with angle ϕ_2, the component W_z along the z-axis of the nacelle, is of lower magnitude. This is also explained by Equation 5.1a, since a larger angle ϕ gives a lower $\cos\phi$. Subsequently, W_z creates a smaller moment around the middle point in the spacing between the two main bearings (since the level arm L stays constant). In contrast, a larger angle ϕ gives a higher $\sin\phi$. Thus, according to Equation 5.1b there is a higher contribution of W_x in the axial direction and subsequently the axial load experienced by MB1. The same impact holds for the weight loads of the remaining components, such as the gearbox and the generator, which are located to the right of the midpoint between the two main bearings, but their moments have an opposite sign.

$$W_z = W \cdot \cos\phi \qquad (5.1a) \qquad\qquad W_x = W \cdot \sin\phi \qquad (5.1b)$$

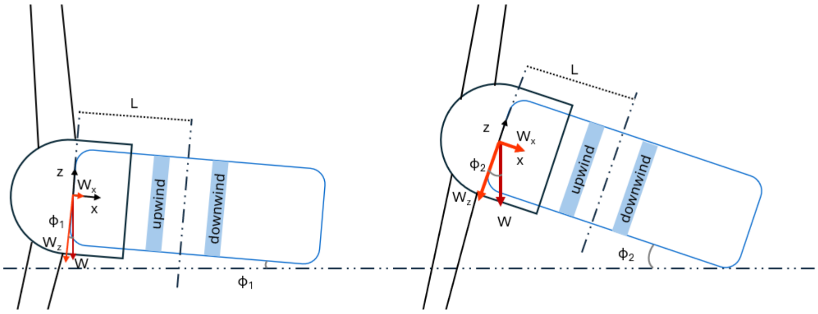

Figure 5.13: Simplified sketch showing the different contribution of the weight of components for a higher nacelle angle with the horizontal

Next, Figure 5.14 shows the lateral hub load F_h^y and the hub moment M_h^z, which influence the MB1 lateral load, F_1^y, according to Equation 3.24.

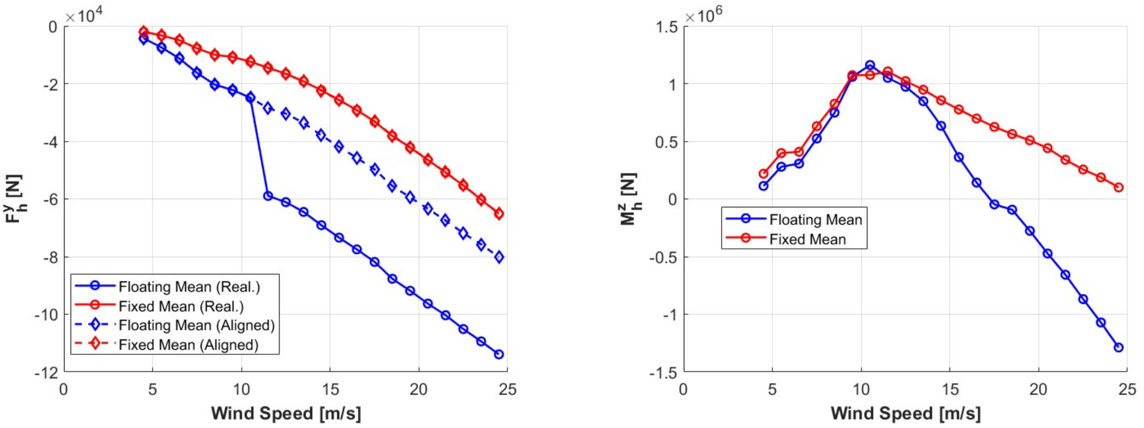

(a) Realistic and aligned case: Hub force F_h^y means

(b) Realistic case: Hub moment M_h^z means

Figure 5.14: Hub force, F_h^y, and hub moment, M_h^z, as a function of wind speed

Figure 5.14a shows that the mean lateral force F_h^y is constantly negative along all wind speeds and of higher magnitude for the FOWT. In the realistic cases, there is an abrupt change between 10.5 and 11.5 m/s, which is caused by a change in wind-wave misalignment of 30°, as can be seen in Table 4.5. In contrast, in the aligned wind-wave cases, F_h^y keeps a similar inclination, while for the BOWT, F_h^y has the same mean values for both realistic and aligned cases.

The negative value implies some lateral misalignment causing the wind to meet the rotor from a misaligned direction (heading to the negative direction of y-axis as depicted in Figure 5.3). This can also be derived from Figure 5.15a, where rotor skew angle is depicted for the FOWT and BOWT, for both realistic and aligned wind-wave cases. Rotor skew angle is an output of AeroDyn module that computes the universal inflow angle (both on horizontal and vertical plane). For the FOWT, the mean rotor skew angle is higher and reaches up to 9.5° at 11.5 m/s, while for the BOWT and the realistic cases, some slight changes in the inclination are caused by changes in wind-wave misalignment, as shown in Table 4.5. These small steps occur because of the discrete simulations performed for each wind speed and wind-wave direction.

Although this inflow angle variation may appear high, according to Hart et al. [65], during normal operation, the difference between nacelle yaw angle and mean wind inflow direction is kept within $\pm 8°$, that can be slightly higher for FOWTs. The lateral imbalance is higher in the FOWT, due to the sway, roll and yaw motion of the platform, which are illustrated in Figure 5.15b, Figure 5.16a and Figure 5.16b, correspondingly. In these figures, the difference between realistic and aligned wind-wave cases for FOWT is also clear, through the sudden shift between 10.5 and 11.5 m/s, because of the change in wind-wave misalignment by 30°, similarly to the F_h^y. However, below 10.5 m/s, the two different sets of simulations have exactly the same values.

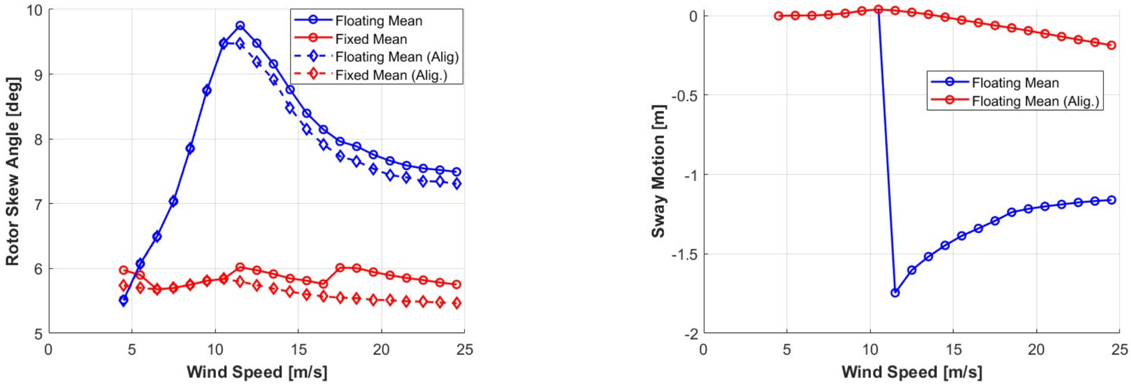

(a)

(b)

Figure 5.15: (a) Rotor skew angle for FOWT and BOWT and (b) FOWT platform sway motion, means, as a function of wind speed for realistic and aligned wind-wave cases

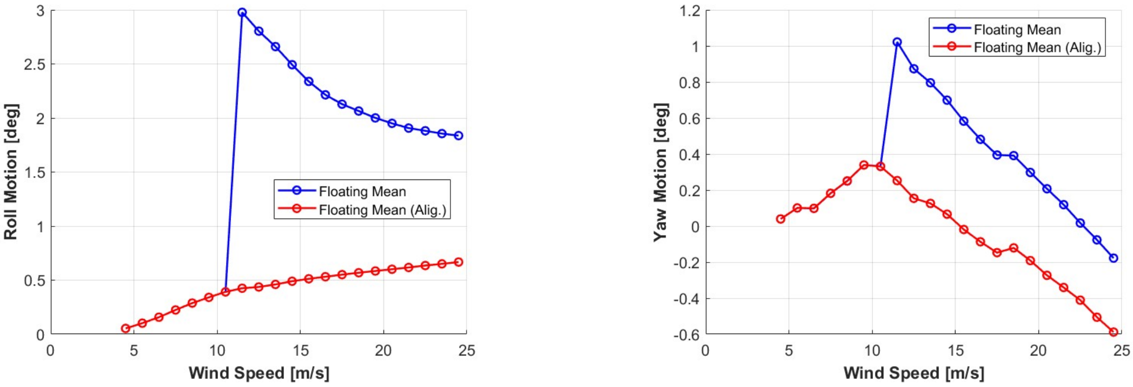

(a)

(b)

Figure 5.16: (a) Platform roll and (b) yaw motion, means, as a function of wind speed for realistic and aligned wind-wave cases

It is clear that FOWT platform motions in the aligned wind-wave cases show a minimal mean variation compared to the realistic cases. For aligned cases, mean sway motion ranges from 0.001 to -0.18 m across the operating wind speeds, roll motion stays positive across the wind speed range (0.05 to 0.67°), while mean yaw motion ranges from 0.04° to -0.59°. In contrast, realistic cases show significant shifts between 10.5 and 11.5 m/s, when the wind-wave misalignment changes by 30°, as already mentioned in Table 4.5. This change induces the highest means in the realistic cases: -1.7 m for sway, 3° for roll, and 1.02° for yaw motion.

According to Figure 5.14b, M_h^z, as the moment created with respect to the vertical axis z, is highly dependent on the inflow wind asymmetries and increases up to the rated wind speed with increasing thrust force on the rotor. After that point, the mean M_h^z starts declining with the activation of the blade pitch control and for the FOWT, it even changes sign after 17.5 m/s. This sign shift can be attributed to combined effects of rotor skew angle, sway, roll and yaw motions. Since M_h^z has higher magnitude than F_h^y, it primarily determines the shape of the MB1 lateral load F_1^y, shown in Figure 5.11b.

In the realistic cases, the sway motion of the platform is mostly negative, whereas the roll motion is positive. According to Figure 4.10, and to gain a better understanding of the lateral wind asymmetry that occurs in the FOWT, the positive roll motion and negative sway motion are shown in Figure 5.17, where it is assumed that the wind meets the rotor from the front (inwards). Positive yaw motion corresponds to a rotation of the platform counterclockwise, while looking the WT from above or to the right while facing the rotor from the front side.

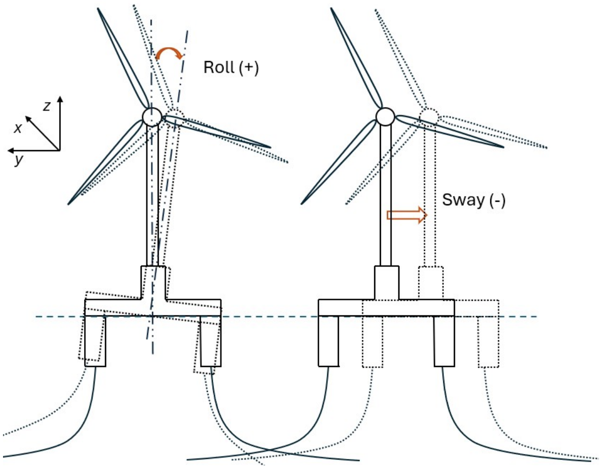

Figure 5.17: Representation of positive roll and negative sway motion for FOWT

5.1.3. Main Bearing Loads Summary

After the thorough analysis of the upwind main bearing loads performed in Subsection 5.1.2, in this section, a summary of the most important key findings is shown in table Table 5.1. For each load component acting on MB1, the table shows: the maximum value and the maximum percentage difference (max diff.) between FOWT and BOWT configurations, and the wind speed (ws) at which they occur. Furthermore, the gradient of every load is noted, and only for the FOWT, for every load, the influencing platform motions are shown. The gradient of the curves aims to indicate how the corresponding load evolves across the wind speeds and is defined as “+”, if the loads increase with wind speeds compared to the value at the lowest operating wind speed (4.5 m/s), “-”, if the load decreases and “0”, if it remains almost constant. In case a load changes inclination, for instance, first rises, but then after a few wind speeds, is reduced, the gradient is mentioned as “+-”.

Table 5.1: Summary of MB1 load characteristics for FOWT and BOWT and platform motion effects

Variable	**Gradient**		**Max value (certain ws)**		**Max diff. (%) (certain ws)**	**Platform DOF (Floating)**
	Floating	**Fixed**	**Floating**	**Fixed**		
$P[MN]$	+-	+-	3.25 (10.5 m/s)	3.10 (10.5 m/s)	5.83% (13.5 m/s)	All DOFs
$F_a[kN]$	+-	+-	773 (10.5 m/s)	703 (10.5 m/s)	13.17% (13.5 m/s)	Surge, pitch
$F_r[MN]$	-	-	2.59 (4.5 m/s)	2.57 (4.5 m/s)	3.66% (13.5 m/s)	All except for surge
$F_1^y[kN]$	+-+	+-	237 (11.5 m/s)	197 (11.5 m/s)	22.35% (12.5 m/s)	Sway, roll, yaw
$F_1^z[MN]$	-	-	2.57 (4.5 m/s)	2.54 (4.5 m/s)	10.77% (24.5 m/s)	Heave, pitch, surge

Table 5.1 shows that the dynamic equivalent load P is slightly higher in the FOWT than in the BOWT, with a maximum difference of 5.83% at 13.5 m/s. The axial load F_α exhibits a more significant increase (13.17%), due to the surge and pitch motions of the floating platform. The largest difference is seen in the lateral load F_y^1 (22.35%), indicating that the lateral MB1 loading is strongly amplified by the sway, roll and yaw platform motions.

5.1.4. Aerodynamic and Rotor Performance Comparison

In Subsection 5.1.1, it was briefly mentioned that the load cycles of the MB1 portrayed in the histograms of the LDD method, and subsequently their contribution to fatigue damage, are influenced by the rotational speed of the rotor (and the main shaft). In this section, the differences in rotor speed between the FOWT and the BOWT are analyzed, after having presented the impact of the various platform motions on MB1 loads, in Subsection 5.1.2. Firstly, in Figure 5.18, the mean rotor speed is presented as a function of the wind speed for the FOWT and BOWT in the realistic case, while the results are similar for the aligned wind-wave case. Moreover, standard deviation bars are used for a few wind speeds that generally show a higher variability for the rotor speed of the FOWT. The high deviation of the rotor speed from the rated value is caused by the simulated intense turbulent conditions of IEC class A.

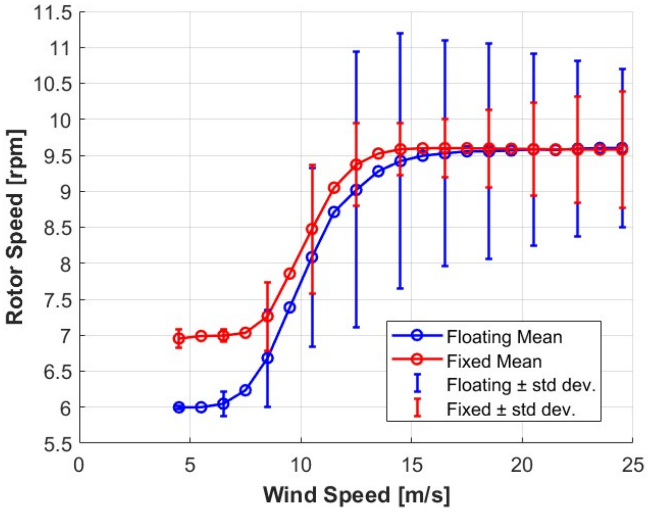

Figure 5.18: Realistic case: Rotor speed, mean and standard deviation, as a function of wind speed

It is evident that the FOWT has lower mean rotor speed in the below-rated region and especially for wind speeds lower than 8.5 m/s. This also causes less load cycles for the MB1 of the FOWT in the below-rated region, as already shown in the LDD histograms at 7.5 m/s in Figure 5.1a. Especially at wind speeds of 4.5 to 6.5 m/s, the mean rotor speed of the FOWT stays close to the minimum rotor speed of 6 rpm, whereas for the BOWT the corresponding value is 7 rpm. Even in the initial part of the above-rated region, the mean rotor speed of the FOWT is slightly lower than that of BOWT revealing the difficulty of the FOWT to reach the rated rotor speed of 9.6 rpm, due to platform motions and more unsteady wind inflow, which was explained in Subsection 5.1.2.

To interpret the difference in low operating wind speeds, it is essential to examine the generator torque control law that is implemented in the below-rated region and cited in Equation 3.15. The rotor speed is related to the generator speed through Equation 3.16, where the gearbox ratio is equal to 50 for the DTU 10 MW RWT drivetrain, as written in Table 4.2. In Figure 5.19, the mean generator torque and power are shown as a function of wind speed. In the below-rated region the mean power is almost identical for the FOWT and the BOWT, but the mean generator torque of the FOWT is a bit higher (up to 26%), which has as a result the lower generator speed and in turn, rotor speed.

In the above-rated region, apart from the active blade pitch control, constant generator torque control is used, that, according to Jonkman [119] and Abbas et al. [94], can help enhance the FOWT platform stability. Therefore, in Figure 5.19a, it is shown that the generator torque of the FOWT and BOWT is quite close, also in the above-rated region. However, the rotor speed and the generator power of the FOWT are slightly lower in the first above-rated wind speeds and they do not reach directly their rated values, as illustrated in Figure 5.18 and Figure 5.19b, respectively.

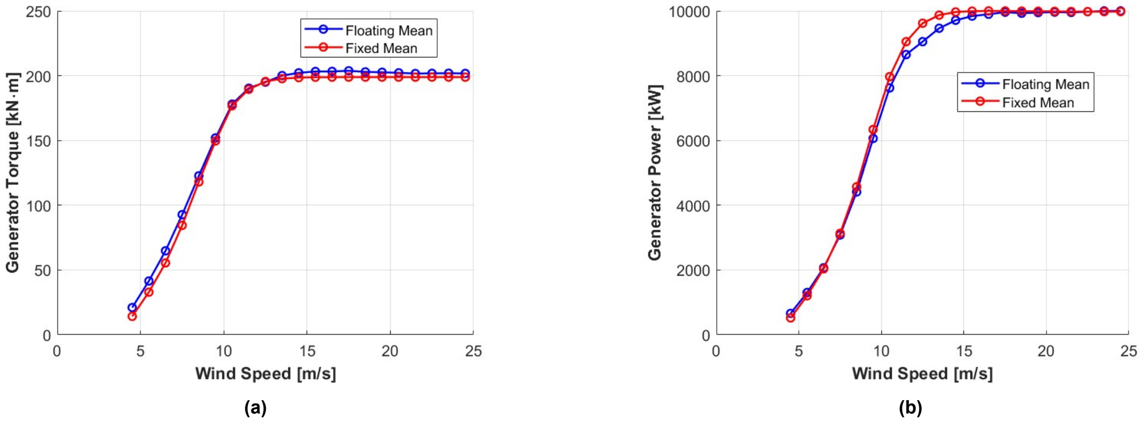

(a) (b)

Figure 5.19: Realistic case: Mean (a) Generator Torque and (b) Power as a function of wind speed

Finally, to gain a better understanding of the operation of the two WT configurations in the below-rated region, in Figure 5.20, the mean TSR as a function of wind speed and the mean power coefficient C_P as a function of TSR for the FOWT and the BOWT are depicted. The design or optimal TSR λ_{design} is defined from Figure 5.20b as the value of TSR, for which C_P is maximized. Thus, from Figure 5.20b, it can be extracted that for the FOWT, $C_{P,max,fl} = 0.4956$ and $\lambda_{\text{design,fl}} = 8.082$, while for the BOWT, $C_{P,max,fix} = 0.491$ and $\lambda_{\text{design,fix}} = 8.355$. Stated differently, FOWT has a higher $C_{P,max}$ and a lower λ_{design} than BOWT, which arises from the platform motions that create unsteady inflow conditions for the FOWT compared to its bottom-fixed counterpart. Moreover, as shown in Figure 5.20a, the deviation of TSR from its design value in the below-rated region (corresponding to the right part of Figure 5.20b), which is higher for lower wind speeds, implies a suboptimal operation of both WTs at low wind speeds.

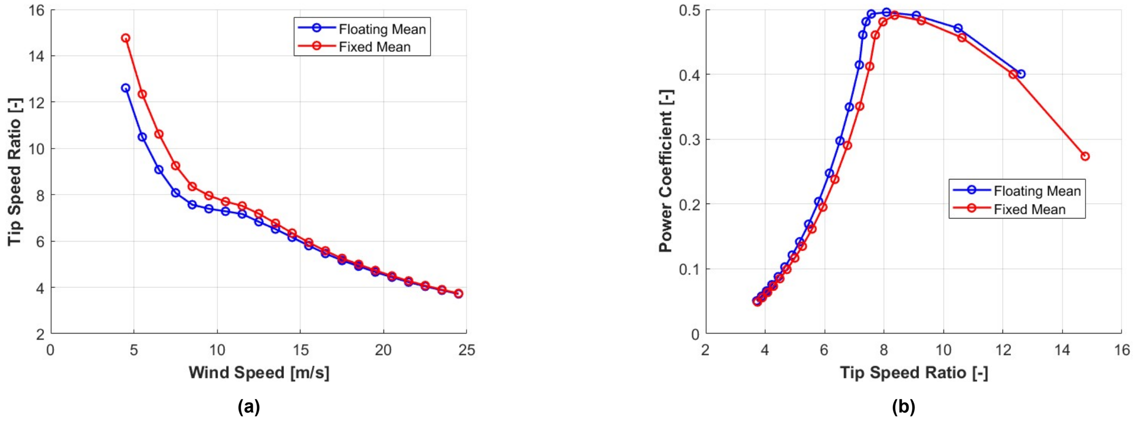

(a) (b)

Figure 5.20: Realistic case: Mean (a) Tip speed ratio and (b) power coefficient

5.2. RUL and Damage

5.2.1. RUL

In the previous sections, the various loads experienced by the upwind main bearing of the two WT configurations, as well as how they are affected by the platform motions in the case of the FOWT, were presented. Moreover, the differences in aerodynamic performance between the FOWT and the BOWT were examined, with a focus on the rotor speed, the TSR and the power coefficient of the two WT configurations during their operation. The next step in the methodology, as also demonstrated in Figure 3.1, is to investigate how the examined loads and characteristics of the WTs affect the damage of MBs and to analyze damage accumulation and RUL over time. In Subsection 3.6.3, it was explained in detail how the accumulated damage and RUL of the MBs was calculated over the 20-year design life.

The RUL of MB1 and MB2 of the FOWT and BOWT over time on a time horizon of 20 years is illustrated in Figure 5.21 for the realistic case. The RUL degradations of the two MBs for the aligned wind-wave cases are very similar to those of the realistic cases. Therefore, their plots are provided in Appendix C, while only the corresponding values are mentioned here for comparison.

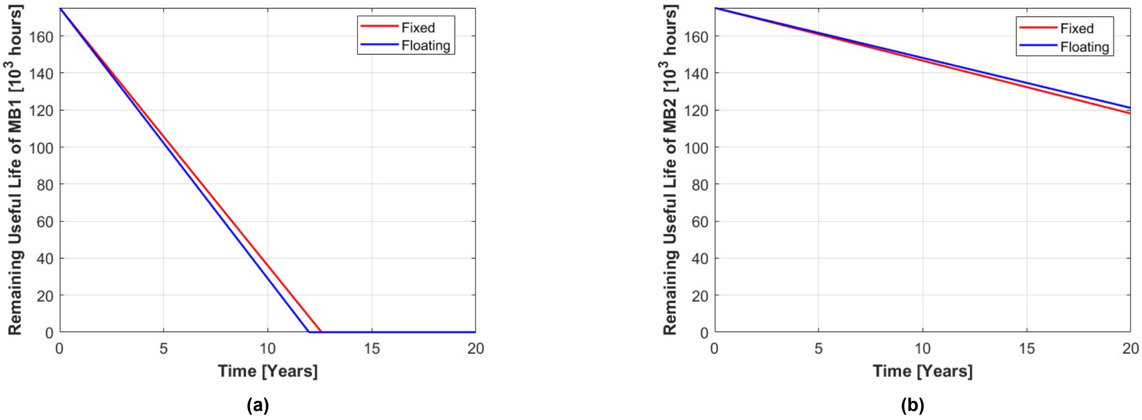

Figure 5.21: Realistic case: Remaining Useful Life degradation of (a) MB1 and (b) MB2 over time

From Figure 5.21a, it is clear that the upwind main bearing, in both WT configurations, fails before the period of 20 years. Specifically, MB1 fails earlier for the FOWT, after 11.98 years, compared to the counterpart for the BOWT, which fails after 12.58 years, for the realistic cases. In contrast, the downwind main bearing does not fail within the 20-year design life for either of the two WT configurations. More specifically, according to the results of the simulations, after 20 years, the RUL of MB2 is estimated to be 13.48 years for the BOWT and 13.83 years for the FOWT. This suggests that MB2 accumulates slightly higher fatigue damage for the BOWT than the FOWT. However, this observation is not investigated further in this thesis, as the focus remains on MB1, which is expected to reach the end of its design life before the 20-year period.

In the aligned wind-wave cases, MB1 fails after 12.02 years for the FOWT and 12.62 years for the BOWT, lasting for 0.3% more years in both WT configurations. This indicates that the misalignment of wind and waves between wind speeds of 11.5 and 17.5 m/s (as shown in Table 4.5) has a negligible effect on the fatigue damage of the upwind main bearing. Similarly, MB2, after the end of the design life in the aligned cases, has a RUL of 13.49 years for the BOWT (0.07% higher than the realistic case) and 13.91 years for the FOWT (0.6% increase with respect to the realistic case). The RUL values of MB1 and MB2 for both realistic and aligned cases are summarized in Table 5.2.

The RUL reduction is represented by a straight line, because in the applied methodology, the hourly simulations are extrapolated to 20 years. That means that exactly the same loads, turbulent conditions and wind speed probabilities, included in the hourly simulations performed, are considered iteratively over the 20-year lifetime, as shown in Equation 3.40. However, it is a limitation due to the absence of real data, as in real conditions, the conditions and loading of the WT can change over the period of 20 years.

5.2.2. Damage results

As expected, the cumulative damage of the two main bearings for both the FOWT and BOWT rises linearly over the 20-year period, following a trend inversely proportional to the RUL. For the realistic case, the cumulative fatigue damage of the two main bearings is shown in Figure 5.22, while again the respective results for the aligned cases are of similar magnitude and omitted for conciseness.

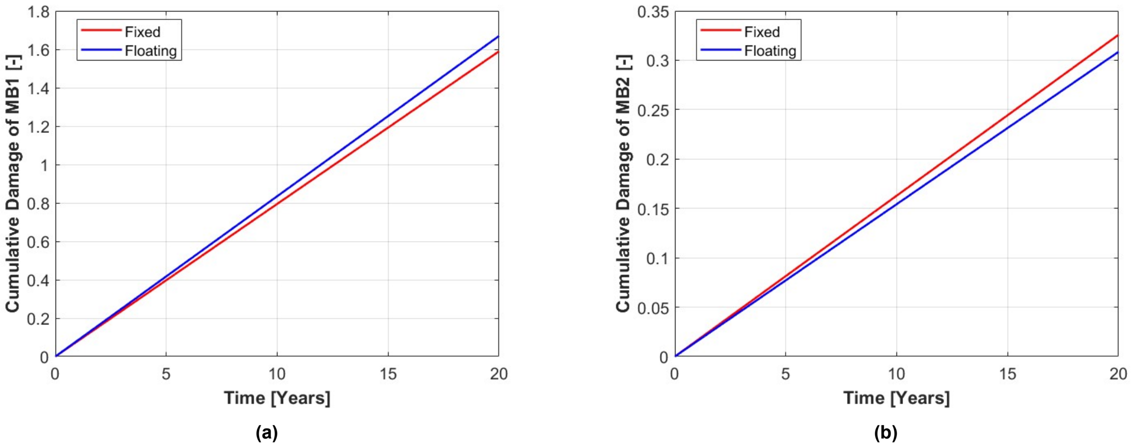

Figure 5.22: Realistic case: Cumulative damage of (a) MB1 and (b) MB2 over time

While values of damage higher than 1 do not make sense physically, since the main bearings fail when damage equals 1, they are shown as a comparative measure of the total damage after 20 years. As shown in Figure 5.22a, in the end of the 20 years, the cumulative damage of MB1 of the FOWT is almost 5% higher than that of the BOWT. Regarding MB2, as shown in Figure 5.22b, the 20-year accumulated damage for the FOWT is almost 6% lower than its counterpart for the BOWT.

For the aligned wind-wave cases, the 20-year cumulative damage of MB1 is 0.6% lower than the realistic cases in both WT types. For MB2, the total 20-year damage over 20 years for the FOWT is 3.2% lower than the realistic cases, while for the BOWT, it is almost identical. The cumulative damage values of MB1 and MB2 for both realistic and aligned cases are summarized in Table 5.3.

Having established that MB1 fails within the 20-year WT design life, the analysis now examines how this damage accumulates across different wind speeds and operating regions. First, it is essential to review the underlying mechanisms that affect the main bearing fatigue damage. Specifically, MB fatigue damage depends on the dynamic equivalent load P (as shown in Equation 3.37 and Equation 3.39), the rotational speed of the rotor (shown in Equation 3.34 to Equation 3.39) and the wind speed probability (Equation 3.39). Since the first two factors have already been analyzed in Section 5.1, the Weibull distribution considered for the installation site of the WTs for this project, is shown in Figure 5.23, along with the most probable wind speeds.

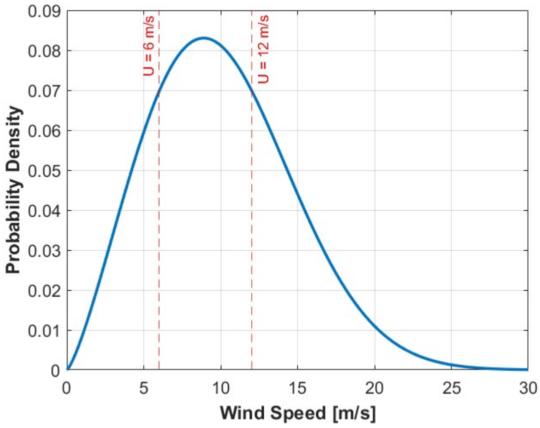

Figure 5.23: Weibull distribution and most probable wind speeds for the selected site

As seen in Figure 5.23, the most probable wind speeds are found between 6 and 12 m/s, so mostly in the below-rated region. Next, in Figure 5.24a, the 20-year cumulative damage of MB1 per wind speed region is illustrated for both FOWT and BOWT, while in Figure 5.24b, the normalized 20-year cumulative damage of MB1 per operating region is shown, as a percentage of the total occurred damage. As shown in the left plot, the cumulative damage distribution for MB1 across wind speeds exhibits a pattern consistent with the regional Weibull wind speed distribution.

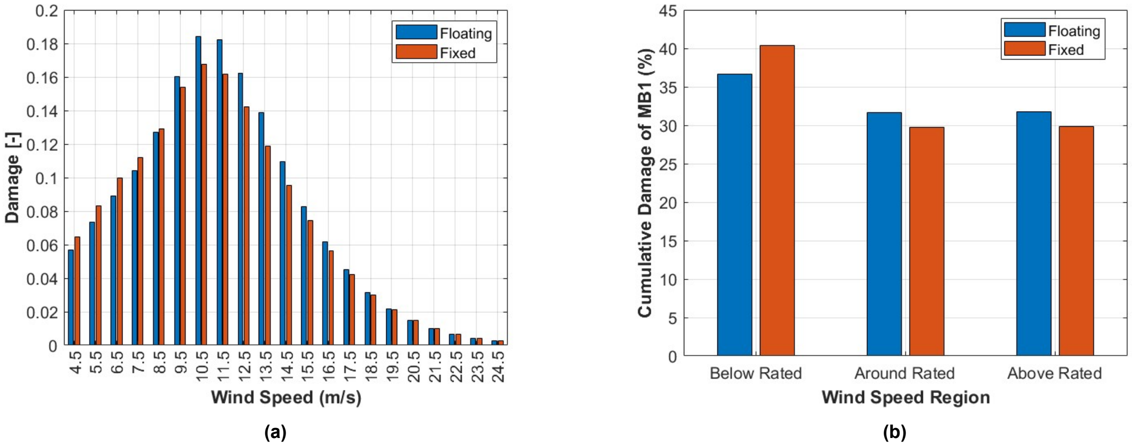

Figure 5.24: Realistic case: MB1 20-year (a) cumulative damage per wind speed and (b) normalized cumulative damage per operating region

An interesting observation is that MB1 experiences higher damage for the BOWT than for the FOWT at wind speeds below 8.5 m/s. This is because the mean dynamic equivalent load is very close between the two WTs in this range, as shown in Figure 5.4a. In the same wind speed range, the rotor speed and in turn the load cycles, are higher for the BOWT, as seen in Figure 5.18. These effects, which are also seen in the LDD histogram, (for instance, at 7.5 m/s, depicted in Figure 5.1a) explain the higher MB1 fatigue damage for the BOWT in the low-wind regime.

Above 8.5 m/s, the trend is reverse, the rotor speed deviation between the two turbines decreases, while the mean dynamic equivalent load becomes higher for the FOWT. This results in greater MB1 fatigue damage for the FOWT in the high-wind regime. The highest contribution to the MB1 fatigue damage occurs at 10.5 m/s and 11.5 m/s, where the MB1 damage for the FOWT exceeds that of the BOWT by 9.8% and 12.5%, respectively.

In Figure 5.24b, it can be observed that the below-rated region has the highest share in the 20-year damage of MB1 for both BOWT and FOWT, making up for 40.4% and 36.6% of the overall 20-year damage respectively. This results demonstrates the impact of the higher Weibull probability for the below-rated wind speeds. As anticipated, for the around-rated and above-rated region (including the wind speeds 10.5 - 12.5 m/s), the FOWT has a higher MB1 cumulative damage than the BOWT by 1.7% and 2%, respectively.

5.2.3. RUL and Damage Results Summary

This section summarizes the results of the RUL and the cumulative fatigue damage of the two MBs for the FOWT and BOWT configurations. Specifically, Table 5.2 presents the failure time of MB1 and the RUL of MB2 after the 20-year design life for both realistic and aligned wind–wave cases. The most significant finding is that MB1 fails during the 20-year design life for both WT configurations, with FOWT showing 4.77% shorter life than BOWT in realistic cases. In the aligned wind-wave cases, MB1 life is extended by approximately 0.3% for both WTs compared to the realistic cases, while FOWT MB1 fails 4.75% earlier than BOWT.

Table 5.3 shows the total accumulated damage of MB1 and MB2 over 20 years. FOWT experiences 5.03% higher MB1 fatigue damage than BOWT in the realistic cases, while the aligned wind-wave cases show a corresponding increase of 5.06%.

Table 5.2: Remaining Useful Life (RUL) of Main Bearings under Different Scenarios

Case	FOWT	BOWT	Diff. (%)
MB1 – Upwind Main Bearing (Failure Time)			
Realistic	11.98 yrs	12.58 yrs	-4.77%
Aligned Wind-Wave	12.02 yrs	12.62 yrs	-4.75%
MB2 – Downwind Main Bearing (RUL after 20 years)			
Realistic	13.83 yrs	13.48 yrs	+2.60%
Aligned Wind-Wave	13.91 yrs	13.49 yrs	+3.11%

Table 5.3: Total Cumulative Damage over 20 Years for Main Bearings

Case	FOWT	BOWT	Diff. (%)
MB1 – Upwind Main Bearing			
Realistic	1.67	1.59	+5.03%
Aligned Wind-Wave	1.66	1.58	+5.06%
MB2 – Downwind Main Bearing			
Realistic	0.31	0.33	-6.06%
Aligned Wind-Wave	0.30	0.33	-9.09%

5.3. Parametric Damage analysis

Following the analysis of the accumulation of fatigue damage in MB1 and its driving factors, a parametric analysis with respect to various environmental and system parameters is presented in this section for the realistic cases. The aim of this sensitivity study, is to identify the environmental conditions and the intrinsic system parameters with the highest impact on the fatigue damage of MB1 for FOWTs and BOWTs. Due to the time limitation of this project, this sensitivity analysis was not performed for all the operating wind speeds. Instead, six characteristic wind speeds were selected, which are mentioned in Table 5.4, along with the reasoning for their selection: two wind speeds in the below-rated region, the rated wind speed and three wind speeds in the above-rated region.

Table 5.4: Justification of selected wind speeds for parametric sensitivity analysis

Wind Speed (m/s)	Reasoning
8.5	Most probable wind speed, in the below-rated region characterized by variable rotor speed and maximum power tracking.
10.5	Approaches the transition to rated operation with increasing loads.
11.5	Transition to rated operation, marking the change in control strategy from torque control to blade pitch control.
13.5	Operation under active pitch control, highlighting main bearing behavior under full-load conditions.
16.5	Higher wind speed in the above-rated region with stronger pitch regulation.
23.5	Very high wind speed close to the cut-out threshold, evaluating main bearing loading under extreme wind conditions.

Moreover, it must be emphasized that the environmental and system parameter variations may not correspond to realistic design of a wind turbine. Regarding the intrinsic characteristics of the BOWT and the FOWT, they are already optimized in the baseline models to minimize operational loads on the various components and ensure efficient and optimal system behavior and operation. Therefore, the purpose of this sensitivity analysis is exploratory and comparative, aiming at detecting the most influential characteristics affecting MB1 fatigue damage, rather than developing new real-world designs, since such designs would require further structural verifications in the time- and frequency- domain.

More precisely, two environmental parameters and three intrinsic system parameters were tested with a $\pm20\%$ change in each parameter. This percentage change was selected to ensure that there will be some notable impact on the results, since as also mentioned above, it is not intended to suggest a new design. However, it was checked that the system of FOWT and BOWT remains stable even after this change. The parametric changes considered for the parametric tests are briefly described in Table 5.5.

Table 5.5: Overview of Parametric Tests: Environmental and System Parameters

Category	Parameter	Description
Environmental	$H_s - T_p$ ±20%	Determines wave energy and frequency content, affects hydrodynamic loading, and platform motion
	Turbulence Intensity (Class B-C)	Represents wind field variability
System (Intrinsic)	Nacelle Mass ±20%	Alters tower-top mass and inertia
	Platform Mass ±20%	Influences platform motion, impacts wave-induced platform dynamics
	Mooring Line Stiffness ±20%	Affects platform motion response and potential drivetrain and tower coupling

A separate simulation was performed for each individual change. Once all of the simulations with the new parameters were completed, the various loads, motions and the new overall cumulative damage for the six examined wind speeds were compared with the quantities of the original simulations presented up to now. The effect of each change on the total MB1 damage for the six wind speeds is noted in Table 5.6, with respect to the original case. The variation in damage pertains only to the six investigated characteristic wind speeds, to gain a relative understanding of how each parameter impacts the damage of the main bearing. This means that if parameter changes are also implemented in the remaining wind speeds, the new total damage obtained could deviate even more from the damage initially calculated. In the relevant table, “Change 1” refers to the first change for every parameter (class B for turbulent intensity or +20% for other parameters), while “Change 2” refers to the second change (class C for turbulent intensity or - 20% for other conditions).

Table 5.6: Effect of Environmental and System Parameters on MB1 Fatigue Damage (% change with respect to the original case)

Parameter	Type	FOWT		BOWT	
		Change 1	Change 2	Change 1	Change 2
$H_s - T_p$ (± 20%)	Environmental	+0.04%	+0.02%	-0.08%	+0.03%
Turbulence Intensity (Class A $\rightarrow$ B|C)	Environmental	-3.92%	-8.07%	-5.27%	-9.92%
Nacelle Mass (± 20%)	System	+1.30%	-0.96%	+0.08%	+0.06%
Platform Mass (± 20%)	System	-5.65%	+4.45%	–	–
Mooring Stiffness (± 20%)	System	+0.03%	+0.17%	–	–

According to Table 5.6, the highest impact on the damage of MB1 caused by the six wind speeds results from the change in turbulent intensity. In the original cases and the selected location, the turbulence intensity of Class A has been considered. Thus, as the turbulence intensity decreases to class B and class C, the MB1 damage is reduced even more, as expected due to lower variability in aerodynamic loads. Another interesting result is that the impact is more intense on the BOWT than on the FOWT. In the BOWT, the damage is reduced by 5.27 and 9.92% for the turbulence classes B and C, accordingly, compared to 3.92 and 8.07% for the FOWT, respectively. This can be attributed to the fact that in the case of the BOWT, wind fluctuations directly influence the drivetrain and the main bearings. In contrast, in the FOWT, there is a coupled behavior between the drivetrain, tower and platform, thus, the effect of the lower turbulence is redistributed between the drivetrain and the platform or partially absorbed by the platform. Consequently, the main bearing of the FOWT is slightly less sensitive to turbulence changes.

Moreover, for the FOWT, among the intrinsic system parameters, the change in platform mass has the most considerable effect on the damage of the MB1. When the platform mass is increased by 20%, the MB1 damage (of the six wind speeds) reduces by 5.65%, while when the platform mass is reduced by 20%, the damage rises by 4.45%. This is related to the motions of the platform, since a lighter semi-submersible platform is anticipated to be subjected in more intense motions, that deteriorate the loads and the damage of the main bearings, as shown in Subsection 5.1.2.

Regarding the remaining parameters, the nacelle mass change induces a higher effect in the damage of MB1 for the FOWT than the BOWT, since the change in tower-top inertia and mass has an additional effect on the platform motion (higher nacelle mass leads to higher pitch platform motions and greater MB1 damage, while a lighter nacelle mitigates this effect). In contrast, in the BOWT, which is fixed in the seabed, the different nacelle mass has a negligible effect.

Next, the variation in mooring line stiffness leads to a very small change in MB1 damage. In particular, MB1 damage is increased for both higher and lower mooring line stiffness. This occurs because the mooring line system in the baseline model is already tuned. As a result, a lower mooring line stiffness could result in higher platform motions and damage of MB1, whereas higher mooring line stiffness could over constrain the platform, causing the transmission of vibrations to the platform, tower and the nacelle. Finally, the change in H_s and T_p has a very small effect on both FOWTs and BOWTs. Since T_p directly affects the wave frequency, to interpret their effect in detail, the wave frequencies should be thoroughly examined with respect to the natural frequencies of the platform and the tower to identify potential resonance. However, since their observed effect is minimal, this correlation is not investigated further in this sensitivity analysis.

Then, Figure 5.25 shows the mean and standard deviations of the dynamic equivalent load of MB1, across the six selected wind speeds and some parametric tests, in which the effect is more visible.

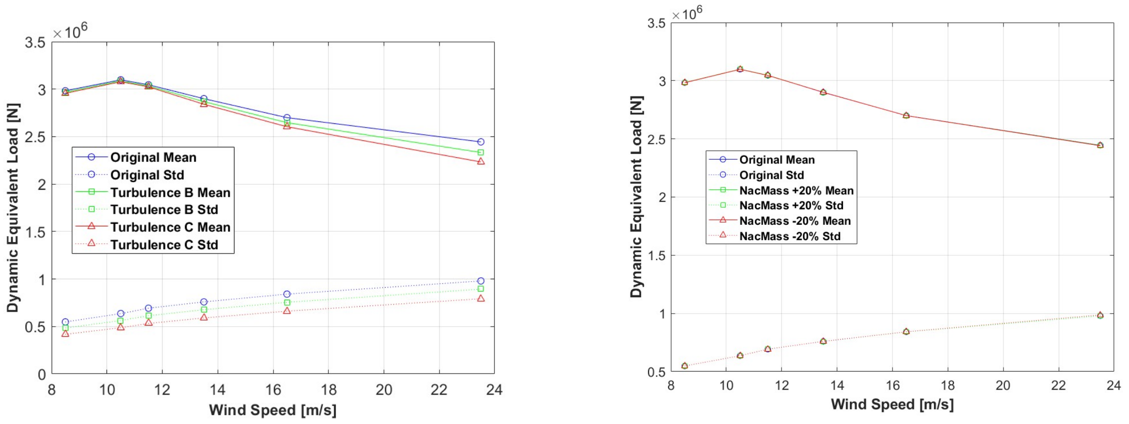

(a) BOWT - turbulence class change

(b) BOWT - nacelle mass change

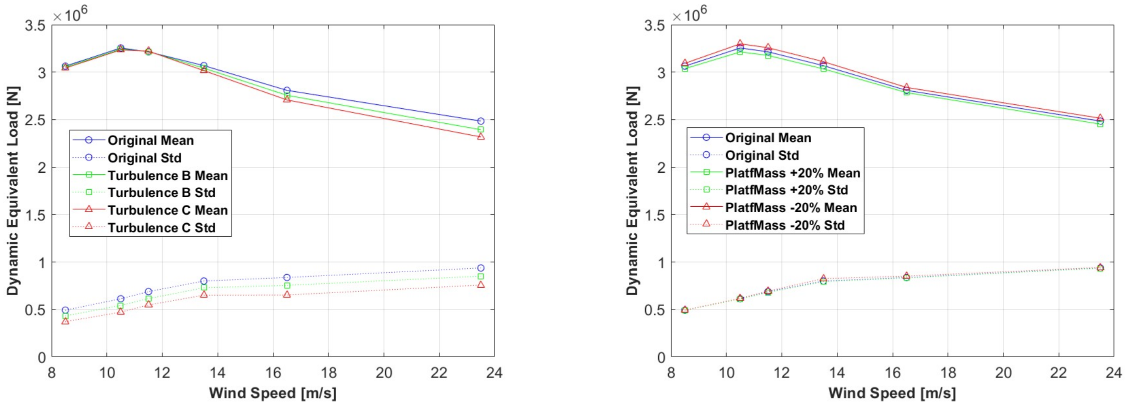

(c) FOWT - turbulence class change

(d) FOWT - platform mass change

Figure 5.25: Dynamic equivalent load variation for indicative parametric tests of BOWT and FOWT

The impact of the turbulence effect is clearer at higher wind speeds in the above rated region as shown in Figure 5.25a and Figure 5.25c, where a lower turbulence class yields lower P mean value and standard deviation. With respect to the platform mass, its effect is visible across all wind speeds in Figure 5.25d. Lower platform mass leads to higher P load, although the standard deviation remains almost constant for the different values of the platform mass. Nacelle mass, on the other hand, has a minor impact on the dynamic equivalent load of the MB1 in the case of BOWT as can be seen in Figure 5.25b.

Moreover, a few indicative changes of the platform motions are illustrated in Figure 5.26 for the most influential parametric variations, to further show how the platform motion affects the MB1 damage.

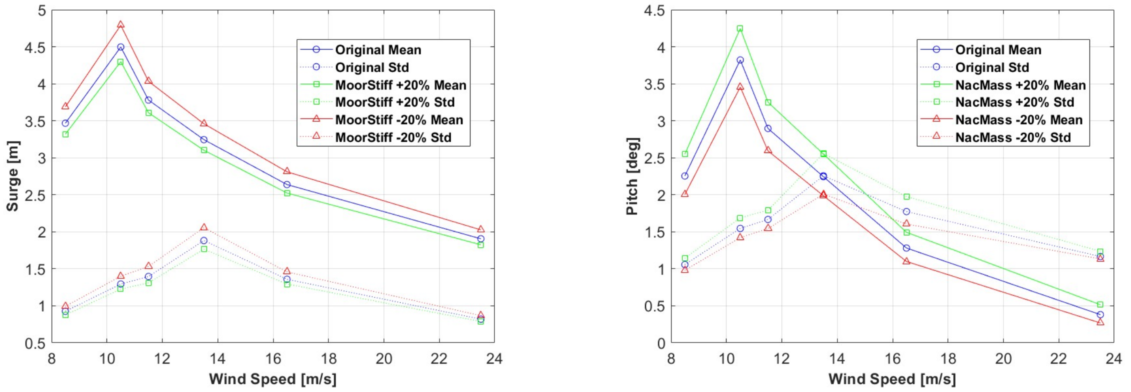

(a) Surge platform motion: mooring line stiffness change

(b) Pitch platform motion: nacelle mass change

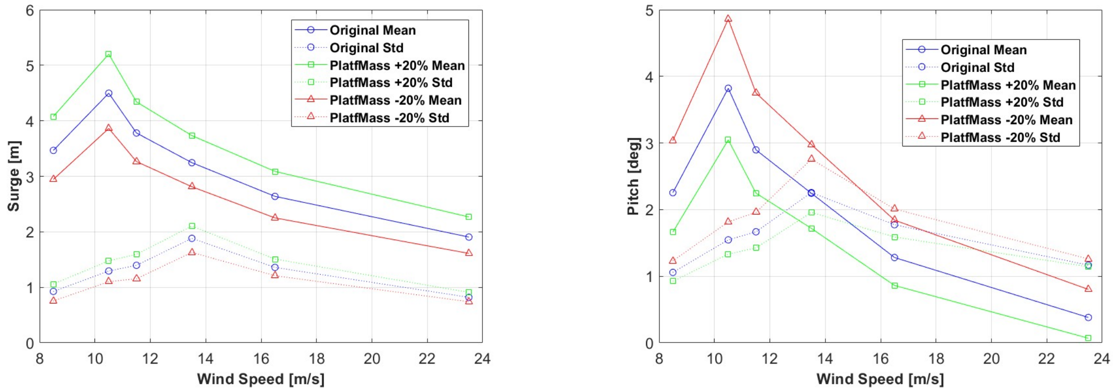

(c) Surge platform motion: platform mass change

(d) Pitch platform motion: platform mass change

Figure 5.26: Platform motion variations for indicative parametric tests of FOWT

According to Figure 5.26a, less mooring line stiffness leads to higher mean value and standard deviations of the surge motion, since the platform moves more freely. Figure 5.26b proves that a heavier nacelle increases the pitch motion of the platform by creating higher gravitational loads and relevant moments. Finally, a higher platform mass results in a more intense surge motion but less intense pitch motion of the platform, as illustrated in Figure 5.26c and Figure 5.26d, accordingly.

In addition to the dynamic equivalent load magnitudes, the MB1 axial-to-radial load ratio is also evaluated to gain a better understanding of how parametric changes affect the internal load distribution. This ratio demonstrates how the axial load contributes versus the radial one to the total load of the main bearing. Changes in the balance can potentially affect the dynamics and the MB1 fatigue life. In Table 5.7 and Table 5.8, the load ratio for each parametric variation is mentioned for the BOWT and FOWT, respectively, as an absolute value and a difference in% from the baseline load ratio, which is equal to 0.2527 for the BOWT and 0.268686 for the FOWT. The column “New Ratio” indicates the MB1 axial-to-radial load ratio, obtained for each parametric change.

Table 5.7: MB1 Axial-to-Radial Load Ratio Change for BOWT

Parameter Change	New Ratio	Difference (%)
TI (A → B)	0.2598	+2.98%
TI (A → C)	0.2665	+5.77%
Nacelle Mass +20%	0.2529	+0.10%
Nacelle Mass –20%	0.2525	-0.07%
$H_s - T_p$ +20%	0.2528	+0.07%
$H_s - T_p$ –20%	0.2526	–0.05%

Table 5.8: Axial to Radial Load Ratio Changes for MB1 and FOWT

Parameter Change	New Ratio	Difference (%)
TI (A → B)	0.2759	+2.71%
TI (A → C)	0.2818	+4.98%
Platform Mass +20%	0.2656	-1.13%
Platform Mass –20%	0.2735	+1.81%
Nacelle Mass +20%	0.2721	+1.31%
Nacelle Mass –20%	0.2657	-1.14%
Mooring Line Stiffness +20%	0.268696	+0.0029%
Mooring Line Stiffness –20%	0.268668	-0.0038%
$H_s - T_p$ +20%	0.268581	-0.04%
$H_s - T_p$ –20%	0.268745	+0.02%

By comparing Table 5.7 and Table 5.8 with Table 5.6, a few conclusions can be drawn, which are briefly mentioned below:

- Lower turbulence intensity reduces the radial load fluctuations, due to more stable aerodynamic inflow, leading to higher axial-to-load ratio and lower fatigue damage of the MB.
- A lighter platform shows a higher pitch motion, which amplifies the axial load contribution and increases the fatigue damage.
- Nacelle mass shows a correlation for the FOWT. Specifically, a heavier nacelle results in a higher axial load and higher fatigue damage. For the BOWT, the nacelle mass has an insignificant effect and does not show an explicit correlation between the axial-to-radial load ratio and the damage of the MB.
- Akin to the nacelle mass in the case of the BOWT, the variation of $H_s - T_p$ and mooring line stiffness demonstrates a negligible effect on the axial-to-radial load ratio, thus, no meaningful relationship can be extracted between that ratio and the fatigue damage of MB1.

6

Discussion

In this chapter, a connection between the results, previously elaborated separately, is presented, while the key points of the results are highlighted and further discussed. Specifically, in Section 6.1, a short overview of the impact of the platform motions on the loads of the main bearing is provided, followed by Section 6.2, where the shares of the axial and radial loads on the dynamic equivalent load and the damage of the main bearing are analyzed. Then, Section 6.3 explains the behavior of the controller and its limitations in the FOWT, while Section 6.4 compares the final results of this thesis against relevant findings from the literature. Lastly, in Section 6.5, the implications of this thesis on socio-economical and system-integration context are outlined.

6.1. Impact of Platform Motions

As explained in Subsection 5.1.2, the upwind main bearing of the FOWT experiences mostly higher loads, across the operating wind speeds. These are affected and mainly amplified by the platform motion, which was analyzed in Subsection 5.1.2. In Figure 6.1, the relation of the different platform motions with the respective loads is briefly illustrated. The different colors of the lines are used to distinguish the effect of the different motions on a specific load. To adduce a specific example, the green line arrows represent the motions of the platform that influence the lateral load F_1^y of MB1, whereas the blue line arrows denote the platform motions affecting the vertical load F_1^z of MB1.

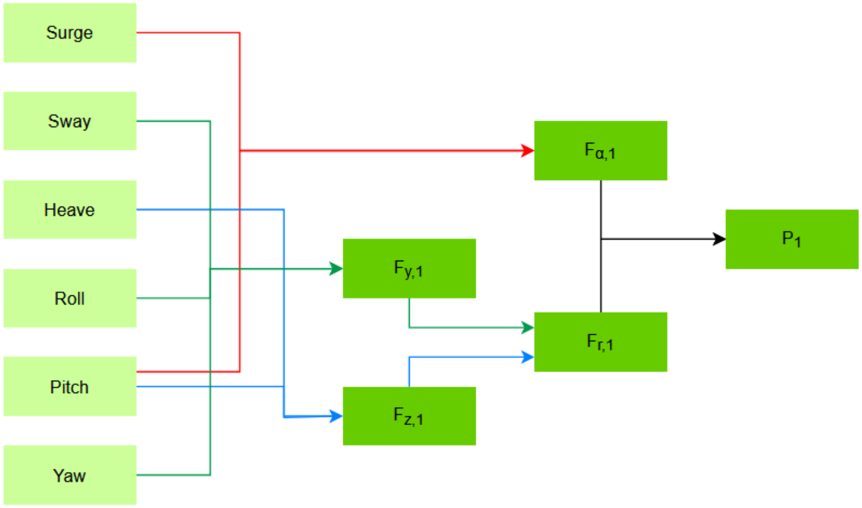

Figure 6.1: Overview of key connections between the platform motions and the loads on the MB1

In short, firstly, it was explained that the positive surge and pitch motion of the platform raises the thrust force of the rotor of the FOWT, which in turn causes a higher axial force on the MB1 of the FOWT. Heave and pitch motion lower the vertical force F_h^z and the moment M_h^y of the rotor-hub respectively, and in turn slightly increase the vertical load of MB1 F_1^z, since the aforementioned loads are related through Equation 3.22. Finally, sway, yaw and roll motion strongly affect the rotor skew angle of the rotor and subsequently the lateral loads of the rotor F_h^y and M_h^z. In the FOWT, these loads have a higher magnitude at higher wind speeds, compared to the BOWT. This change increases the variability of the lateral load F_1^y of MB1 of the FOWT, making it higher at wind speeds around the rated one or with a different sign at higher wind speeds close to the cut-out value.

6.2. Axial and Radial Load Shares

In the previous chapter, the radial and axial loads of MB1 were analyzed and it was shown that radial loads are higher than axial loads in the DTU 10 MW drivetrain configuration with two locating main bearings. Notably, it would be of interest to see how the ratio and the contribution of these loads to the dynamic equivalent load change per wind speed and wind turbine category. For the former, the axial to radial load ratio (for realistic cases) is shown in the bar plot of Figure 6.2. For the latter, the bar plots of Figure 6.3 are used, which, apart from the values of axial and radial load, also consider the effect of the dynamic radial and axial load factor X and Y respectively (Table 3.2).

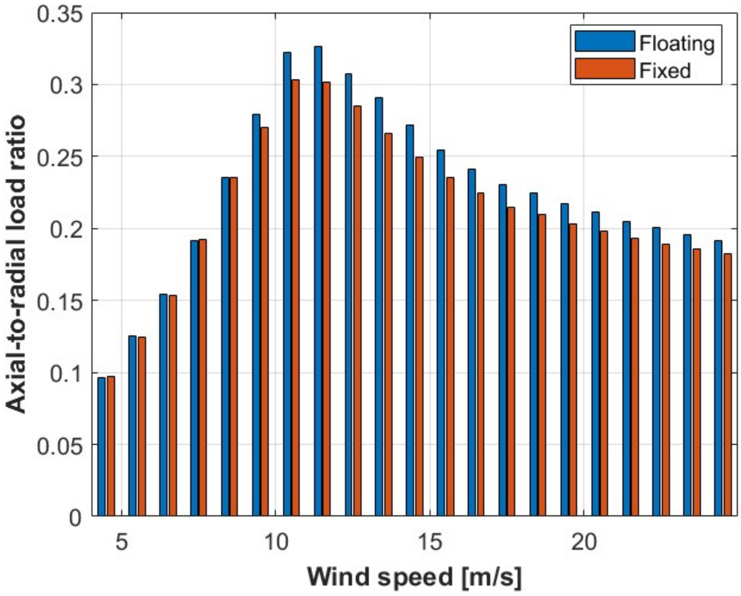

Figure 6.2: Realistic case: Axial-to-radial load ratio for FOWT and BOWT as a function of wind speed

Regarding the axial-to-radial load ratio, according to Figure 6.2, for both the FOWT and BOWT, it is less than one in the full operating wind speed range, meaning that the radial load is higher than the axial load. The ratio increases up to the rated wind speed of 11.4 m/s and then starts decreasing after the activation of blade pitch control, following the variation of the MB1 axial load and thrust force as shown in Figure 5.7a and Figure 5.7b, respectively.

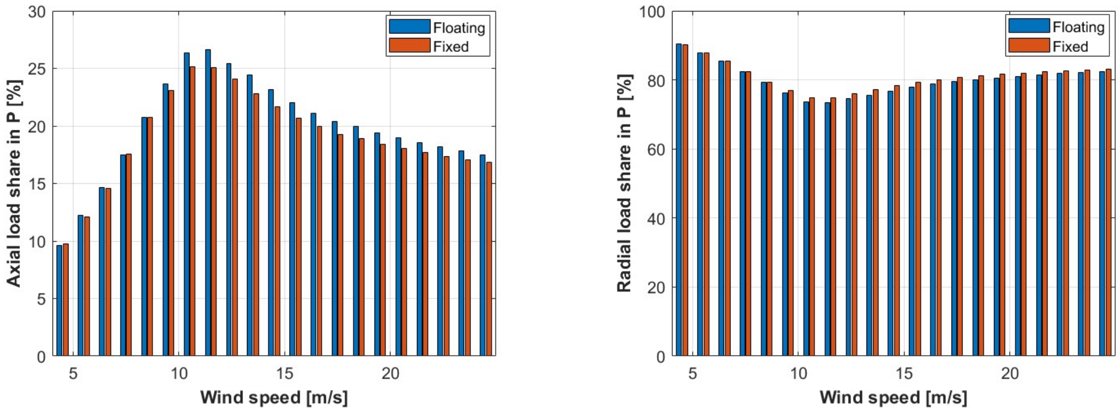

(a)

(b)

Figure 6.3: Realistic case: (a) Axial and (b) radial load share in the dynamic equivalent load P as a function of wind speed

Next, from Figure 6.3a and Figure 6.3b, it is clear that the radial load has a significantly higher contribution to the dynamic equivalent load P of the MB. As shown in Figure 6.3b, the mean radial load makes up even for 90.4% and 90.2% of the dynamic equivalent load for the FOWT and BOWT, accordingly, at 4.5 m/s.

However, as shown in Equation 3.37 and Equation 3.39, the relationship of the dynamic equivalent load (thus of the axial and radial load) to the damage of the main bearing is nonlinear due to the exponent m = 10/3 for the roller bearings according to ISO: 281: 2007 [68]. Therefore, the contribution of the radial and axial load to the damage of MB1 is illustrated in Figure 6.4.

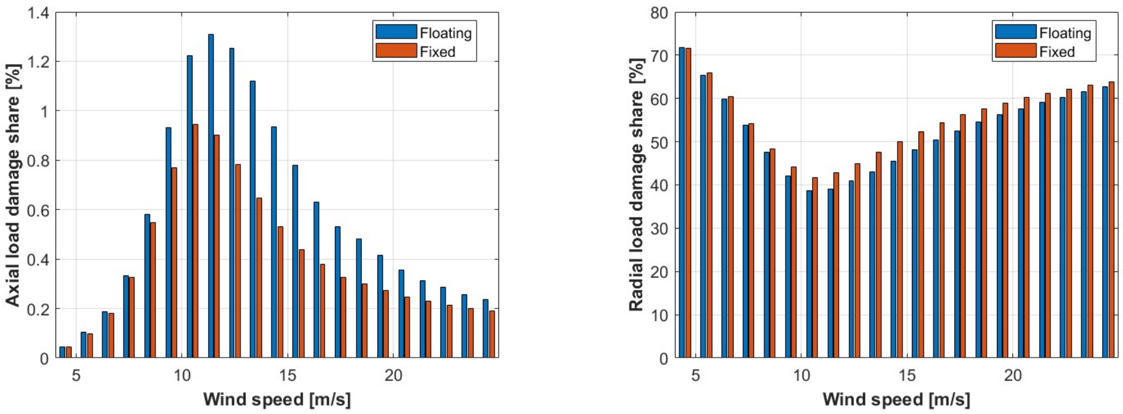

(a) Axial load share in the damage of MB1 as a function of wind speed

(b) Radial load share in the damage of MB1 as a function of wind speed

Figure 6.4: Realistic case: (a) Axial and (b) radial load share in the damage of MB1 as a function of wind speed (realistic cases)

Radial load is shown to contribute to MB1 damage for the FOWT from 38.7% (at 10.5 m/s) to 71.8% (at 4.5 m/s), while for the BOWT from 41.8% (at 10.5 m/s) to 71.6% (at 4.5 m/s). Axial load, on the other hand, contributes to the damage of MB1 from 0.05% (at 4.5 m/s) to 1.3% (at 11.5 m/s) for the FOWT, while for the BOWT its contribution ranges from 0.05% (at 4.5 m/s) to 0.9% (at 10.5 m/s). It should be highlighted that the sum of the contribution of the radial and axial load to the damage of MB1 is not 100%, due to the nonlinear nature of the relationship between P and damage and the fact that the rotational speed of the rotor also affect the load cycles and subsequently, the damage of the main bearing.

6.3. Controller Behavior

As already analyzed in Subsection 5.1.4, the mean generator power of the FOWT and the rotor speed (Figure 5.18) are lower than that of the BOWT in the first above-rated wind speeds. The mean value of the generator power and its standard deviation are also shown in Figure 6.5, where it is visible that from approximately 10.5 to 14.5 m/s, the power of the FOWT has a lower mean value, but a higher standard deviation than that of the BOWT.

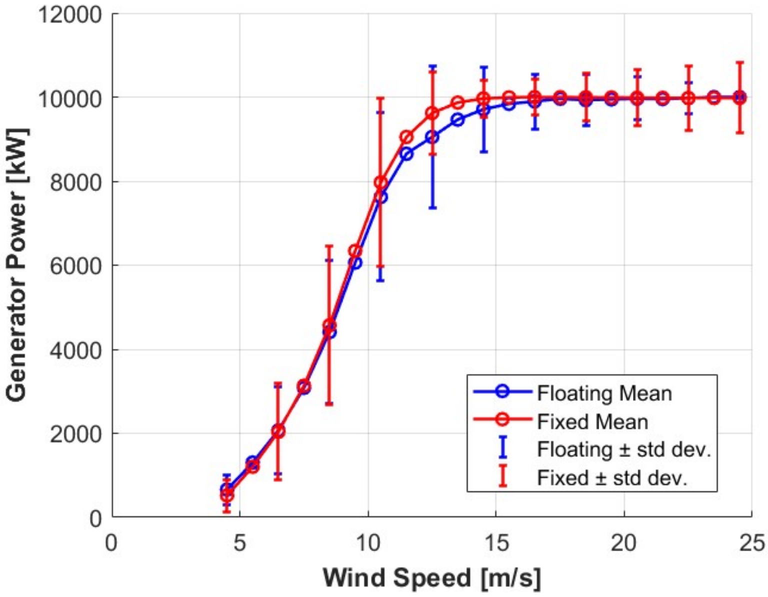

Figure 6.5: Realistic case: Generator Power, mean and standard deviation, as a function of wind speed

To understand the operation of the controller in that area, a step-analysis was performed, during which constant wind speeds (without turbulence) were selected between the cut-in and cut-out wind speed for a constant wind and wave direction. Specifically, starting from the cut-in wind speed of 4.5 m/s, the wind speed was increased gradually by 1 m/s every 200 s, leading to a total simulation of 4200 s, as shown in Figure 6.6.

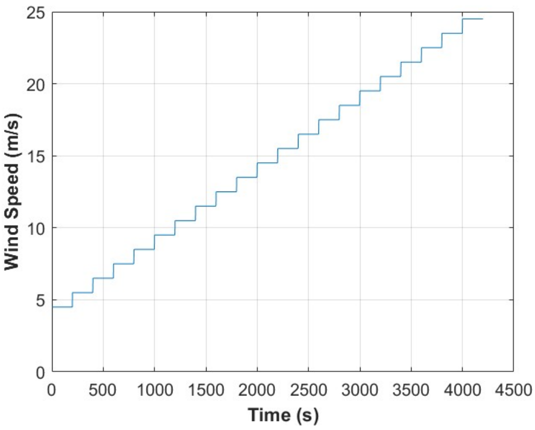

Figure 6.6: Realistic case: Constant wind speeds used in step-analysis, between cut-in and cut-out wind speeds

Then, some timeseries of the quantities of the floating wind turbine are analyzed to detect any possible abnormalities in the controller operation. Specifically, the rotor speed and the blade pitch angle are shown in Figure 6.7, while the rotor thrust of the FOWT is shown separately and compared to the value of BOWT in Figure 6.8.

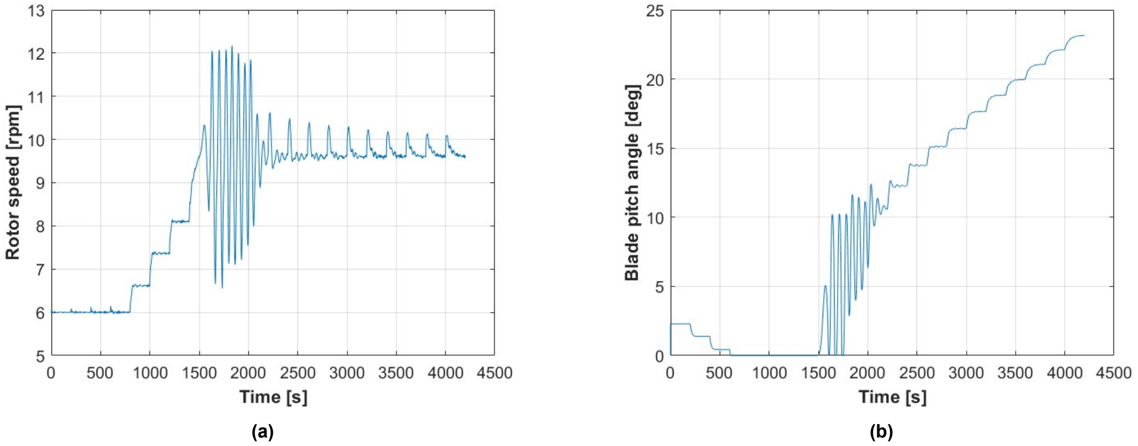

Figure 6.7: (a) Rotor speed and (b) blade pitch angle of FOWT in the step-analysis

An instability of the controller is observed between almost 1500 s and 2100 s, which correspond to the wind speeds 11.5 m/s to 14.5 m/s, as shown in Figure 6.6, and after that range, the controller continues working properly in steps, in the above-rated region. This instability arises from the coupling between the platform motion and the WT controller during the transition from operation at below-rated to above-rated wind speeds. Specifically, the controller struggles to distinguish between actual wind speed variations and apparent fluctuations caused by platform motion, which leads to inappropriate control responses.

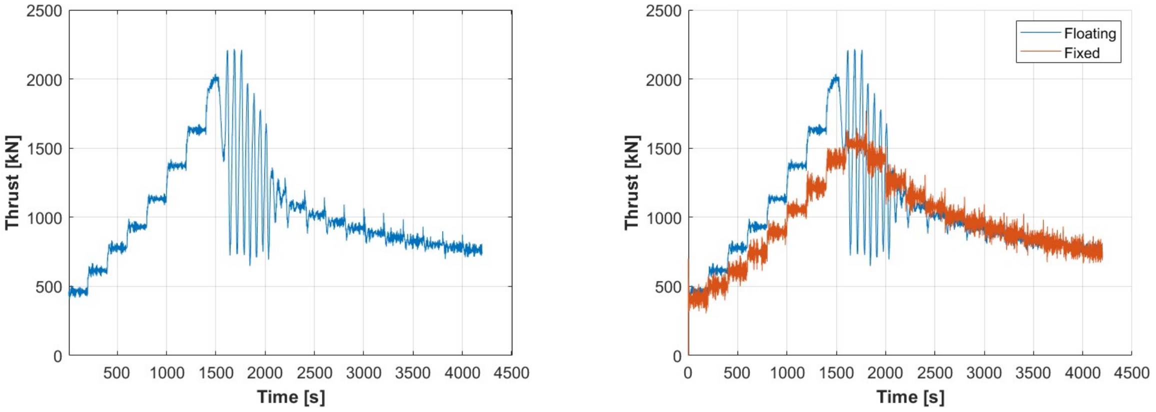

(a) Rotor thrust of FOWT in the step-analysis

(b) Rotor thrust of FOWT and BOWT in the step-analysis

Figure 6.8: Rotor thrust of FOWT and BOWT in the step-analysis

The same transient oscillations are noticed in the thrust load of the floating wind turbine, which is plotted against the rotor thrust of the bottom-fixed wind turbine in the step analysis. One could assume that this instability of the controller would significantly influence the loads and the fatigue damage of the main bearing, yet, its impact is twofold.

Firstly, between 11.5 and 14.5 m/s, this controller irregularity could plausibly lead to increased loads, such as the rotor thrust, and in turn loads of the MB. However, as explained in Subsection 5.1.2, it is the platform pitch and surge motion that amplify the thrust load and subsequently the axial load of the MB. Indeed, this is clearly confirmed in Figure 6.8b, where especially before 1500 s, when the controller is inactive (below-rated region) the FOWT presents notably higher thrust values than the BOWT.

Furthermore, in the region between 11.5 and 14.5 m/s, the rotor speed of the FOWT exhibits lower mean value (as shown in Figure 5.18), which could reduce the cycles counts and probably the damage of MB1 for these wind speeds. Therefore, for a more realistic modeling of the FOWT, an advanced control scheme should be used to account for and deal with these irregularities. References from the literature supporting this observation in the controller operation are provided in the following section.

6.4. Literature Validation

In this section, some literature references are offered that confirm the results of this thesis. Firstly, in this thesis the floating wind turbine shows higher loads and fatigue damage of the main bearing than the bottom-fixed counterpart. Wang et al. [120] support this in their work, where they found larger axial and radial loads on the main bearings of a spar floating turbine than a monopile configuration. As mentioned in Subsection 5.2.2, the cumulative damage of the upwind main bearing over 20 years is 1.59 for the realistic cases and 1.58 for the aligned wind-wave cases, whereas for the downwind main bearing, the respective value is 0.33 for both sets of simulations. The calculated cumulative damage values are comparable to those that Wang et al. [64] found in their work, for a DTU 10 MW monopile wind turbine installed at an offshore location in the Northern North Sea. Specifically, over a 20-year period, they calculated a total damage of 1.61 for the upwind main bearing and 0.27 for the downwind main bearing.

Moreover, in Subsection 5.2.1, according to the cited RUL results, the upwind main bearing is the one that fails, after 11.98 years for the semi-submersible FOWT and after 12.58 years for the monopile BOWT, respectively. Validation against field data is challenging due to limited publicly available information. For FOWTs, the only available case is from the Hywind Scotland floating wind farm, where the MBs of its five spar FOWTs were replaced after seven years of operation [121], almost 41% earlier than predicted in this thesis. However, this case involves a different FOWT category, with an unknown bearing configuration (one or two MBs), and it is unclear whether the MBs failed completely or were replaced preventively. Regarding broader WT categories, Hart et al. [122], using a mixed dataset of 7,707 onshore and offshore WTs (unspecified configuration), concluded that on average 10% of MBs would require replacement within 10.5 years, 12.5% to 20% earlier than the results of this thesis. The scarcity of publicly available configuration-specific main bearing failures is due to the confidentiality of such information and the relatively recent deployment of FOWT technology.

The publicly available ROSCO controller, designed for bottom-fixed and floating offshore wind turbines, as was described, was found to be unstable in the case of the FOWT, for the first wind speeds of the above-rated region. The observed irregularities have been discussed in the existing literature, that highlights how additional control challenges are introduced to FOWTs because of coupled dynamics. Hegazy et al. [123] underline that conventional blade pitch control in FOWTs, can add non-minimum phase dynamics, particularly due to rotor thrust and platform pitch coupling, leading to instability and limited effectiveness of the controller. Furthermore, Yu et al. [124] and Stockhouse et al. [125], highlight that conventional controllers of wind turbines, can result in insufficient generator speed regulation and drivetrain stresses, when directly adopted in FOWTs. These findings and those presented in Section 6.3 reveal that floating wind turbines demand appropriate advanced control strategies tailored to their dynamic coupled behavior, such as gain scheduling, multi-loop feedback or model predictive control, to ameliorate and optimize their operational stability [125], contrary to the bottom-fixed wind turbines, whose structural stability allows the usage of simplified conventional controllers.

6.5. System integration and socio-economic implications

This thesis provides an analytical comparison of main bearing fatigue loads and damage between FOWTs and BOWTs, which has significant socio-economic and system-integration relevance. As mentioned in the introduction, the necessity to shift to renewable energy sources and the saturation of onshore wind turbines, makes floating wind a promising solution for the future energy map, since it enables access to deep-sea wind resources in regions with limited shallow waters. However, this advantage comes with additional drivetrain complexity, especially in the main bearings, due to platform-induced motions such as surge and pitch.

The results of this thesis show clear differences between FOWTs and BOWTs in terms of main bearing loading and fatigue damage. While radial loads dominate in both WT configurations, the FOWT experiences higher mean axial and radial MB1 loads across the operating wind speed range due to platform-induced motions. Around the rated wind speed, platform surge and pitch motion amplify the axial loads, while pitch, sway, roll, and yaw increase radial loads, resulting in up to 13.17% higher axial loading and 5.83% higher dynamic equivalent loading compared to the BOWT. Over a 20-year design life, this corresponds to 5.03% more accumulated fatigue damage for the upwind main bearing of the FOWT, reducing its RUL by approximately seven months with respect to the BOWT.

From a system-integration perspective, the results underline that drivetrain and main bearing design for FOWTs must be approached holistically. Unlike BOWTs, where the main bearings loads are mainly influenced by tower and nacelle dynamics, in the case of FOWTs, the coupled response of platform, nacelle and control system has an important influence on the main bearing damage. Specifically, the performed parametric sensitivity analysis indicates that different parts, such as the nacelle mass and inertia, the platform mass and inertia or mooring lines stiffness, can have an impact on the MB1 damage of the FOWT. This suggests that for an efficient floating wind deployment, system-oriented design should be adopted, rather than designing individual components separately.

In practice, this could include developing control schemes tailored to floating platform dynamics. Controllers could use platform motion sensors to anticipate and counteract load peaks, enabling real-time load mitigation. Advanced controllers could also integrate the impact of the turbulence intensity and balance power production with drivetrain fatigue through intelligent pitch control during high-turbulence periods, potentially extending main bearing life.

Furthermore, since radial loads dominate in the MB1 dynamic equivalent load and fatigue damage, bearing manufacturers could prioritize radial over axial capacity in four-point support drivetrains, at least for the upwind main bearing. This approach could save costs by extending the bearing life and avoiding oversized bearings with unnecessary axial capacity.

From a socio-economic perspective, the findings of this thesis have explicit implications for the operational and financial challenges of wind. Main bearings represent a significant share of the O&M costs, and their replacement is more complex and costly in floating offshore wind turbines, where access is limited. The calculated MB1 failure times in this thesis could help offshore wind farm operators plan predictive maintenance schedules and replacement of the MBs. In doing so, they could reduce unplanned downtime costs, avoid unexpected failures and increase the offshore wind energy yield. Finally, improving main bearing reliability of offshore, and especially floating wind turbines, could help deploy FOWTs in regions, where sea depths do not allow the installation of BOWTs, such as the Mediterranean Sea.

In summary, while floating wind turbines introduce additional drivetrain challenges compared to bottom-fixed configurations, targeted design and control measures can significantly improve main bearing lifetime and reduce O&M costs, supporting large-scale offshore wind deployment.

7

Conclusions and Recommendations

In this chapter, the conclusions of this thesis and recommendations for future work are presented. Specifically, in Section 7.1, the research sub-questions are answered one by one, and eventually the main research question is addressed. Next, Section 7.2 presents some limitations of this research and recommendations for future work.

7.1. Conclusions

The four research sub-questions of this work are mentioned and answered below:

Sub-question 1:
How can the loads on the main bearings be estimated, and which loads have the greatest influence on the main bearings of floating and bottom-fixed offshore wind turbines?

In this thesis, the main bearing loads are calculated using OpenFAST simulations under the operating conditions of Design Load Case 1.2, following IEC-61400-3-1:2019 guidelines [53]. Post-processing is performed according to ISO 281:2007 [68], to compute the equivalent dynamic load, which combines the axial and radial load of the main bearing weighted by standard factors. The analysis uses the DTU 10 MW reference wind turbine drivetrain, which includes two locating main bearings. The upwind main bearing (MB1), which experiences the highest loads, is the focus of this thesis. The axial and radial load of the main bearing are derived from force and moment balances, using the outputs of rotor thrust, shaft forces and moments from OpenFAST, according to relevant literature, which can be found in detail in Subsection 3.6.1. Especially, for the axial direction, rotor thrust is distributed between the two main bearings, proportionally to their stiffness. Furthermore, radial load consists of the loads in the vertical z- direction and the transverse y- direction.

The results show that radial load has the highest contribution to the MB1 loading and damage in both the floating and bottom-fixed configurations. Particularly, radial load constitutes 74 to 90% of the dynamic equivalent load for the FOWT across all operating wind speeds of the realistic cases and 75 to 90% for the BOWT (as seen in Figure 6.3b). Regarding fatigue damage, for the FOWT, radial load contributes 39 to 72% of the cumulative damage of the MB1 over a 20-year lifetime, whereas for the BOWT, the corresponding range is 42 to 72% (as illustrated in Figure 6.4b).

Sub-question 2:
What is the impact of the platform motion in floating wind turbines on main bearing loading compared to the bottom-fixed configurations?

The semi-submersible platform of the FOWT moves freely with six degrees of freedom (DOFs), introducing dynamic motions that alter the wind inflow to the rotor and predominantly increase the loads on the MB1 compared to the BOWT. The primary motions that affect loading are pitch and surge, whose mean values are found positive for the load cases of this thesis. Physically, positive pitch motion means that the platform tilts the rotor upward, increasing the angle of attack of the blades, while positive surge motion means that the platform moves toward the heading direction of the wind, resulting in higher effective wind speed for the rotor. These combined effects increase the rotor thrust of the FOWT and subsequently the axial load of the MB1.

Additionally, this research proves that heave and pitch motion affect the forces and moments on the vertical axis z and increase the vertical load of the MB for the FOWT, as elaborated in Subsection 5.1.2. Finally, in the same section, it is analyzed how sway, yaw and roll motion of the platform influence the rotor skew angle (shown in Figure 5.15a) causing slight misalignment between the wind and the rotor and changing the lateral loads in the transverse direction y. Specifically, the FOWT exhibits a higher transverse load than the BOWT around the rated wind speed. However, at higher wind speeds, close to the cut-out value, this lateral load first becomes lower than BOWT and then reverses direction. Aligned wind-wave cases show deviation in the lateral motions of the platform, with respect to the realistic cases, but their influence on the damage of MB1, eventually, is inconsiderable.

Sub-question 3:
How can fatigue damage of main bearings be calculated and what are the primary factors driving it in both wind turbine configurations?

In this thesis, the fatigue damage of the main bearings is estimated using the Load Duration Distribution (LDD) method, to define the cycles and the bins of the dynamic equivalent loads, and the bearing basic rating life of the MB, according to ISO 281: 2007 [68], as defined in Subsection 3.6.2. Each bin is defined from simulation-produced time series and linked to the basic rating life of the bearing. Next, the Palmgren-Miner linear accumulative damage hypothesis is applied across discrete dynamic equivalent load bins, including the site-specific Weibull probability for each wind speed (shape parameter = 11.4 and scale parameter = 2.3), to calculate the hourly damage of the main bearing for every hour. The hourly damage is then iteratively extrapolated to the 20 years lifetime and is also converted into Remaining Useful Life (RUL) of the main bearing within the 20 years.

According to the analysis of this thesis, the key factors contributing to fatigue damage are the dynamic equivalent load, particularly the radial load, which has the greatest impact, and the rotor speed mean and standard deviation, which impact the number of load cycles, especially under the simulated turbulent wind conditions. The latter results in higher fatigue damage of the MB1 in the BOWT at wind speeds below 8.5 m/s, while at wind speeds above 9.5 m/s, the MB1 of the FOWT experiences higher damage (as depicted in Figure 5.24a). Finally, wind speed probability, determined by the Weibull distribution, plays a critical role in the fatigue damage of MB1, since, at the selected location in the North Sea, the most frequent wind speeds lie between 6 and 12 m/s. Thus, the results indicate that the below-rated wind speed region contributes the most to the cumulative damage of MB1 across the operating regions, representing 36.6% and 40.4% of its total cumulative damage for the FOWT and BOWT, respectively (as portrayed in Figure 5.24b).

Sub-question 4:
Which environmental and system parameters have the greatest impact on the fatigue damage of the main bearings?

In this study, to determine the impact of environmental and system parameters on the fatigue damage of MB1, a parametric analysis is performed at six typical wind speeds, 8.5, 10.5, 11.5, 13.5, 16.5 and 23.5 m/s. For system parameters, tests include a $\pm 20\%$ variation in nacelle mass for both the FOWT and BOWT. For the FOWT, the same variation is also applied to the mooring line stiffness and platform mass. Furthermore, in terms of environmental parameters, a change of turbulence class from class A to class B and C, and a $\pm 20\%$ change in significant wave height (H_s) and peak spectral period (T_p), are implemented in both the FOWT and BOWT for the selected wind speeds. The purpose of this sensitivity analysis is only comparative, to qualitatively identify the most impactful parameters. It is not intended to propose new designs, which would require a more in-depth analysis to evaluate how natural and excitation frequencies vary under different conditions.

To evaluate the required change, the dynamic equivalent load and platform motions are compared, as well as the axial-to-radial load ratio at each wind speed and the cumulative damage from the contribution of the six selected wind speeds. The comparison data can be found in detail in Section 5.3. The results of this study suggest that turbulence intensity has the greatest impact on the MB1 damage. As shown in Table 5.6, for the BOWT, changing turbulence class from A to B and C reduces the damage of MB1 by 5.27 and 9.92%, respectively. For the FOWT, the corresponding reductions are 3.92 and 8.07%. This suggests that lower load variability, resulting from lower turbulence intensity, decreases the damage, by a greater rate in the BOWT, where the drivetrain directly experiences load changes. In contrast, in the FOWT, the platform's coupling with the tower and drivetrain absorbs part of these perturbations, mitigating the impact on the main bearing. Furthermore, platform mass is the most influential system parameter for the FOWT. A 20% increase in the platform mass reduces the MB1 fatigue damage by 5.6%, whereas a 20% lighter platform mass increases the MB1 fatigue damage by 4.4%.

Following the four research sub-questions, the main research question is answered below:

Main research question:
"How do the loading and fatigue damage of the main bearing differ between bottom-fixed and floating offshore wind turbines, and what is their sensitivity to environmental and system parameters?"

The findings of this research confirm that semi-submersible floating wind turbines (FOWTs) and bottom-fixed monopile wind turbines (BOWTs) experience different load mechanisms, although being subjected to identical environmental input conditions. While the BOWT remains rigidly fixed to the seabed, the FOWT is affected by the platform motion and the aero-hydro-servo coupling, which amplify its loads.

Radial loads dominate the MB1 loading and fatigue damage in both configurations. The activation of blade pitch control in the above-rated region reduces both axial and radial loads, However, the FOWT shows equal or higher mean loads acting on the MB1 across all operating wind speeds. The most noticeable difference occurs at 13.5 m/s, where the mean axial load is higher by 13.17% for the FOWT. This increase is primarily attributed to the pitch and surge platform motions that amplify the rotor thrust. At the wind speed of 13.5 m/s, the differences between FOWT and BOWT also peak for the dynamic equivalent load at 5.83% and for the radial load at 3.66%. Finally, the thesis reveals that the radial load of the FOWT is further affected by the sway, heave, roll, and yaw motions of the platform.

Regarding MB1 fatigue damage, the FOWT accumulates a total MB1 fatigue damage of 1.67 over a 20-year lifetime, corresponding to a failure after 11.98 years. This compares to a total damage of 1.59 for the BOWT, corresponding to a failure after 12.58 years. This represents a 5.03% higher fatigue damage for the FOWT than for the BOWT. The aligned wind-wave cases show a marginal 0.6% reduction in the 20-year cumulative damage of MB1, indicating that wind-wave misalignment has negligible impact on the MB1 fatigue damage for the investigated conditions.

Further insights show that the BOWT experiences slightly higher MB1 fatigue damage in the below-rated region than the FOWT, by 3.8%, due to higher rotor speeds. Conversely, the FOWT exhibits higher fatigue damage in the around rated (10.5 - 12.5 m/s) and above-rated region by 1.7% and 2.0% respectively, when the rotor speeds of the BOWT and FOWT converge and the loads are amplified.

Finally, the parametric study identifies that turbulence intensity has the strongest impact on the damage of MB1 for both FOWT and BOWT. A transition from turbulence class A to C, lowers the fatigue damage for the six selected wind speeds, by nearly 10% in the BOWT and 8% in the FOWT. This difference arises because wind-induced load fluctuations are transmitted directly to the drivetrain in BOWTs, whereas in FOWTs, platform motion absorbs some of these fluctuations. Among system parameters, for the FOWT, a 20% heavier platform reduces the damage of MB1 by 5.6%, whereas a 20% lower platform mass increases the damage by 4.4%, due to more intense platform motions. Mooring line stiffness, nacelle mass and wave characteristics ($H_s - T_p$) have a significantly lower effect.

In summary, floating wind turbines experience more complex and severe upwind main bearing loads, primarily due to the platform motion dynamics and coupled aerodynamic, hydrodynamic, structural and control interactions. This results in higher cumulative fatigue damage, that is highly sensitive to the turbulence intensity and the control strategies implemented. These findings pave the way for a fatigue-informed system integration in future floating wind developments.

7.2. Recommendations for future work

In this section, some previously mentioned limitations of this project are summarized, along with corresponding recommendations for future work.

7.2.1. Metocean Conditions

To begin with, as presented in Chapter 4, for this thesis, the operating wind speeds of DTU 10 MW RWT are considered according to DLC 1.2, for a specific location in the North Sea with site-specific metocean conditions and Weibull distribution. These are introduced in hourly simulations in OpenFAST and the post-processing stage, and the outputs are used iteratively for every hour of the 20 years, considering, for instance, the same turbulent conditions and variations. Therefore, a first recommendation for future work would be to adopt real data and metocean conditions over 20 years, with variable conditions to model more realistic conditions. Moreover, a validation of the results with real field or experimental data would be a valuable addition.

Next, by using a specific location and a site-specific Weibull distribution, the numerical results are limited to that location or locations with similar conditions. However, the relative conclusions, such as the differences between the loading mechanisms of FOWTs and BOWTs and the impact of platform motions, are transferable and can be generalized to other locations. Thus, it would be interesting to implement the proposed methodology in a different location, to verify the extracted conclusions, and compare the results, for example, the total damage or the failure time of the main bearings, and the maximum values of the loads or their differences between the two WT configurations.

Furthermore, in Subsection 3.4.2, it is mentioned that for the simulation of the semi-submersible FOWT, the potential flow theory is used in HydroDyn, considering only the first order terms (linear wave theory) and not the second order terms and forces, that account for nonlinear effects, that requires outputs from the WAMIT software [92] to be modeled in OpenFAST. Consequently, a proposal could be to use the commercial software WAMIT and calculate the second-order terms of the potential flow theory to identify how they could potentially influence the platform motions, loads, and damage of the main bearings. In that direction, another suggestion would be to use the JONSWAP wave spectrum instead of the Pierson-Moskowitz considered in this thesis, to investigate how that would impact the platform motions and loads of the main bearings.

7.2.2. System components and validation

In Section 6.3, it is shown that the controller used in this thesis is unstable for the wind speeds between 11.5 and 14.5 m/s. It is explained that this instability does not intensify the loads of the main bearing and the relevant damage compared to that of the BOWT. However, it would be beneficial for a more realistic modeling of the FOWT control strategy and to account for the platform-induced dynamics, to use advanced control designs, tailored to the dynamic coupled behavior of the FOWT, such as gain scheduling, multi-loop feedback or model predictive control [125].

Subsequently, for drivetrain layout, it would be interesting to test a different main bearings layout (for instance, one locating and one non-locating main bearing) to investigate how the load distribution changes and what the impact is on the loading and the fatigue damage of the two main bearings. Moreover, in this thesis, an analytical formulation is used to compute the loads on the main bearings. Therefore, it would be useful to validate the load results, with SIMPACK, which is a high-fidelity multibody simulation software [60]. Additionally, in this research, following the guidelines of IEC 61400-3-1: 2019 [53], hourly simulations are performed. Another suggestion would be to perform shorter stochastic simulations with more seeds, at least for a few wind speeds, to examine if the results would change.

Finally, this study focuses on time-domain fatigue indicators (mean loads, standard deviations and load cycles), which are suitable for long-term fatigue damage analysis, along with physical interpretation of the loads and the impact of the platform motion. However, future work could be complemented and benefited from thorough frequency-domain analysis to understand potential resonance and dynamic coupling of the system, especially in floating platforms, where there are a lot of motions in the low-frequency range.

References

[1] Ocean Energy Resources. *First Turbine Rises at HKN Offshore Wind Park*. 2023. URL: https://ocean-energyresources.com/2023/04/16/first-turbine-rises-at-hkn-offshore-wind-park/ (visited on 07/15/2025).

[2] IPCC. *Climate Change 2023: Synthesis Report*. Geneva, 2023. IPCC, July 25, 2023. DOI: 10.59327/IPCC/AR6-9789291691647. URL: https://www.ipcc.ch/report/ar6/syr/ (visited on 01/29/2025).

[3] UNFCCC. *Conference of the Parties (COP)*. 2025. URL: https://unfccc.int/process/bodies/supreme-bodies/conference-of-the-parties-cop (visited on 01/29/2025).

[4] United Nations Framework Convention on Climate Change. *The Paris Agreement*. 2015. URL: https://unfccc.int/sites/default/files/english_paris_agreement.pdf (visited on 01/10/2025).

[5] International Renewable Energy Agency. *World Energy Transitions Outlook 2024: 1.5°C Pathway, Abu Dhabi*. 2024. URL: https://www.irena.org/-/media/Files/IRENA/Agency/Publication/2024/Nov/IRENA_World_energy_transitions_outlook_2024.pdf (visited on 01/10/2025).

[6] Global Wind Energy Council. *Global Wind Report 2024*. 2024. URL: https://gwec.net/wp-content/uploads/2024/04/GWR-2024_digital-version_final-1.pdf (visited on 01/29/2025).

[7] P.J.M. Bussemakers. “Validation of aero-hydro-servo-elastic load and motion simulations in BHawC/OrcaFlex for the Hywind Scotland floating offshore wind farm”. MA thesis. Delft University of Technology, 2020. URL: https://resolver.tudelft.nl/uuid:5607a38d-6666-4cb3-9ebf-ba2a66a899fe.

[8] N. Yildiz, H. Hemida, and C. Baniotopoulos. “Operation, Maintenance, and Decommissioning Cost in Life-Cycle Cost Analysis of Floating Wind Turbines”. In: *Energies* 17.6 (2024), p. 1332. ISSN: 1996-1073. DOI: 10.3390/en17061332. URL: https://www.mdpi.com/1996-1073/17/6/1332 (visited on 01/20/2025).

[9] E. Paya and A. Zigeng Du. *The frontier between fixed and floating foundations in offshore wind*. 2020. URL: https://www.empireengineering.co.uk/the-frontier-between-fixed-and-floating-foundations-in-offshore-wind/ (visited on 01/30/2025).

[10] Energy Knowledge Institute. *World’s deepest fixed-bottom offshore wind farm now fully operational*. 2023. URL: https://knowledge.energyinst.org/new-energy-world/article?id=138330 (visited on 02/02/2025).

[11] O. Gaidai et al. “Novel Reliability Method Validation for Floating Wind Turbines”. In: *Advanced Energy and Sustainability Research* 4.8 (2023), p. 2200177. ISSN: 2699-9412, 2699-9412. DOI: 10.1002/aesr.202200177. URL: https://onlinelibrary.wiley.com/doi/10.1002/aesr.202200177 (visited on 01/28/2025).

[12] Equinor. *Hywind Scotland*. 2018. URL: https://www.equinor.com/energy/hywind-scotland (visited on 01/13/2025).

[13] G. Song. *Stay Ashore: Offshore Wind O&M Automation*. 2023. URL: https://cse.umn.edu/safl/events/stay-ashore-offshore-wind-om-automation-guiju-song-ge-research (visited on 06/30/2025).

[14] D. Zappalá and P. J. Tavner. “2.11 - Wind Turbine Reliability - Maintenance Strategies”. In: *Comprehensive Renewable Energy, Second Edition: Volume 1-9*. Vol. 1-9. Elsevier, Jan. 2022, pp. 353–370. ISBN: 978-0-12-819734-9. DOI: 10.1016/B978-0-12-819727-1.00154-0.

[15] W. Wiley et al. “Sensitivity analysis of numerical modeling input parameters on floating offshore wind turbine loads”. In: *Wind Energy Science* 8.10 (Oct. 2023). Publisher: Copernicus Publications, pp. 1575–1595. ISSN: 23667451. DOI: `10.5194/wes-8-1575-2023`.

[16] DHI Group. *Decode Offshore Wind Engineering Challenges at Every Stage*. 2024. URL: `https://blog.dhigroup.com/decode-offshore-wind-engineering-challenges-at-every-stage/` (visited on 03/15/2025).

[17] Y. J. Kim et al. “Foundation Types of Fixed Offshore Wind Turbine”. In: *Journal of Ocean Engineering and Technology* 38.2 (2024), pp. 74–85. ISSN: 1225-0767, 2287-6715. DOI: `10.26748/KSOE.2024.041`. URL: `http://joet.org/journal/view.php?doi=10.26748/KSOE.2024.041` (visited on 03/15/2025).

[18] Global Growth Insights. *Offshore Wind Power Market Size, Share, Growth, and Industry Analysis*. 2025. URL: `https://www.globalgrowthinsights.com/market-reports/offshore-wind-power-market-106335` (visited on 08/12/2025).

[19] A. Lamei and M. Hayatdavoodi. “On motion analysis and elastic response of floating offshore wind turbines”. In: *Journal of Ocean Engineering and Marine Energy* 6.1 (Feb. 2020), pp. 71–90. ISSN: 2198-6444, 2198-6452. DOI: `10.1007/s40722-019-00159-2`. URL: `http://link.springer.com/10.1007/s40722-019-00159-2` (visited on 12/02/2024).

[20] Mordor Intelligence. *Floating Offshore Wind Power Market Size & Share Analysis - Growth Trends & Forecasts (2025 - 2030)*. 2025. URL: `https://www.mordorintelligence.com/industry-reports/floating-offshore-wind-power-market` (visited on 08/01/2025).

[21] Deepwater Buoyancy. *Mooring Matters: Fixed vs. Floating Offshore Wind Turbines*. 2023. URL: `https://deepwaterbuoyancy.com/comparing-fixed-and-floating-offshore-wind-turbines/` (visited on 03/15/2025).

[22] C. D. Dao et al. “Integrated condition□based maintenance modelling and optimisation for offshore wind turbines”. In: *Wind Energy* 24.11 (2021), pp. 1180–1198. ISSN: 1095-4244, 1099-1824. DOI: `10.1002/we.2625`. URL: `https://onlinelibrary.wiley.com/doi/10.1002/we.2625` (visited on 02/09/2025).

[23] M. Shafiee and J. D. Sørensen. “Maintenance optimization and inspection planning of wind energy assets: Models, methods and strategies”. In: *Reliability Engineering & System Safety* 192 (Dec. 2019), p. 105993. ISSN: 09518320. DOI: `10.1016/j.ress.2017.10.025`. URL: `https://linkinghub.elsevier.com/retrieve/pii/S095183201630789X` (visited on 02/10/2025).

[24] I. Leo. “Investigation of Wind Turbine Rotor Imbalances Using Drivetrain Signals”. MA thesis. Delft University of Technology, 2024. URL: `https://resolver.tudelft.nl/uuid:b314cc00-6e61-4d20-b70d-c36597fe6515`.

[25] C. J. Crabtree, D. Zappalá, and S. I. Hogg. “Wind energy: UK experiences and offshore operational challenges”. In: *Proceedings of the Institution of Mechanical Engineers, Part A: Journal of Power and Energy* 229.7 (2015), pp. 727–746. ISSN: 0957-6509, 2041-2967. DOI: `10.1177/0957650915597560`. URL: `https://journals.sagepub.com/doi/10.1177/0957650915597560` (visited on 02/09/2025).

[26] François Besnard. “On maintenance optimization for offshore wind farms”. In: (2013).

[27] BVGAssociates, Catapult Offshore Renewable Energy, The Crown Estate and Crown Estate Scotland. *Guide to Floating Offshore Wind: Wind Farm Costs*. 2025. URL: `https://guidetofloatingoffshorewind.com/wind-farm-costs/` (visited on 02/26/2025).

[28] N. Yildiz, H. Hemida, and C. Baniotopoulos. “Operation, Maintenance, and Decommissioning Cost in Life-Cycle Cost Analysis of Floating Wind Turbines”. In: *Energies* 17.6 (2024), p. 1332. ISSN: 1996-1073. DOI: `10.3390/en17061332`. URL: `https://www.mdpi.com/1996-1073/17/6/1332` (visited on 01/20/2025).

[29] J. McMorland et al. “Operation and maintenance for floating wind turbines: A review”. In: *Renewable and Sustainable Energy Reviews* 163 (2022), p. 112499. ISSN: 13640321. DOI: `10.1016/j.rser.2022.112499`. URL: `https://linkinghub.elsevier.com/retrieve/pii/S1364032122004038` (visited on 12/02/2024).

[30] G. Katsouris and A. Marina. *Cost modelling of floating wind farms*. ECN Petten, The Netherlands, 2016.

[31] A. Dewan and M. Asgarpour. *Reference O & M Concepts for Near and Far Offshore Wind Farms*. ECN Petten, 2016.

[32] G. Rinaldi, P.R. Thies, and L. Johanning. “Improvements in the O&M modelling of floating offshore wind farms”. In: *Developments in Renewable Energies Offshore*. Ed. by C. Guedes Soares. 1st ed. CRC Press, Oct. 12, 2020, pp. 481–487. ISBN: 978-1-003-13457-2. DOI: `10.1201/9781003134572-54`. URL: `https://www.taylorfrancis.com/books/9781000318739/chapters/10.1201/9781003134572-54` (visited on 02/12/2025).

[33] S. Margaronis. “Equinor says Scotland floating wind turbine flaw has been repaired”. In: *American Journal of Transportation* (2024). URL: `https://www.ajot.com/insights/full/ai-equinor-says-scotland-floating-wind-turbine-flaw-has-been-repaired` (visited on 02/12/2025).

[34] Global Maritime. *Heavy maintenance campaign completed on Hywind Scotland floating offshore wind farm*. 2024. URL: `https://www.globalmaritime.com/news/heavy-maintenance-campaign-completed-on-hywind-scotland` (visited on 02/12/2025).

[35] L. Sandvik. *Hywind Scotland to shut down for months due to extensive maintenance*. 2024. URL: `https://energywatch.com/EnergyNews/Renewables/article16759185.ece` (visited on 02/12/2025).

[36] H. Li et al. “Failure Rate Assessment for Onshore and Floating Offshore Wind Turbines”. In: *Journal of Marine Science and Engineering* 10.12 (Dec. 2022). Publisher: MDPI. ISSN: 20771312. DOI: `10.3390/jmse10121965`.

[37] M. Wilkinson. “Measuring Wind Turbine Reliability-Results of the Reliawind Project”. In: 2011. URL: `https://api.semanticscholar.org/CorpusID:128347265` (visited on 02/14/2025).

[38] J. Carroll, A. McDonald, and D. McMillan. “Failure rate, repair time and unscheduled O&M cost analysis of offshore wind turbines”. In: *Wind Energy* 19.6 (2016), pp. 1107–1119. ISSN: 1095-4244, 1099-1824. DOI: `10.1002/we.1887`. URL: `https://onlinelibrary.wiley.com/doi/10.1002/we.1887` (visited on 01/23/2025).

[39] P. DT O’connor and A. V. Kleyner. *Practical reliability engineering*. john wiley & sons, 2011.

[40] J. Ribrant and L. Bertling. “Survey of failures in wind power systems with focus on Swedish wind power plants during 1997-2005”. In: *2007 IEEE Power Engineering Society General Meeting*. 2007, pp. 1–8. DOI: `10.1109/PES.2007.386112`.

[41] P. Tavner et al. “Reliability & Availability of Wind Turbine Electrical & Electronic Components”. In: *EPE Journal* 20.4 (2010), pp. 45–50. DOI: `10.1080/09398368.2010.11463777`. URL: `https://doi.org/10.1080/09398368.2010.11463777` (visited on 02/25/2025).

[42] S. Faulstich, B. Hahn, and P. J. Tavner. “Wind turbine downtime and its importance for offshore deployment”. In: *Wind Energy* 14.3 (2011), pp. 327–337. DOI: `https://doi.org/10.1002/we.421`. URL: `https://onlinelibrary.wiley.com/doi/abs/10.1002/we.421` (visited on 03/25/2025).

[43] A. Martinez and G. Iglesias. “Mapping of the levelised cost of energy for floating offshore wind in the European Atlantic”. In: *Renewable and Sustainable Energy Reviews* 154 (2022), p. 111889. ISSN: 1364-0321. DOI: `https://doi.org/10.1016/j.rser.2021.111889`. URL: `https://www.sciencedirect.com/science/article/pii/S1364032121011564`.

[44] W. Dong et al. “Time domain-based gear contact fatigue analysis of a wind turbine drivetrain under dynamic conditions”. In: *International Journal of Fatigue* 48 (2013), pp. 133–146. ISSN: 01421123. DOI: `10.1016/j.ijfatigue.2012.10.011`. URL: `https://linkinghub.elsevier.com/retrieve/pii/S0142112312002964` (visited on 03/17/2025).

[45] H. Li and C. G. Soares. “Assessment of failure rates and reliability of floating offshore wind turbines”. In: *Reliability Engineering and System Safety* 228 (Dec. 2022). Publisher: Elsevier Ltd. ISSN: 09518320. DOI: `10.1016/j.ress.2022.108777`.

[46] E. Hart et al. “A review of wind turbine main bearings: design, operation, modelling, damage mechanisms and fault detection”. In: *Wind Energy Science* 5.1 (2020), pp. 105–124. ISSN: 2366-7451. DOI: `10.5194/wes-5-105-2020`. URL: `https://wes.copernicus.org/articles/5/105/2020/` (visited on 03/13/2025).

[47] J. Keller et al. *Wind Turbine Drivetrain Reliability Collaborative Workshop: A Recap*. NREL/TP–5000-66593, DOE/GO–102016-4878, 1314863. Aug. 1, 2016, NREL/TP–5000–66593, DOE/GO–102016–4878, 1314863. DOI: `10.2172/1314863`. URL: `http://www.osti.gov/servlets/purl/1314863/` (visited on 03/13/2025).

[48] E. Hart et al. “Wind turbine main bearing loading and wind field characteristics”. In: *Wind Energy* 22.11 (Nov. 2019), pp. 1534–1547. ISSN: 1095-4244, 1099-1824. DOI: `10.1002/we.2386`. URL: `https://onlinelibrary.wiley.com/doi/10.1002/we.2386` (visited on 03/13/2025).

[49] J. McMorland et al. “Operation and maintenance for floating wind turbines: A review”. In: *Renewable and Sustainable Energy Reviews* 163 (July 2022), p. 112499. ISSN: 13640321. DOI: `10.1016/j.rser.2022.112499`. URL: `https://linkinghub.elsevier.com/retrieve/pii/S1364032122004038` (visited on 12/02/2024).

[50] A. R. Nejad et al. “Wind turbine drivetrains: state-of-the-art technologies and future development trends”. In: *Wind Energy Science* 7.1 (Feb. 21, 2022), pp. 387–411. ISSN: 2366-7451. DOI: `10.5194/wes-7-387-2022`. URL: `https://wes.copernicus.org/articles/7/387/2022/` (visited on 01/16/2025).

[51] W. Dheelibun Remigius and A. Natarajan. “A review of wind turbine drivetrain loads and load effects for fixed and floating wind turbines”. In: *WIREs Energy and Environment* 11.1 (Jan. 2022). ISSN: 2041-8396, 2041-840X. DOI: `10.1002/wene.417`. URL: `https://wires.onlinelibrary.wiley.com/doi/10.1002/wene.417` (visited on 12/02/2024).

[52] A. R. Nejad and J. Torsvik. “Drivetrains on floating offshore wind turbines: lessons learned over the last 10 years”. In: *Forschung im Ingenieurwesen* 85.2 (June 2021), pp. 335–343. ISSN: 0015-7899, 1434-0860. DOI: `10.1007/s10010-021-00469-8`. URL: `https://link.springer.com/10.1007/s10010-021-00469-8` (visited on 12/02/2024).

[53] International Electrotechnical Commission (IEC). *IEC 61400-3-1:2019: Wind Turbines – Part 3-1: Design requirements for fixed offshore wind turbines*. 1.0. ICS 27.180. Geneva, Switzerland: International Electrotechnical Commission (IEC), 2019.

[54] International Electrotechnical Commission (IEC). *IEC 61400-3-2:2019: Wind Turbines – Part 3-2: Design requirements for floating offshore wind turbines*. 1.0. ICS 27.180. Geneva, Switzerland: International Electrotechnical Commission (IEC), 2019.

[55] International Electrotechnical Commission (IEC). *IEC 61400-4:2012: Wind Turbines – Part 4: Design requirements for wind turbine gearboxes*. 1.0. NEK IEC 61400-4:2012 provided by Standard Online for NTNU Universitetsbiblioteket. Geneva, Switzerland: International Electrotechnical Commission (IEC), 2012.

[56] H. Polinder et al. “Comparison of direct-drive and geared generator concepts for wind turbines”. In: *IEEE Transactions on Energy Conversion* 21.3 (2006), pp. 725–733. DOI: `10.1109/TEC.2006.875476`.

[57] R. Bergua, J. Jové, and J. Echarte. “Pure Torque Drivetrain Design: A Proven Solution for Increasing the Wind Turbine Reliability”. In: *Conference: Brazil Wind Power*. Aug. 2014.

[58] J. N. Stander, G. Venter, and M. J. Kamper. “Review of direct-drive radial flux wind turbine generator mechanical design”. In: *Wind Energy* 15.3 (2012), pp. 459–472. DOI: `https://doi.org/10.1002/we.484`. URL: `https://onlinelibrary.wiley.com/doi/abs/10.1002/we.484` (visited on 03/27/2025).

[59] National Renewable Energy Laboratory (NREL). *OpenFAST Documentation*. 2023. URL: `https://openfast.readthedocs.io/en/main/` (visited on 05/19/2025).

[60] Dassault Systemes. *Simpack: Multibody System Simulation Software*. 2025. URL: `https://www.3ds.com/products/simulia/simpack` (visited on 01/06/2025).

[61] Hexagon AB. *Romax*. 2025. URL: `https://hexagon.com/products/product-groups/computer-aided-engineering-software/romax` (visited on 08/13/2025).

[62] F. C. Mehlan and A. R. Nejad. “Rotor imbalance detection and diagnosis in floating wind turbines by means of drivetrain condition monitoring”. In: *Renewable Energy* 212 (Aug. 2023), pp. 70–81. ISSN: 09601481. DOI: `10.1016/j.renene.2023.04.102`. URL: `https://linkinghub.elsevier.com/retrieve/pii/S0960148123005682` (visited on 01/23/2025).

[63] V. L. Krathe et al. “Investigation of Main Bearing Fatigue Estimate Sensitivity to Synthetic Turbulence Models Using a Novel Drivetrain Model Implemented in OpenFAST”. In: *Wind Energy* 28.3 (2025). e70005 we.70005, e70005. DOI: `https://doi.org/10.1002/we.70005`. URL: `https://onlinelibrary.wiley.com/doi/abs/10.1002/we.70005` (visited on 04/03/2025).

[64] S. Wang, A. R. Nejad, and T Moan. “On design, modelling, and analysis of a 10-MW medium-speed drivetrain for offshore wind turbines”. In: *Wind Energy* 23.4 (Apr. 2020). Publisher: John Wiley and Sons Ltd, pp. 1099–1117. ISSN: 10991824. DOI: `10.1002/we.2476`.

[65] E. Hart et al. “Impacts of wind field characteristics and non-steady deterministic wind events on time-varying main-bearing loads”. In: *Wind Energy Science* 7.3 (2022), pp. 1209–1226. ISSN: 2366-7451. DOI: `10.5194/wes-7-1209-2022`. URL: `https://wes.copernicus.org/articles/7/1209/2022/` (visited on 05/28/2025).

[66] Y. Guo et al. *An Analytical Formulation for Sizing and Estimating the Dimensions and Weight of Wind Turbine Hub and Drivetrain Components*. Tech. rep. NREL/TP-5000-63008. National Renewable Energy Laboratory (NREL), 2015. URL: `https://www.nrel.gov/docs/fy15osti/63008.pdf` (visited on 04/03/2025).

[67] Z. Jiang et al. “Dynamic reliability analysis of main shaft bearings in wind turbines”. In: *International Journal of Mechanical Sciences* 235 (Dec. 2022), p. 107721. ISSN: 00207403. DOI: `10.1016/j.ijmecsci.2022.107721`. URL: `https://linkinghub.elsevier.com/retrieve/pii/S0020740322006014` (visited on 01/16/2025).

[68] International Organization for Standardization (ISO). *ISO 281:2007 Rolling bearings — Dynamic load ratings and rating life*. second. International Organization for Standardization (ISO), 2007.

[69] J. Ben Ali et al. “Accurate bearing remaining useful life prediction based on Weibull distribution and artificial neural network”. In: *Mechanical Systems and Signal Processing* 56-57 (2015), pp. 150–172. ISSN: 08883270. DOI: `10.1016/j.ymssp.2014.10.014`. URL: `https://linkinghub.elsevier.com/retrieve/pii/S0888327014004087` (visited on 08/13/2025).

[70] F. C. Mehlan, J. Keller, and A. R. Nejad. “Virtual sensing of wind turbine hub loads and drivetrain fatigue damage”. In: *Forschung im Ingenieurwesen/Engineering Research* 87.1 (Mar. 2023). Publisher: Springer Vieweg, pp. 207–218. ISSN: 14340860. DOI: `10.1007/s10010-023-00627-0`.

[71] Zaaijer, M. and Viré, A. *Introduction to wind turbines: physics and technology*. 2023.

[72] J.M. Jonkman et al. *AeroDyn v15 User’s Guide and Theory Manual*. Technical Report. National Renewable Energy Laboratory (NREL), 2015. URL: `https://openfast.readthedocs.io/en/dev/source/user/` (visited on 04/01/2025).

[73] J. M. Jonkman, A N Robertson, and G J Hayman. “HydroDyn User’s Guide and Theory Manual”. In: *National Renewable Energy Laboratory* (2015).

[74] J. M. Jonkman and M. L. Buhl Jr. *FAST User’s Guide*. Tech. rep. NREL/EL-500-38230. Report No. NREL/EL-500-38230. National Renewable Energy Laboratory, 2005.

[75] A. Platt, B. Jonkman, and J. Jonkman. *InflowWind User’s Guide*. Tech. rep. National Renewable Energy Laboratory, 2016. URL: `https://www2.nrel.gov/wind/nwtc/inflowwind` (visited on 04/01/2025).

[76] B.J. Jonkman. *TurbSim User’s Guide: Version 1.50*. Tech. rep. NREL/TP-5000-46198. National Renewable Energy Laboratory, 2009. URL: `https://www.nrel.gov/docs/fy09osti/46198.pdf` (visited on 04/01/2025).

[77] National Renewable Energy Laboratory (NREL). *ServoDyn Module User Guide*. Accessed via OpenFAST Documentation. NREL. 2023. URL: `https://openfast.readthedocs.io/en/main/source/user/servodyn/` (visited on 04/01/2025).

[78] M. Hall. *MoorDyn User's Guide*. Tech. rep. Version 1.00.02, December 15, 2015. University of Maine, Department of Mechanical Engineering, 2015. URL: `https://www.matt-hall.ca/moordyn` (visited on 04/01/2025).

[79] R. Damiani, J. Jonkman, and G. Hayman. *SubDyn User's Guide and Theory Manual*. Tech. rep. NREL/TP-5000-63062. National Renewable Energy Laboratory, 2015. URL: `https://www.nrel.gov/docs/fy15osti/63062.pdf` (visited on 04/01/2025).

[80] B. Jonkman and J. Jonkman. *FAST v8.16.00*. Accessed via OpenFAST Documentation. 2016. URL: `https://openfast.readthedocs.io/en/dev/_downloads/5f2ddf006568adc9b88d8118dc3f1732/FAST8_README.pdf` (visited on 04/01/2025).

[81] Integrum Energy. *Understanding Cut-in Wind Speed: The Key to Wind Turbine Efficiency*. 2025. URL: `https://www.linkedin.com/pulse/understanding-cut-in-wind-speed-key-turbine-efficiency-au9tc/` (visited on 03/31/2025).

[82] International Electrotechnical Commission (IEC). *IEC 61400-3:2009 Wind Turbines – Part 3: Design requirements for offshore wind turbines*. 1.0. ICS 27.180. Geneva, Switzerland: International Electrotechnical Commission (IEC), 2009.

[83] International Electrotechnical Commission (IEC). *IEC 61400-1:2019: Wind energy generation systems - Part 1: Design requirements*. 1.0. ICS 27.180. Geneva, Switzerland: International Electrotechnical Commission (IEC), 2019.

[84] International Electrotechnical Commission (IEC). *IEC 61400-1: Wind energy generation systems – Part 1: Design requirements*. Edition 4.0, Geneva, Switzerland. International Electrotechnical Commission (IEC), 2019.

[85] D. Karystinou. "Sensitivity Analysis of Hydrodynamic Parameters on the Dynamic Response of the Semisubmersible Floating Offshore Wind turbine with the use of OpenFAST". MSc Thesis. Delft University of Technology, 2021. URL: `https://resolver.tudelft.nl/uuid:f747bbd4-fee3-4d03-ad4d-f673f20810a2`.

[86] J.M.J. Journee and W.W. Massie. *Offshore Hydromechanics*. `https://ocw.tudelft.nl/wp-content/uploads/OffshoreHydromechanics_Journee_Massie.pdf`. First Edition. 2001.

[87] T. T. Tran and D. H. Kim. "A CFD study into the influence of unsteady aerodynamic interference on wind turbine surge motion". In: *Renewable Energy* 90 (May 2016), pp. 204–228. ISSN: 09601481. DOI: `10.1016/j.renene.2015.12.013`. URL: `https://linkinghub.elsevier.com/retrieve/pii/S0960148115305188` (visited on 04/07/2025).

[88] I. Filippidis. "Energy Yield Comparison of Spar & Monopile Offshore Wind Turbines using BEM & OLAF Models". MSc Thesis. Delft University of Technology, 2023. URL: `https://resolver.tudelft.nl/uuid:690ce59e-c69f-4d5d-8713-cdd81173e932`.

[89] D. Matha et al. "Modelling of Floating Offshore Wind Technologies". In: *Floating Offshore Wind Energy: The Next Generation of Wind Energy*. Ed. by Arthur Pecher and Jens Peter Kofoed. Springer International Publishing, 2016, pp. 133–240. DOI: `10.1007/978-3-319-29398-1_4`. URL: `https://link.springer.com/chapter/10.1007/978-3-319-29398-1_4`.

[90] M. Lerch, M. De-Prada-Gil, and C. Molins. "The influence of different wind and wave conditions on the energy yield and downtime of a Spar-buoy floating wind turbine". In: *Renewable Energy* 136 (June 2019), pp. 1–14. ISSN: 09601481. DOI: `10.1016/j.renene.2018.12.096`. URL: `https://linkinghub.elsevier.com/retrieve/pii/S096014811831543X` (visited on 04/01/2025).

[91] J. Dai et al. "Modeling and investigation of load and motion characteristics of offshore floating wind turbines". In: *Ocean Engineering* 159 (July 2018), pp. 187–200. ISSN: 00298018. DOI: `10.1016/j.oceaneng.2018.04.003`. URL: `https://linkinghub.elsevier.com/retrieve/pii/S0029801818304153` (visited on 12/02/2024).

[92] WAMIT, Inc. *WAMIT: Wave Analysis MIT*. 2025. URL: `https://www.wamit.com/` (visited on 07/15/2025).

[93] H. Geng and G. Yang. "Linear and Nonlinear Schemes Applied to Pitch Control of Wind Turbines". In: *The Scientific World Journal* 2014.1 (2014), p. 406382. DOI: `https://doi.org/10.1155/2014/406382`. URL: `https://onlinelibrary.wiley.com/doi/abs/10.1155/2014/406382` (visited on 06/22/2025).

[94] N. J. Abbas et al. "A reference open-source controller for fixed and floating offshore wind turbines". In: *Wind Energy Science* 7.1 (Jan. 19, 2022), pp. 53–73. ISSN: 2366-7451. DOI: `10.5194/wes-7-53-2022`. URL: `https://wes.copernicus.org/articles/7/53/2022/` (visited on 06/22/2025).

[95] Koyo bearing. *KOYO tapered roller bearings 2TR1450*. WHCD bearing. 2025. URL: `https://www.whcdbearings.com/product/koyo-tapered-roller-bearings-2tr1450/` (visited on 04/03/2025).

[96] V.-C. Tong and S.-W. Hong. "Characteristics of Tapered Roller Bearing Subjected to Combined Radial and Moment Loads". In: *International Journal of Precision Engineering and Manufacturing-Green Technology* 1.4 (2014), pp. 323–328. DOI: `10.1007/s40684-014-0040-1`.

[97] H. Zhang et al. "A Method to Solve the Stiffness of Double-Row Tapered Roller Bearing". In: *Mathematical Problems in Engineering* 2019 (2019), pp. 1–13. DOI: `10.1155/2019/1857931`.

[98] T. A. Harris and M. N. Kotzalas. *Rolling Bearing Analysis: Advanced Concepts of Bearing Technology*. 5th. CRC Press, Taylor & Francis Group, 2007. ISBN: 9780849371820.

[99] J. E. Shigley et al. *Mechanical Engineering Design*. 10th. McGraw-Hill Education, 2015. ISBN: 9780073398204.

[100] C. Hübler and R. Rolfes. "Probabilistic temporal extrapolation of fatigue damage of offshore wind turbine substructures based on strain measurements". In: *Wind Energy Science* 7.5 (2022), pp. 1919–1940. ISSN: 2366-7451. DOI: `10.5194/wes-7-1919-2022`. URL: `https://wes.copernicus.org/articles/7/1919/2022/` (visited on 08/08/2025).

[101] L. Cao et al. "Prediction of Remaining Useful Life of Wind Turbine Bearings under Non-Stationary Operating Conditions". In: *Energies* 11.12 (2018), p. 3318. ISSN: 1996-1073. DOI: `10.3390/en11123318`. URL: `https://www.mdpi.com/1996-1073/11/12/3318` (visited on 08/08/2025).

[102] R. Rodriguez Arias and J. Galvan. *NAUTILUS-DTU10 MW Floating Offshore Wind Turbine at Gulf of Maine*. Presented at WindEurope 2018 Conference, Hamburg, Germany. 2018. URL: `https://www.researchgate.net/publication/328359606_NAUTILUS-DTU10_MW_Floating_Offshore_Wind_Turbine_at_Gulf_of_Maine` (visited on 04/02/2025).

[103] J. Galvan et al. "NAUTILUS-DTU10 MW Floating Offshore Wind Turbine at Gulf of Maine: Public numerical models of an actively ballasted semisubmersible". In: *Journal of Physics: Conference Series* 1102 (2018). DOI: `10.1088/1742-6596/1102/1/012015`. URL: `https://www.researchgate.net/publication/328204534_NAUTILUS-DTU10_MW_Floating_Offshore_Wind_Turbine_at_Gulf_of_Maine_Public_numerical_models_of_an_actively_ballasted_semisubmersible` (visited on 04/01/2025).

[104] DTU Wind and Energy Systems and World Bank. *Global Wind Atlas*. `https://globalwindatlas.info/en/`. Accessed: 2025-04-01. 2024.

[105] Mathiesen, M. and Meyer, A. and Kvingedal, B. *Hywind Buchan Deep Metocean Design Basis*. Technical Report RE2014-002. Version Revision 2. Statoil, 2014. URL: `https://marine.gov.scot/sites/default/files/metocean_design_basis_hywind_buchan_deep_mdb_rev2_0.pdf` (visited on 03/10/2025).

[106] J. Velarde. "Design of Monopile Foundations to Support the DTU 10 MW Offshore Wind Turbine". MA thesis. Delft University of Technology, Norwegian University of Science, and Technology, 2016. URL: `https://resolver.tudelft.nl/uuid:ed2c91db-450e-4d64-86a5-9e410bd0ecda`.

[107] W. Shi et al. "Combined effects of aerodynamic and second-order hydrodynamic loads for floating wind turbines at different water depths". In: *Applied Ocean Research* 130 (2023). ISSN: 0141-1187. DOI: `https://doi.org/10.1016/j.apor.2022.103416`. URL: `https://www.sciencedirect.com/science/article/pii/S0141118722003455`.

[108] F. Ding et al. "An integrated approach for wind turbine gearbox fatigue life prediction considering instantaneously varying load conditions". In: *Renewable Energy* 129 (Dec. 2018), pp. 260–270. ISSN: 09601481. DOI: `10.1016/j.renene.2018.05.074`. URL: `https://linkinghub.elsevier.com/retrieve/pii/S0960148118305950` (visited on 02/02/2025).

[109] A. R. Nejad et al. “Correlation between Acceleration and Drivetrain Load Effects for Monopile Offshore Wind Turbines”. In: *Energy Procedia* 94 (2016), pp. 487–496. ISSN: 18766102. DOI: `10.1016/j.egypro.2016.09.219`. URL: `https://linkinghub.elsevier.com/retrieve/pii/S1876610216309006` (visited on 02/16/2025).

[110] A. Saenz-Aguirre et al. “Floating wind turbine energy and fatigue loads estimation according to climate period scaled wind and waves”. In: *Energy Conversion and Management* 271 (Nov. 2022). ISSN: 01968904. DOI: `10.1016/j.enconman.2022.116303`. URL: `https://linkinghub.elsevier.com/retrieve/pii/S0196890422010810` (visited on 02/02/2025).

[111] S. Wang, A. R. Nejad, and T. Moan. “On Initial Design and Modelling of a 10 MW Medium Speed Drivetrain for Offshore Wind Turbines”. In: *Journal of Physics: Conference Series* 1356.1 (2019). ISSN: 1742-6588, 1742-6596. DOI: `10.1088/1742-6596/1356/1/012024`. URL: `https://iopscience.iop.org/article/10.1088/1742-6596/1356/1/012024` (visited on 12/07/2024).

[112] J.D. Sørensen. “Reliability assessment of wind turbines”. In: *Safety, Reliability and Risk Analysis: Beyond the Horizon*. Ed. by R.D.J.M. Steenbergen et al. London: Taylor & Francis Group, 2014, pp. 27–36. ISBN: 978-1-138-00123-7.

[113] Y. Li et al. “Fatigue reliability analysis of wind turbine drivetrain considering strength degradation and load sharing using survival signature and FTA”. In: *Energies* 13.8 (Apr. 2020). Publisher: MDPI AG. ISSN: 19961073. DOI: `10.3390/en13082108`.

[114] L. Li, Z. Gao, and T. Moan. “Joint Environmental Data at Five European Offshore Sites for Design of Combined Wind and Wave Energy Devices”. In: vol. 137. June 2013. DOI: `10.1115/OMAE2013-10156`.

[115] DNV. *DNV-RP-C205: Environmental Conditions and Environmental Loads*. 2021. URL: `https://www.dnv.com/energy/standards-guidelines/dnv-rp-c205-environmental-conditions-and-environmental-loads/` (visited on 04/03/2025).

[116] I. H. Holthuijsen. *Waves in Oceanic and Coastal Waters*. Cambridge University Press, 2007.

[117] K. Johannessen, T. S. Meling, and S. Haver. “Joint Distribution for Wind and Waves in the Northern North Sea”. In: *International Journal of Offshore and Polar Engineering* (2002).

[118] Marine Regions. *Buchan Deep - Marine Gazetteer Placedetails*. 2025. URL: `https://marineregions.org/gazetteer.php?p=details&id=3340` (visited on 03/12/2025).

[119] J. Jonkman. *Definition of the Floating System for Phase IV of OC3*. National Renewable Energy Laboratory (NREL), May 1, 2010. DOI: `10.2172/979456`. URL: `http://www.osti.gov/servlets/purl/979456-qqFMGj/` (visited on 07/14/2025).

[120] S. Wang, A. R. Nejad, and T. Moan. “Dynamic Behaviour Comparison of a 10-MW Drivetrain in a Bottom-fixed Monopile and a Spar Floating Wind Turbines”. In: 2024. URL: `https://www.researchgate.net/publication/377570766_Dynamic_Behaviour_Comparison_of_a_10-MW_Drivetrain_in_a_Bottom-fixed_Monopile_and_a_Spar_Floating_Wind_Turbines` (visited on 07/14/2025).

[121] S. Margaronis. *Equinor says Scotland floating wind turbine flaw has been repaired*. 2024. URL: `https://www.ajot.com/insights/full/ai-equinor-says-scotland-floating-wind-turbine-flaw-has-been-repaired` (visited on 01/13/2025).

[122] E. Hart et al. *Main Bearing Replacement and Damage - A Field Data Study on 15 Gigawatts of Wind Energy Capacity*. National Renewable Energy Laboratory (NREL), July 1, 2023. DOI: `10.2172/1992019`. URL: `https://www.osti.gov/servlets/purl/1992019/` (visited on 07/14/2025).

[123] A. Hegazy, P. Naaijen, and J. W. Van Wingerden. *Control design for floating wind turbines*. Apr. 30, 2025. DOI: `10.5194/wes-2025-68`. URL: `https://wes.copernicus.org/preprints/wes-2025-68/` (visited on 07/14/2025).

[124] W. Yu et al. “Evaluation of control methods for floating offshore wind turbines”. In: *Journal of Physics: Conference Series* 1104 (2018). Publisher: IOP Publishing, p. 012033. ISSN: 1742-6588, 1742-6596. DOI: `10.1088/1742-6596/1104/1/012033`. URL: `https://iopscience.iop.org/article/10.1088/1742-6596/1104/1/012033` (visited on 07/14/2025).

[125] D. Stockhouse et al. “Sink or Swim: A Tutorial on the Control of Floating Wind Turbines”. In: *2023 American Control Conference (ACC)*. 2023 American Control Conference (ACC). San Diego, CA, USA: IEEE, 2023, pp. 2512–2529. DOI: `10.23919/acc55779.2023.10155920`. URL: `https://ieeexplore.ieee.org/document/10155920/` (visited on 07/14/2025).

A

Case Study parameters

A.1. Tower properties

In Figure A.1, the Fore-Aft (FA), Side-to-Side (SS), axial and torsional stiffness with respect to the height fraction of the tower are illustrated for the BOWT and FOWT models. The tower of the FOWT is designed stiffer than in the BOWT, to mitigate the amplified motions transmitted from the semi-submersible platform to the rotor-nacelle assembly and ensure proper rotor operation.

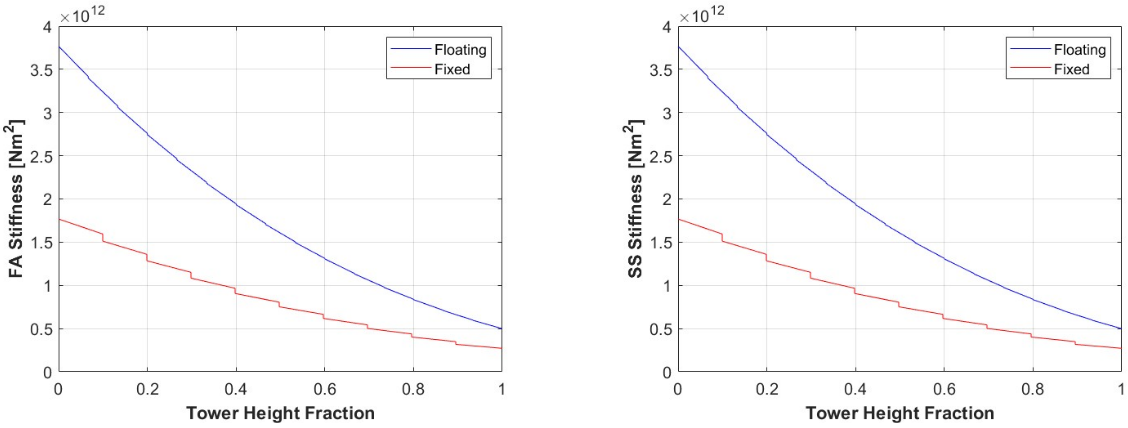

(a) Tower Fore-Aft Stiffness

(b) Tower Side-Side Stiffness

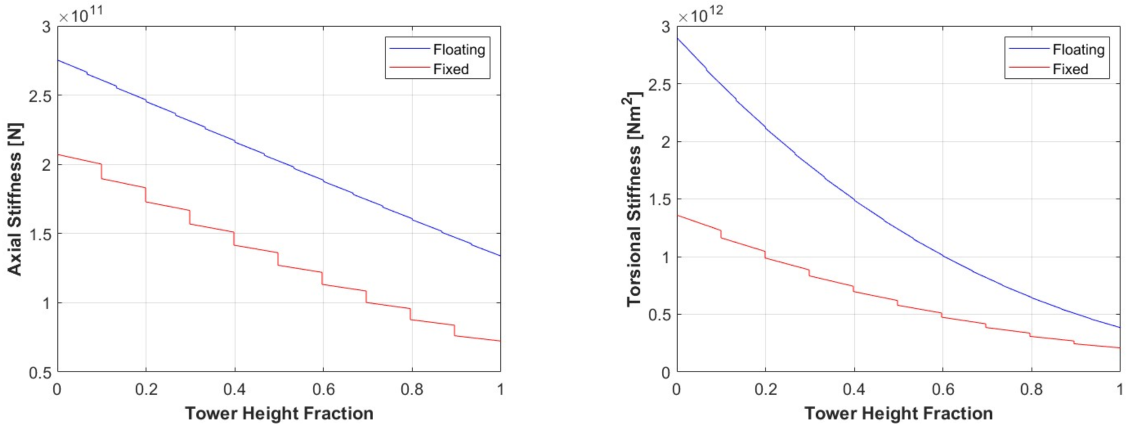

(c) Tower Axial Stiffness

(d) Tower Torsional Stiffness

Figure A.1: Stiffness properties of the towers of BOWT and FOWT with respect to the height fraction

A.2. Floating platform and fairlead tensions

The Nautilus DTU 10-MW FOWT, is equipped with a Station Keeping System (SKS) to maintain platform stability and positional balance. The system consists of four symmetrically arranged catenary mooring lines anchored to the seabed. The SKS layout of the original 130 water depth model is shown in Figure A.2, while in Table A.1, the main parameters of SKS are included.

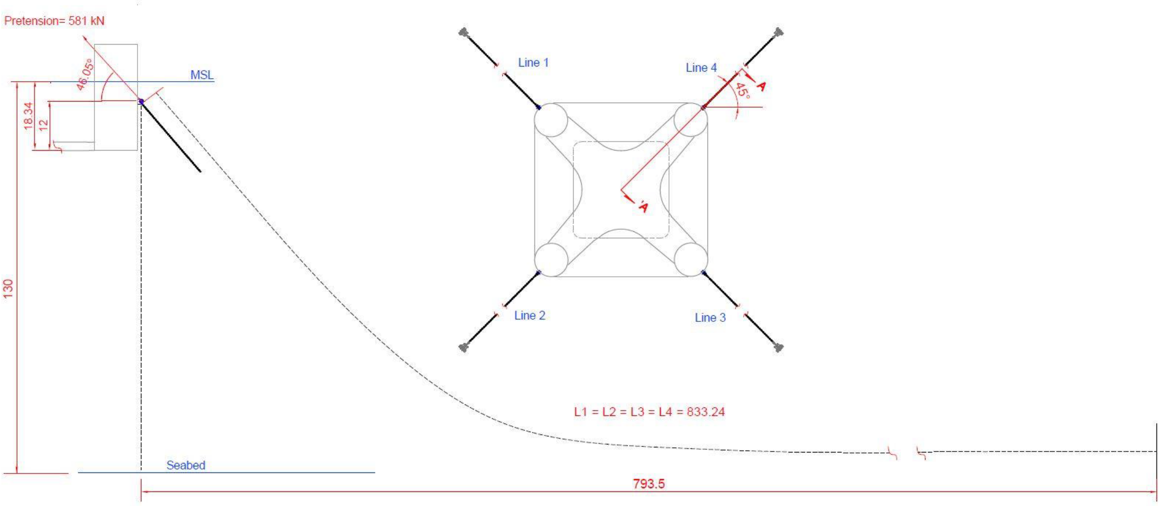

Figure A.2: Nautilus DTU-10 MW semisubmersible platform mooring system layout [102]

Table A.1: NAUTILUS-10 SKS Mooring System Properties

NAUTILUS-10 SKS Property	Value	Units
Total fairlead number	4	[-]
Total mooring lines number	4	[-]
Fairlead radius from floating platform centre	43.96	[m]
Fairlead position above keel	12.00	[m]
Anchor radius from floating platform centre	837.46	[m]
Mooring line type	Studless chain	[-]
Mooring line unstretched length	833.24	[m]
SKS lines pretension	406,300	[N]
Anchoring system type	Drag anchor	[-]

Figure A.3 compares the fairlead tensions of the four mooring lines for the original Nautilus DTU 10-MW FOWT model at 130 m water depth and the adjusted model at 60 m. The fairlead tension magnitudes are generally close between the two configurations, and their periodic responses show similar periods and frequencies for all lines. The stiffness of the mooring system directly affects the platform's natural frequencies, thus, the next section presents the free decay tests used to determine the natural frequencies of both the original and adjusted models of the FOWT and BOWT.

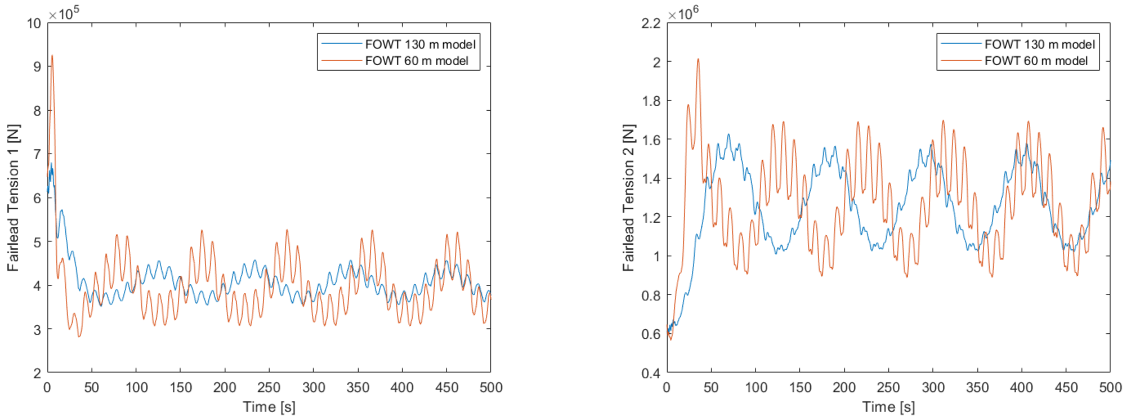

(a) Fairlead tension 1 **(b)** Fairlead tension 2

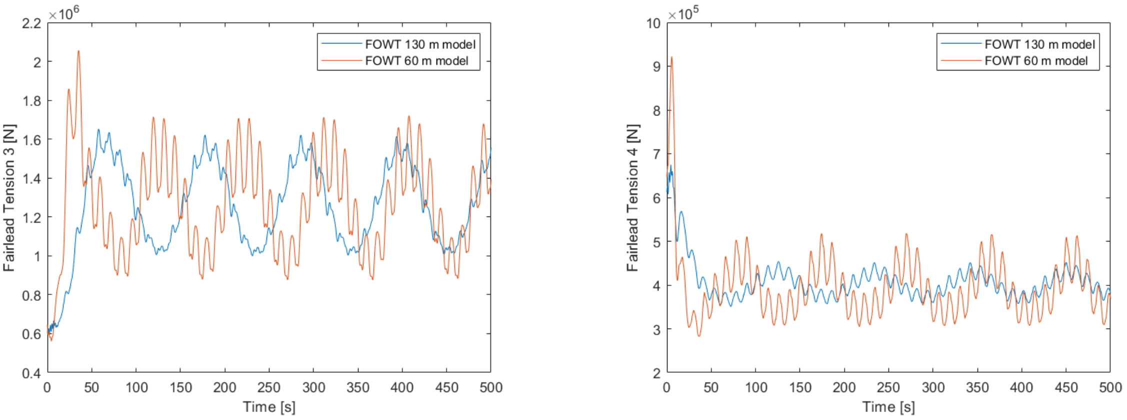

(c) Fairlead tension 3 **(d)** Fairlead tension 4

Figure A.3: Fairlead tensions of the four mooring lines of the FOWT for the original water depth of 130 m and the one of 60 m

A.3. Free Decay tests

Free-decay tests are performed to identify the natural frequencies of the tower motions and the platform six-DOF motions in the FOWT. In the free-decay tests conducted in this thesis, according to the widely applied method [85, 88], it is considered that there is no wind and still water (no waves), while an initial displacement is imposed in the DOF of interest and the motion is recorded. Moreover, only the examined DOF is enabled in the ElastoDyn, while the remaining DOFs remain disabled to isolate the desired motion without any external perturbations. That also means that there is no control applied on the WT. The free-decay tests were performed with a timestep of 0.005 s for both BOWT and FOWT and for a time period of 600 s. The initial displacements for every DOF are shown in Table A.2. Also, for the fore-aft and side-to-side free-decay test of the FOWT and BOWT the same initial displacements are considered.

DOF of Interest	Initial DOF Displacement
Tower Fore-Aft (m)	1
Tower Side-Side (m)	1
Platform Surge (m)	5
Platform Sway (m)	5
Platform Heave (m)	2
Platform Roll (deg)	2
Platform Pitch (deg)	5
Platform Yaw (deg)	5

Table A.2: Initial displacements used for DOFs free decay tests

The natural frequencies are usually obtained after converting the time-domain signals (retrieved from OpenFAST) into frequency-domain plots using a Fast Fourier Transform (FFT). The timeseries of the performed free-decay tests are shown below, as well as their corresponding frequency domain response, which is used to extract the natural frequencies.

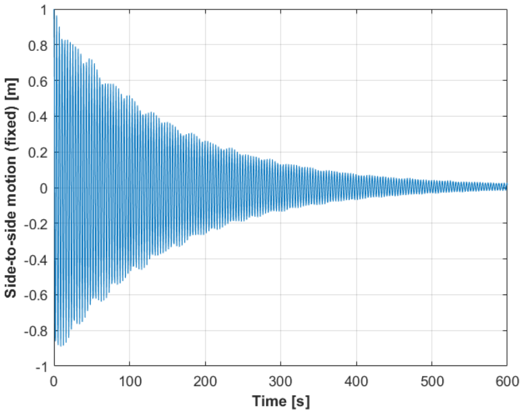

Figure A.4: Free-decay test - BOWT side-to-side tower motion

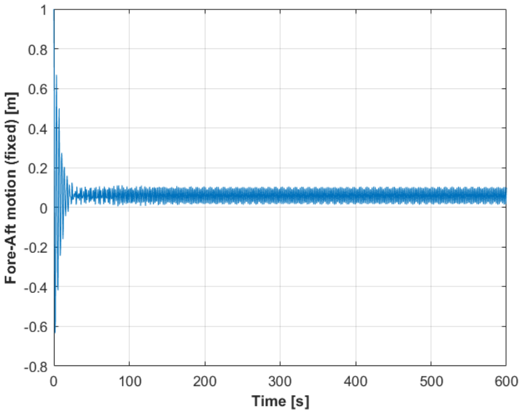

Figure A.5: Free-decay test - BOWT fore-aft tower motion

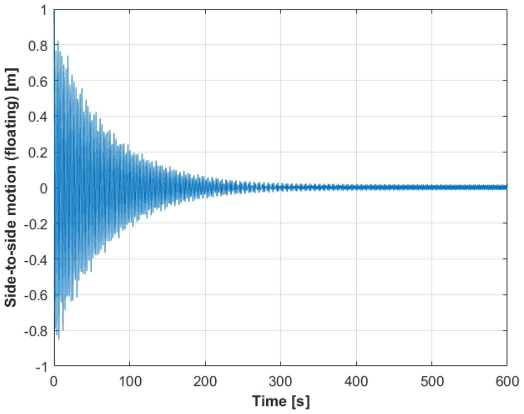

Figure A.6: Free-decay test - FOWT side-to-side tower motion

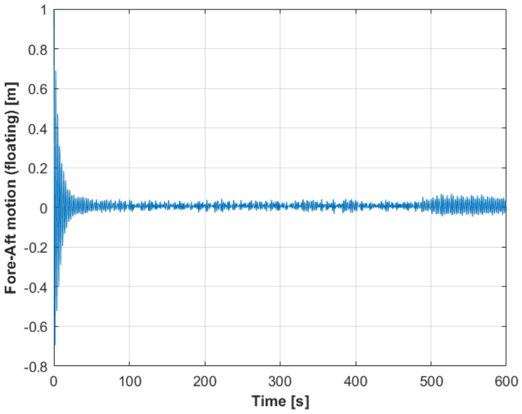

Figure A.7: Free-decay test - FOWT fore-aft tower motion

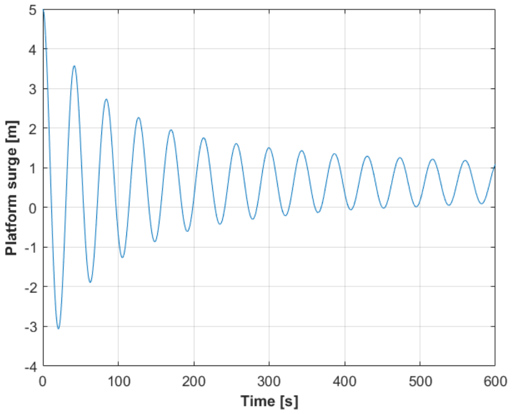

Figure A.8: Free-decay test - FOWT platform surge motion

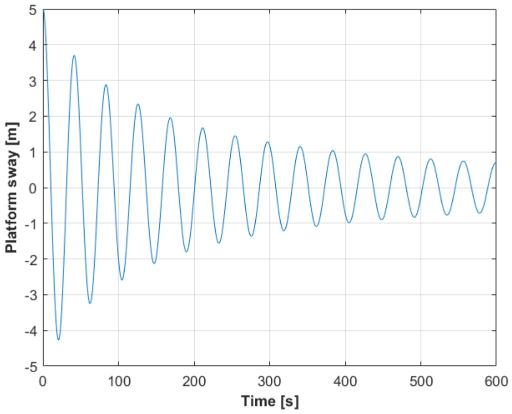

Figure A.9: Free-decay test - FOWT platform sway motion

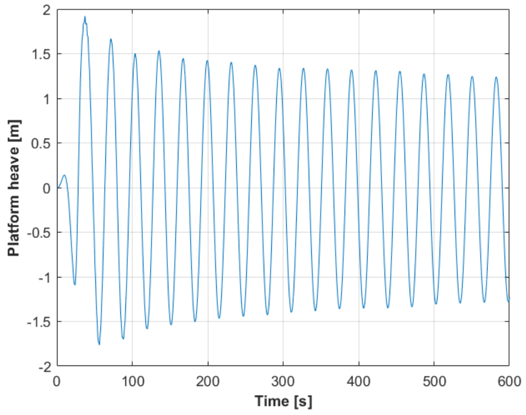

Figure A.10: Free-decay test - FOWT platform heave motion

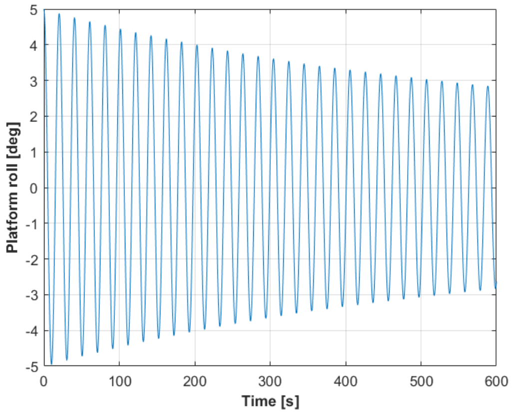

Figure A.11: Free-decay test - FOWT platform roll motion

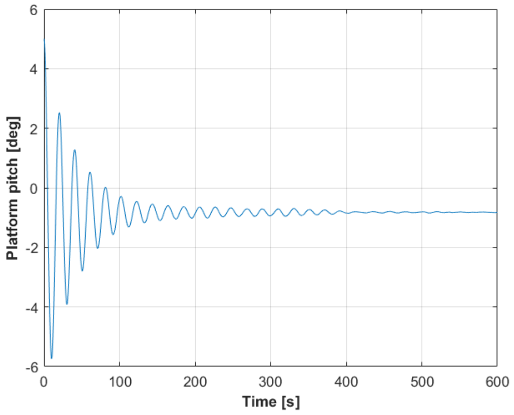

Figure A.12: Free-decay test - FOWT platform pitch motion

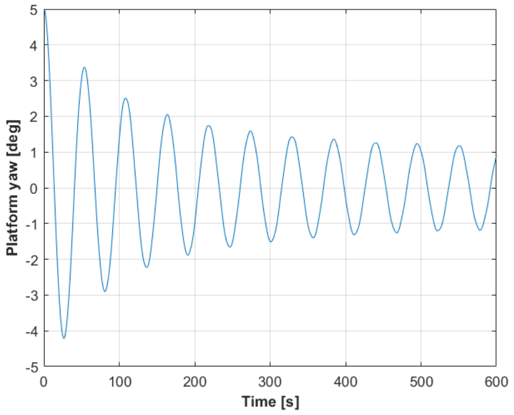

Figure A.13: Free-decay test - FOWT platform yaw motion

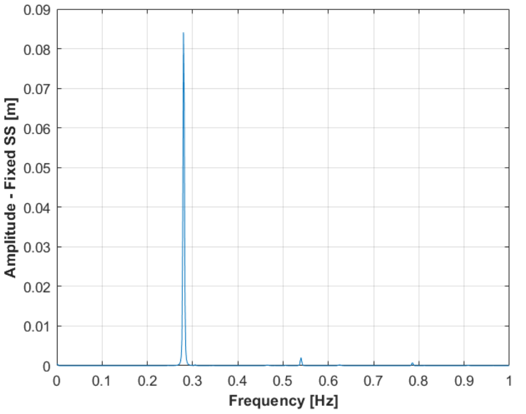

Figure A.14: Free-decay test - BOWT side-to-side tower motion FFT

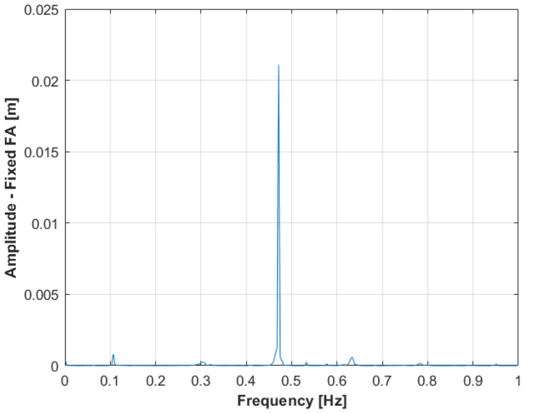

Figure A.15: Free-decay test - BOWT fore-aft tower motion FFT

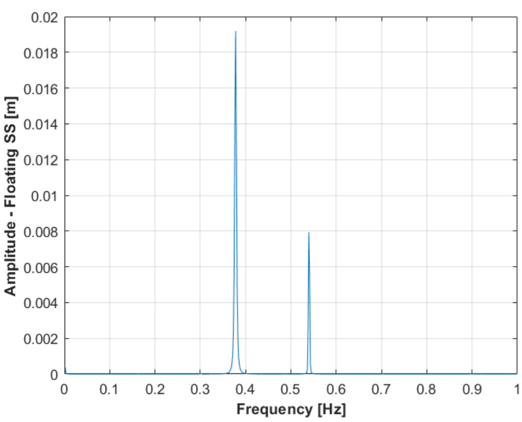

Figure A.16: Free-decay test - FOWT side-to-side tower motion FFT

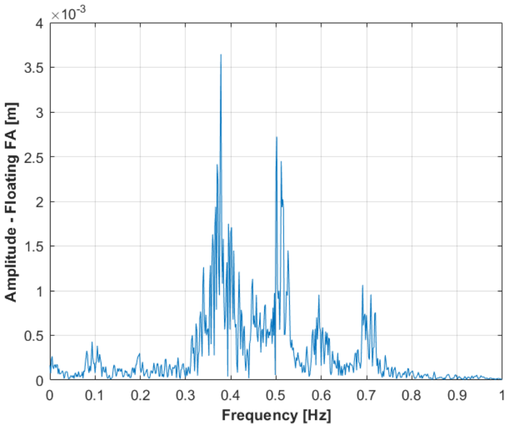

Figure A.17: Free-decay test - FOWT fore-aft tower motion FFT

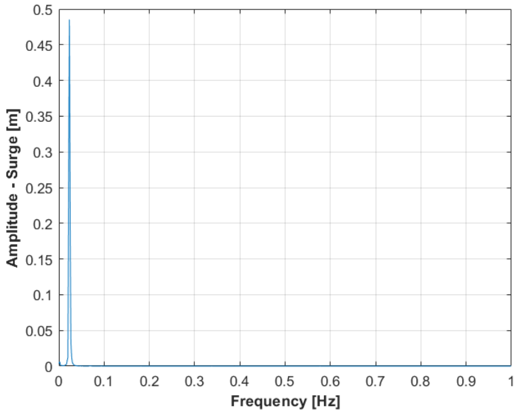

Figure A.18: Free-decay test - FOWT platform surge motion FFT

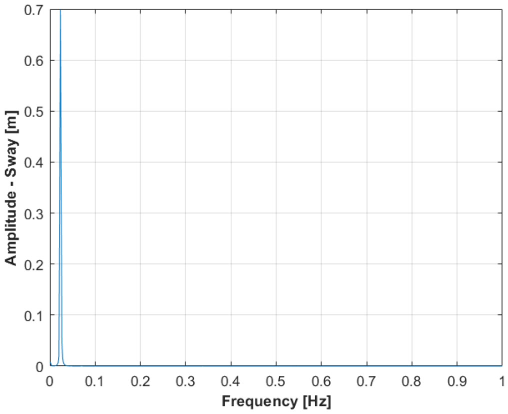

Figure A.19: Free-decay test - FOWT platform sway motion FFT

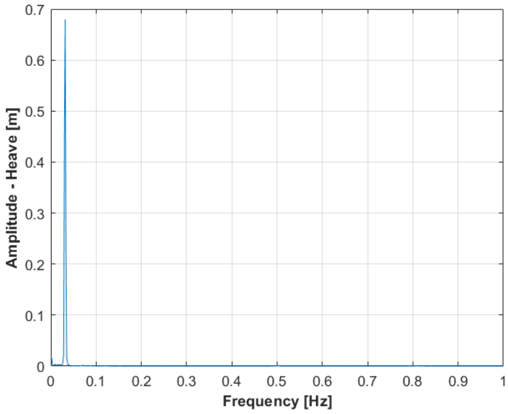

Figure A.20: Free-decay test - FOWT platform heave motion FFT

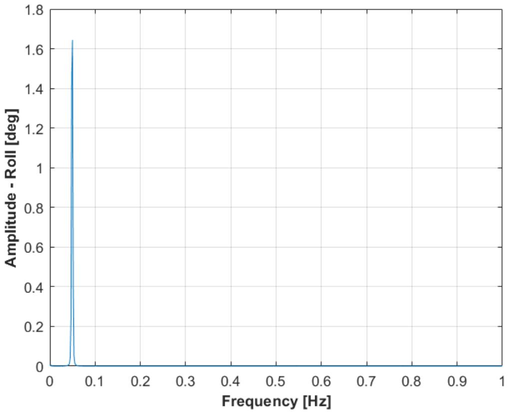

Figure A.21: Free-decay test - FOWT platform roll motion FFT

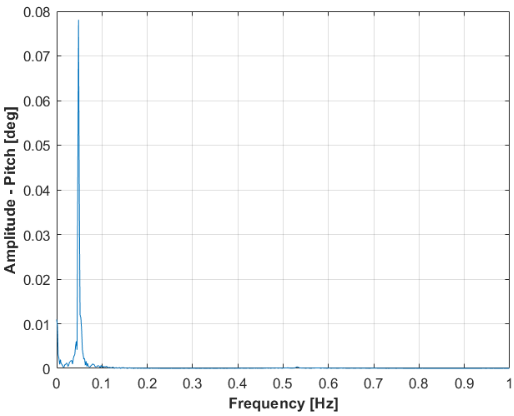

Figure A.22: Free-decay test - FOWT platform pitch motion FFT

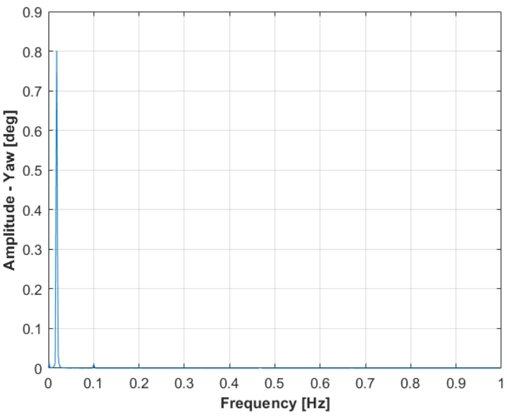

Figure A.23: Free-decay test - FOWT platform yaw motion FFT

According to the information that can be extracted from the tests, the dominant peak frequencies correspond to the natural frequencies of each DOF for the adjusted FOWT and BOWT models. The natural frequencies of the different DOFs can be summarized in Table A.3 for both the adjusted and original BOWT and FOWT models. The plots of the free-decay tests of the original models are omitted for brevity.

Table A.3: Comparison of natural frequencies [Hz] for FOWT and BOWT (adjusted model vs. original model).

Degree of Freedom	FOWT (adjusted)	FOWT (original)	BOWT (adjusted)	BOWT (original)
Tower FA	0.378	0.3833	0.4713	0.4717
Tower SS	0.378	0.3817	0.2798	0.2800
Surge	0.0233	0.0233	–	–
Sway	0.0233	0.0233	–	–
Heave	0.0317	0.0317	–	–
Roll	0.0500	0.0500	–	–
Pitch	0.0483	0.0483	–	–
Yaw	0.0183	0.0183	–	–

Table A.3 shows that the natural frequencies of the various DOFs remain almost constant between the adjusted and original FOWT and BOWT models. It is also clear that the natural frequencies of the platform are very low, below 0.1 Hz. Moreover, the tower SS natural frequency in the FOWT is higher than that in the BOWT, while the tower FA natural frequency is higher for the BOWT. This may be explained by the fact that although the tower of the FOWT is stiffer per height fraction than that of the BOWT, it also has higher mass per unit length. These two parameters affect the natural frequencies in opposite directions, higher stiffness tends to increase them, whereas higher mass tends to reduce them.

A.4. Input conditions

Table A.4 and Table A.5 complement the wind and wave rose of Buchan Deep [105], shown in Figure 4.9a and Figure 4.9b, respectively. Specifically, the tables list the directional probability for each wind speed cluster (of 2 m/s) and significant wave height cluster (of 1 m), respectively.

Table A.4: Directional distribution of wind speed, at 10 m above sea level, at Buchan Deep [105]

Wind (m/s)	0°	30°	60°	90°	120°	150°	180°	210°	240°	270°	300°	330°	Omni
<2	0.31	0.32	0.30	0.35	0.35	0.37	0.40	0.36	0.35	0.31	0.31	0.34	4.08
<4	1.24	1.09	1.01	1.20	1.31	1.45	1.61	1.33	1.24	1.05	1.10	1.40	14.74
<6	4.12	2.88	2.41	2.67	3.45	5.42	6.49	5.57	4.00	3.48	3.53	4.34	48.44
<8	6.55	3.82	3.07	3.25	4.54	7.15	8.56	7.43	5.30	4.35	4.35	5.66	80.95
<10	7.14	4.03	3.26	3.46	5.66	9.90	11.38	9.75	6.32	5.12	5.11	6.27	89.51
<12	7.55	4.12	3.34	3.56	6.96	11.53	13.25	11.18	6.84	5.67	5.65	6.83	93.91
<14	7.65	4.12	3.34	3.66	7.00	12.63	14.58	12.57	6.87	6.95	7.01	6.99	97.27
<16	7.65	4.12	3.34	4.26	9.13	13.93	15.99	13.95	7.15	7.71	7.90	7.17	98.99
<18	7.77	4.14	3.37	4.29	10.64	15.04	16.94	14.99	7.26	7.88	8.05	7.29	99.97
<20	7.77	4.14	3.37	4.29	10.64	15.04	16.94	14.99	7.26	7.88	8.05	7.29	99.97
<22	7.77	4.14	3.37	4.29	10.64	15.04	16.94	14.99	7.26	7.88	8.05	7.29	100.00
<24	7.77	4.14	3.37	4.29	10.64	15.04	16.94	14.99	7.26	7.88	8.05	7.29	100.00
<26	7.77	4.14	3.37	4.29	10.64	15.04	16.94	14.99	7.26	7.88	8.05	7.29	100.00
<28	7.78					10.05	14.01	15.64	8.75	7.29	7.92		
<30	7.78												
<32	7.78												
Total	7.78	4.14	3.37	4.29	6.24	10.05	14.01	15.64	8.75	7.29	7.92	10.62	100.00
Mean	8.1	6.6	6.2	7.2	8.0	8.1	8.8	9.7	8.5	8.9	9.3	8.5	8.5
Maximum	28.2	23.3	22.4	22.8	23.6	25.6	26.9	30.6	25.3	27.7	31.4	28.4	31.4

Table A.5: Directional distribution of significant wave height H_s at Buchan Deep [105]

H_s **(m)**	0°	30°	60°	90°	120°	150°	180°	210°	240°	270°	300°	330°	Omni
<1	4.40	4.73	1.78	2.07	2.07	3.15	3.00	2.86	0.88	0.55	0.73	1.76	27.98
<2	11.62	9.70	3.44	5.05	4.74	7.07	7.97	8.97	2.29	1.43	1.96	4.65	68.88
<3	15.31	10.98	3.66	5.22	6.56	8.81	10.56	12.24	2.88	1.55	2.21	5.88	86.00
<4	16.91	11.32	3.72	6.85	6.91	10.66	12.63	13.03	2.88	1.86	2.34	5.88	90.51
<5	17.66	11.40	3.99	7.71	7.70	10.70	12.65	13.04	3.02	1.97	2.88	7.34	98.51
<6	18.11	11.43	4.00	7.93	7.94	10.95	12.65	13.04	3.02	1.97	2.88	7.34	99.36
<7	18.14	11.43	4.00	7.95	7.94	11.00	12.65	13.04	3.02	1.97	2.88	7.34	99.97
<8	18.14	11.43	4.00	7.95	7.94	11.00	12.65	13.04	3.02	1.97	2.88	7.34	99.97
<9	18.14	11.43	4.00	7.95	7.94	11.00	12.65	13.04	3.02	1.97	2.88	7.34	100.00
<10	18.20	11.43	7.60	7.42		12.26	13.76						
<11	18.20												
Total	18.20	11.43	4.00	7.60	7.42	10.13	12.26	13.76	3.02	1.97	2.88	7.34	100.00
Mean	2.0	1.4	1.3	1.8	1.9	1.7	1.9	1.8	1.6	1.7	1.9	1.8	1.8
Maximum	10.2	8.1	6.7	8.6	8.4	7.7	8.4	8.9	6.3	6.2	6.6	8.4	10.2

B

LDD Results

This appendix section presents LDD results for four more wind speeds, for realistic and aligned wind-wave case, respectively. These plots verify that at below-rated wind speeds, the MB1 of the BOWT experiences more load cycles. However, above the rated wind speed, the MB1 of the FOWT shows more cycles at higher load values.

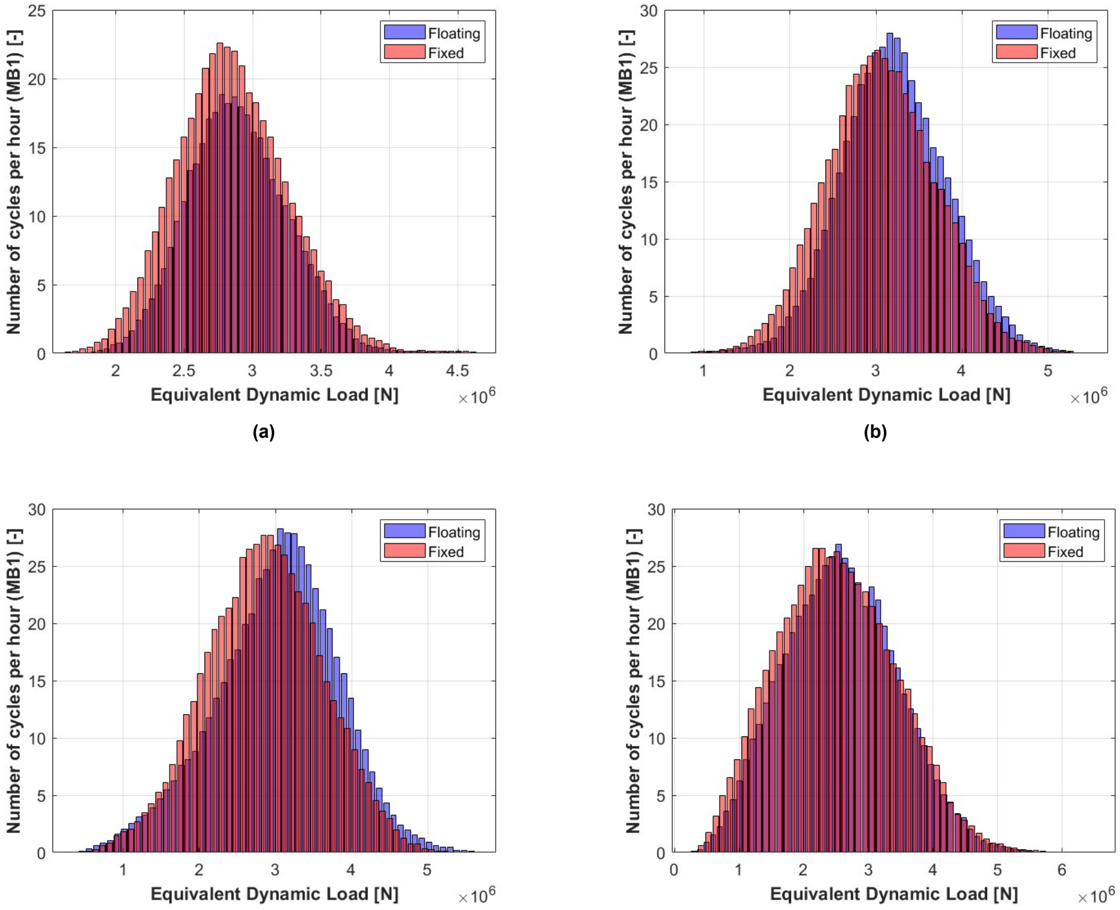

(a)

(b)

(c)

(d)

Figure B.1: Realistic case: LDD histograms for FOWT and BOWT for four different wind speeds: (a) 5.5 m/s, (b) 10.5 m/s, (c) 13.5 m/s and (d) 19.5 m/s.

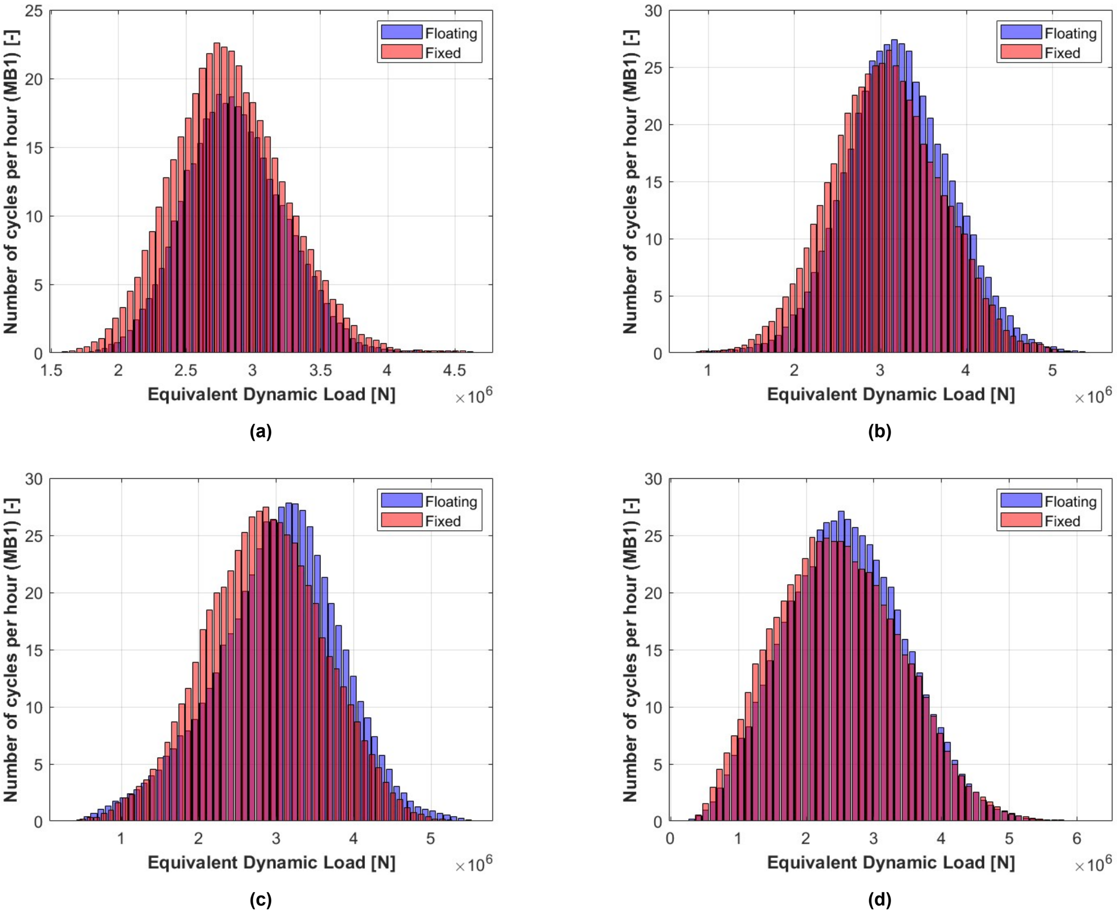

(a)

(b)

(c)

(d)

Figure B.2: Aligned wind-wave case: LDD histograms for FOWT and BOWT for four different wind speeds: (a) 5.5 m/s, (b) 10.5 m/s, (c) 13.5 m/s and (d) 19.5 m/s.

C

Aligned wind-wave case Results

This appendix includes results of the aligned wind-wave case that are omitted from the main body since they are similar to the results of the realistic case. They are presented in the order that they are shown at the main body in Chapter 5.

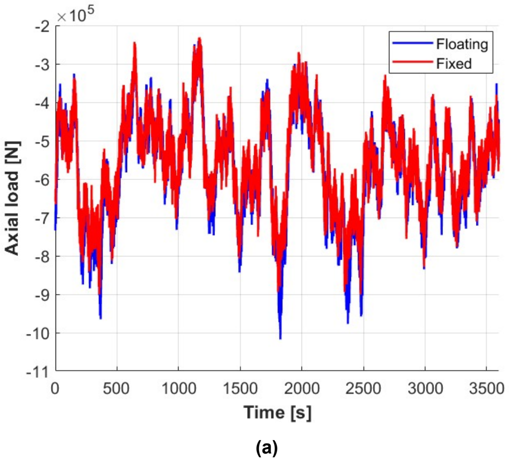

Figure C.1: Aligned wind-wave case: Time series of MB1 axial load $F_{\alpha,1}$ at (a) 8.5 and (b) 13.5 m/s

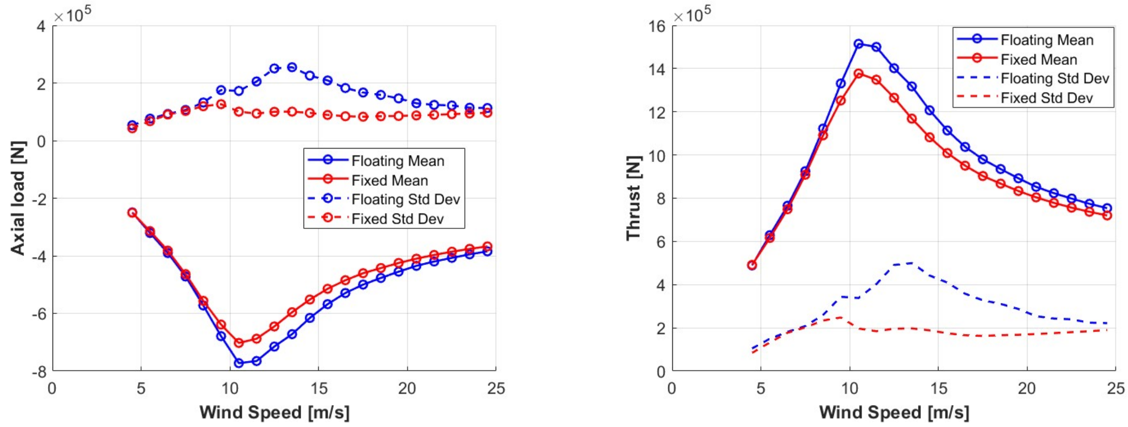

(a) MB1 axial load, $F_{\alpha,1}$, mean and standard deviation **(b)** Thrust force, T, mean and standard deviation

Figure C.2: Aligned wind-wave case: (a) MB1 Axial load, $F_{\alpha,1}$, and (b) thrust force, T, mean and standard deviation as a function of wind speed

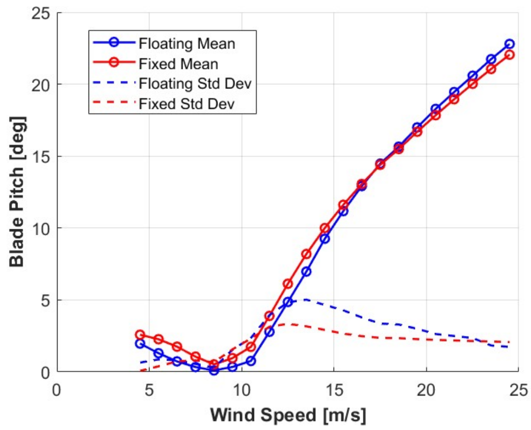

Figure C.3: Aligned wind-wave case: Blade pitch angle, mean and standard deviation as a function of wind speed

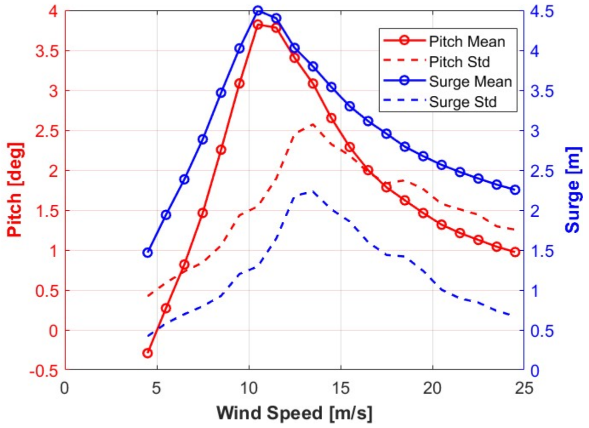

Figure C.4: Aligned wind-wave case: Platform pitch and surge motion, mean and standard deviation as a function of wind speed

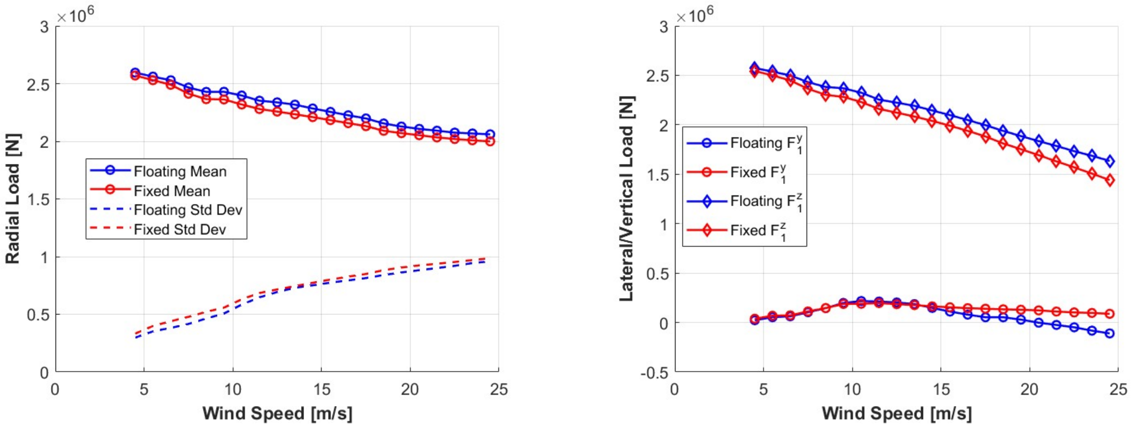

(a) Radial load, $F_{r,1}$, mean and standard deviation

(b) Lateral, F_1^y, and vertical load, F_1^z, means

Figure C.5: Aligned wind-wave case: MB1 Radial load, $F_{r,1}$, and its components, F_1^y and F_1^z, as a function of wind speed

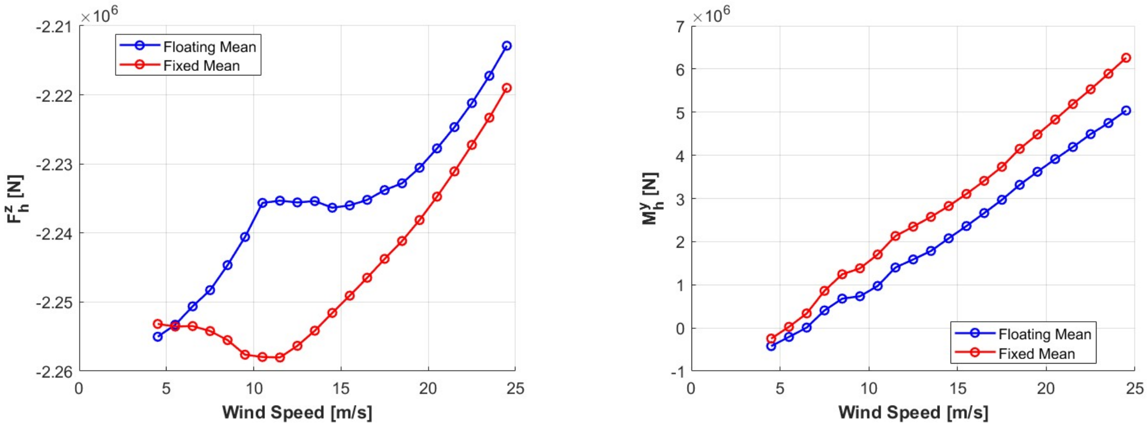

(a) Hub force F_h^z means

(b) Hub moment M_h^y means

Figure C.6: Aligned wind-wave case: Hub force, F_h^z, and moment, M_h^y, related to MB1 vertical load, F_1^z as a function of wind speed

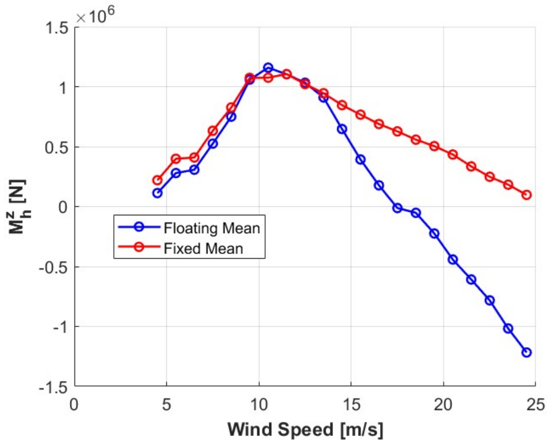

Figure C.7: Aligned wind-wave case: Hub moment M_h^z mean as a function of wind speed

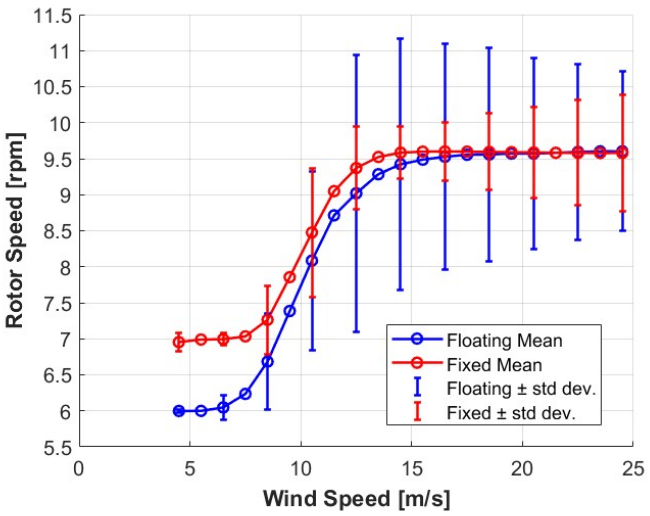

Figure C.8: Aligned wind-wave case: Rotor speed for FOWT and BOWT as a function of wind speed

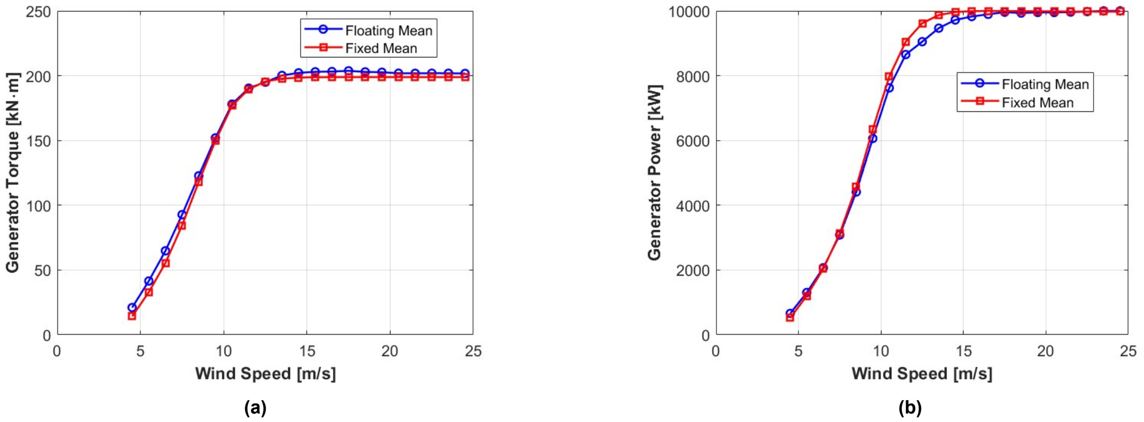

Figure C.9: Aligned wind-wave case: Mean (a) Generator Torque and (b) Power as a function of wind speed

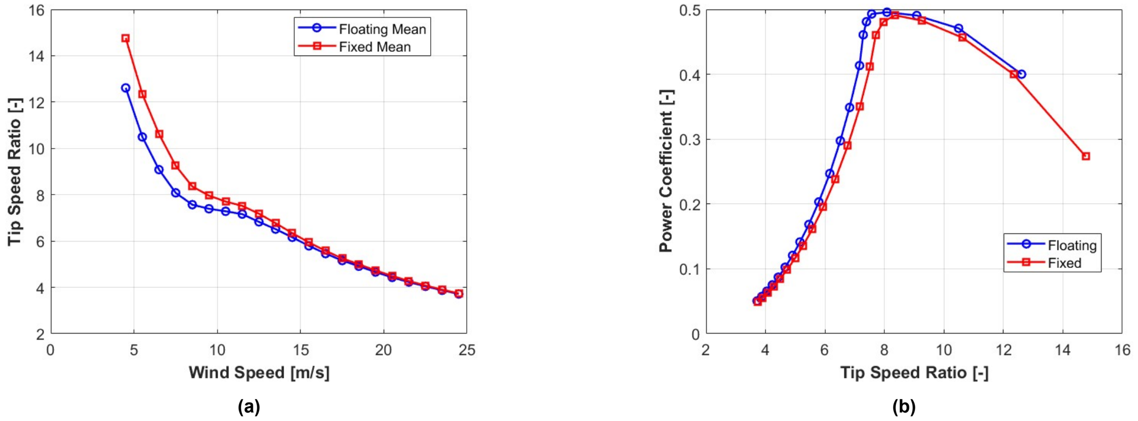

Figure C.10: Aligned wind-wave case: Mean (a) Tip speed ratio and (b) power coefficient as a function of wind speed

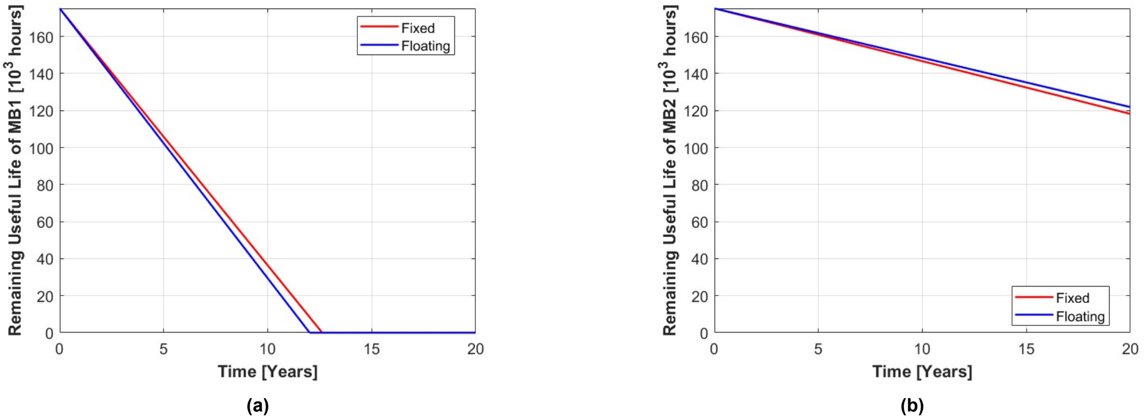

Figure C.11: Aligned wind-wave case: Remaining Useful Life degradation of (a) MB1 and (b) MB2 over time

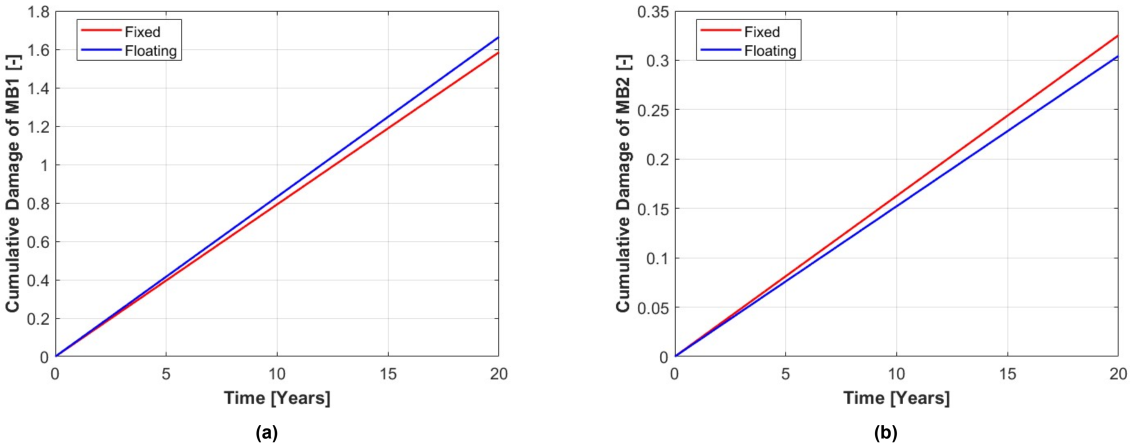

Figure C.12: Aligned wind-wave case: Cumulative damage of (a) MB1 and (b) MB2 over time

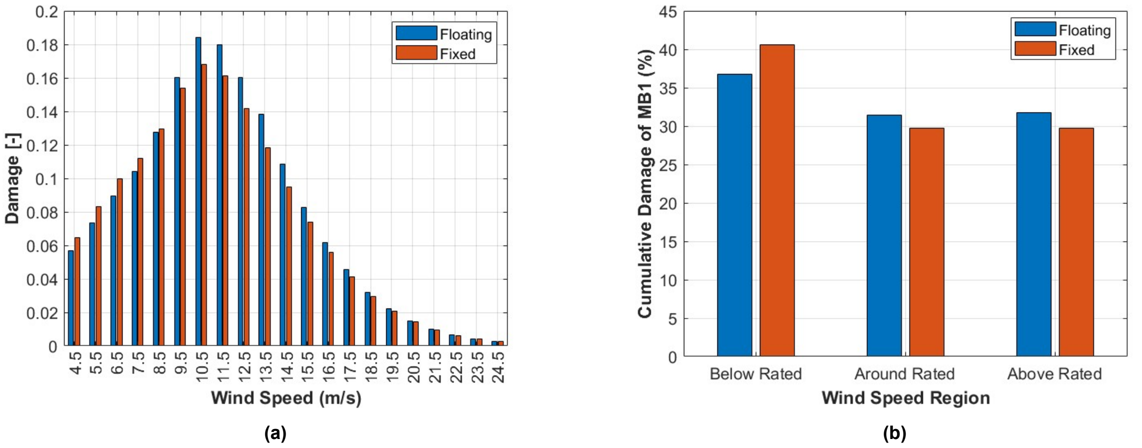

Figure C.13: Aligned wind-wave case: MB1 20-year (a) cumulative damage per wind speed and (b) normalized cumulative damage per operating region

D

Platform motion Results

This appendix presents complementary statistics for the FOWT platform over the operating wind speeds: minimum and maximum values, mean, standard deviation, and range (max - min) of platform motions. These detailed statistics supplement the main body analysis, which focuses on mean motion characteristics. The max/min values capture peak responses during load fluctuations under the simulated turbulent conditions. Thus, they show much higher variation than the mean or standard deviation.

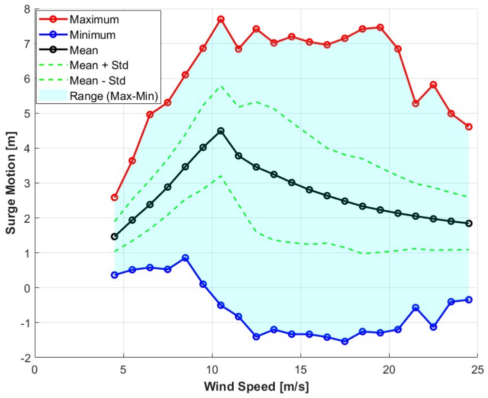

Figure D.1: Realistic case: Platform surge motion statistics

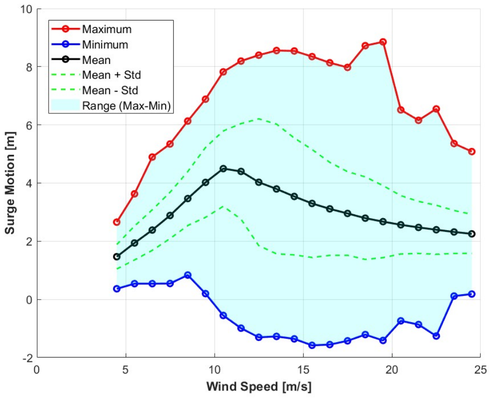

Figure D.2: Aligned wind-wave case: Platform surge motion statistics

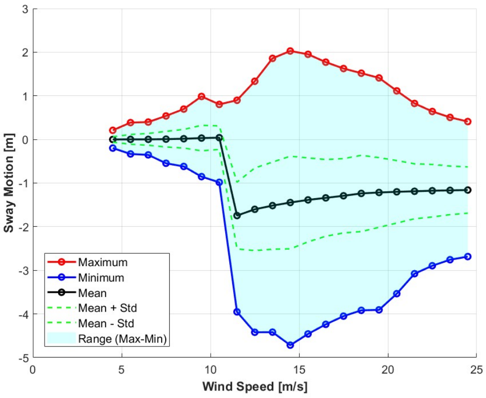

Figure D.3: Realistic case: Platform sway motion statistics

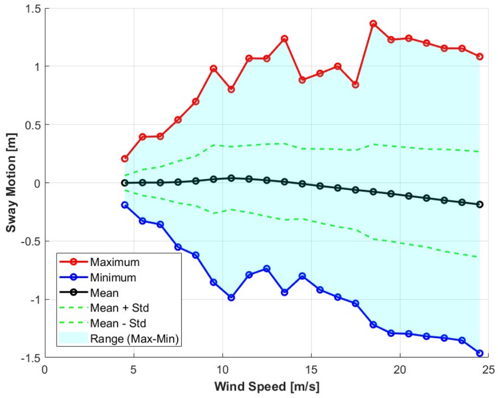

Figure D.4: Aligned wind-wave case: Platform sway motion statistics

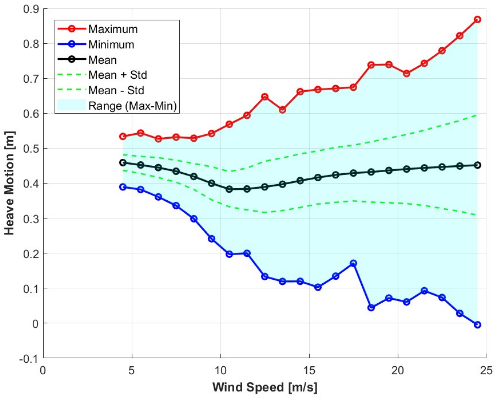

Figure D.5: Realistic case: Platform heave motion statistics

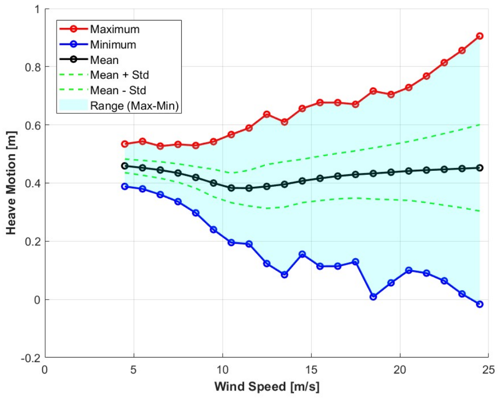

Figure D.6: Aligned wind-wave case: Platform heave motion statistics

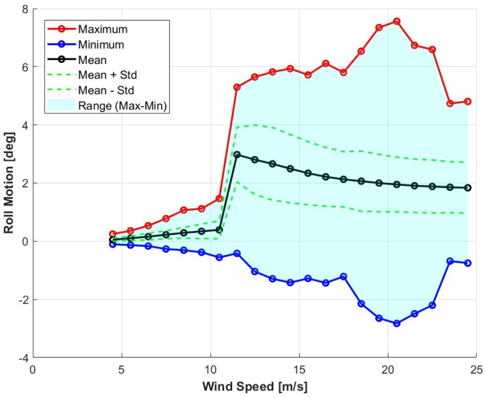

Figure D.7: Realistic case: Platform roll motion statistics

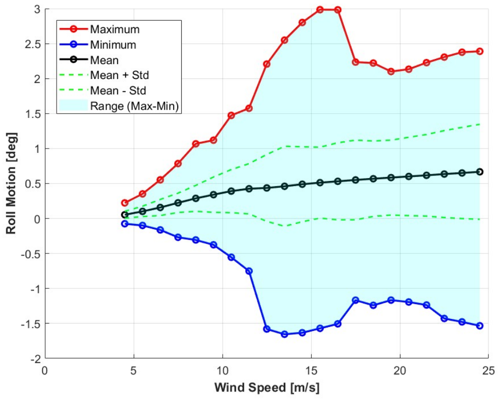

Figure D.8: Aligned wind-wave case: Platform roll motion statistics

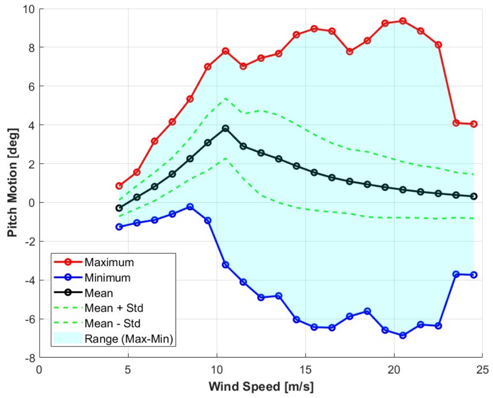

Figure D.9: Realistic case: Platform pitch motion statistics

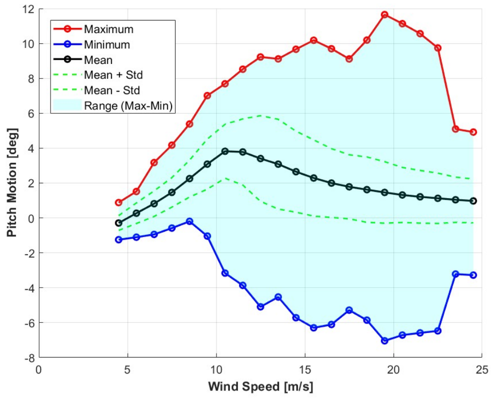

Figure D.10: Aligned wind-wave case: Platform pitch motion statistics

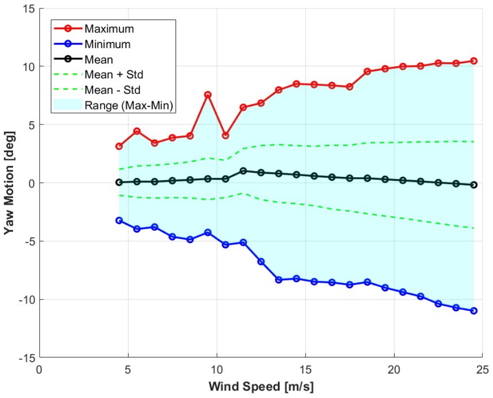

Figure D.11: Realistic case: Platform yaw motion statistics

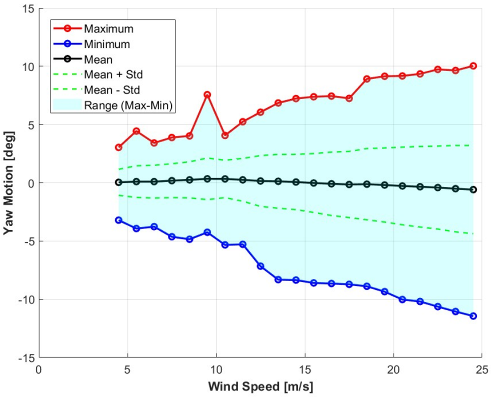

Figure D.12: Aligned wind-wave case: Platform yaw motion statistics